Title

Fluidically Driven Systems for Tangible and Interactive Media

Permalink

https://escholarship.org/uc/item/5t04793g

Author

Jadhav, Saurabh Subhash

Publication Date

2021

Peer reviewed|Thesis/dissertation

UNIVERSITY OF CALIFORNIA SAN DIEGO

Fluidically Driven Systems for Tangible and Interactive Media

A dissertation submitted in partial satisfaction of the
requirements for the degree
Doctor of Philosophy

in

Engineering Sciences (Mechanical Engineering)

by

Saurabh Jadhav

Committee in charge:

Professor Michael T. Tolley, Chair
Professor Nicholas Gravish
Professor Darren Lipomi
Professor Tania Morimoto
Professor Jurgen Schulze

2021

The dissertation of Saurabh Jadhav is approved, and it is acceptable in quality and form for publication on microfilm and electronically

University of California San Diego

2021

DEDICATION

In loving memory of my grandma,

Sushma Anant Hatkar

TABLE OF CONTENTS

LIST OF FIGURES

LIST OF TABLES

ACKNOWLEDGEMENTS

This dissertation would not be possible without the great deal of support and encouragement that I received.

I would like to begin by thanking my advisor, Dr. Michael T. Tolley, for his guidance, patience, support, and mentorship. Thank you for being a constant source of encouragement since the beginning of my graduate school. Thank you for continuously nurturing any ideas that I had, right from the beginning when I proposed the "soft haptic glove" as a class project, and steering me in the right direction whenever I needed it. Dr. Michael Tolley's door was always open whenever I needed any advice or ran into trouble. Thank you for the countless edits and feedback on the manuscripts that help me learn a great deal. I truly learned the techniques of scientific writing and effectively presenting my research from you. Thank you for giving me this fantastic opportunity.

Thank you to the members of my committee. Special gratitude to Dr. Jurgen Schulze. Thank you for your constant support, encouragement, and mentorship. Thank you for encouraging my ideas and motivating me to pursue my passion for VR. Your insights and expertise into 3D-user interfaces guided my graduate research. I was delighted to be part of your group during the early years when commercial VR was picking up, and would always cherish those discussions in the meetings right from the coolest new hardware in the market to any new game that was published that week. Thank you for accepting me as your student, although I was from outside the CSE department. To Dr. Nick Gravish, Thank you for all your mentorship and invaluable insights that guided my research projects. Thank you for your invaluable lessons on modeling granular media to the design of experiments that answer the research questions. The discussions we had during our topic subgroup meetings were always very insightful. To Dr. Tania Morimoto, Thank you for always being available whenever I needed any advice or feedback. I had a fantastic time TAing your class on Haptic Interfaces, and it was great fun to participate and help in building this new course at UCSD. Thank you for sharing your enthusiasm and insight on haptic interfaces. Also, thank you for all your advice and mentoring outside the class. To Dr. Darren Lipomi, Thank you for your invaluable lessons on topics ranging from professional development to be a successful graduate student. I always found your talks through IDEA center and your podcasts on YouTube to be very insightful.

A Ph.D. tends to be a very solitary endeavor. This is not being the case for me at all, Thanks to the members and alumni from the Bioinspired Robotics and Design Lab, many of whom I've known since the beginning of my grad school. Thank you for your help and encouragement along the way. Dylan, I consider it a great honor to being able to contribute to some of your fun projects right from the 3D-printed quadruped to the new electronics-free version. Thank you for all the stimulating, late-night discussions we had and every meal we shared. You were the first person from the lab that I had collaborated with before I ventured into soft robotics. Ben, thank you for all the encouragement and for teaching me to have a positive approach to everything. I am glad that we were able to be housemates during the course of our Ph.D.s. Michael, thanks for the constant encouragement and being supportive whenever I needed it. Thanks for all the help before my defense and for my dissertation. Cheers to all the meals we shared over the past year. Jess, thank you for the collaborations and for sharing your expertise on ocean exploration and biology. Will, thanks for being an ally and keeping me awake during all our late night/ early morning sessions in the lab. Caleb, thanks for all your help and insights as a senior Ph.D. student in the lab. Paul, thanks for all your advice and insights with soft robot prototyping whenever I got stuck, and thanks for your help as a TA in the Soft Robotics class. Adriane, thank you for all the late-night/ early morning discussions about the projects which were always intellectually stimulating. Emily, thanks for all the help and feedback on writing and always being willing to help. Iman, thank you for sharing your insights and expertise on electronics, circuit modeling, and controls. Jiayao cheers to all the meals we shared over the past year and thanks for being a co-TA for the MAE 150 class. Ramzi, thanks for all your help with my research and insights into tech transfer. Shivam, thank you for all the insightful discussions over all the meals we shared, and thank you for being there whenever I needed. Thank you to all the BRDL alumni including Jamie, Tom, Francis, Dan, Charlie, and Bocheng. None of this would have worked out as well without all of your help and support.

I would like to thank my parents and grandparents for their constant support (both financial and emotional) and believing in me. To all my friends from undergrad for encouraging and supporting me, especially Akash, Chaitanya, Kunal, Mihir, Swapnil, Giridhar, Anish, Suraj, and Ashwin. Lastly, I would like to thank all my undergraduate and high school professors and tutors for making me capable to pursue this endeavor. If you are reading this and I haven't named you, thank you for your patience and support. If we have met, I have learnt something from you.

The following acknowledgements are to satisfy the requirements of the University of California San Diego.

Chapter 2, in full, is a reprint of the material as it appears in Soft Robotics, 2021. Jadhav, Saurabh; Ramzi Majit, Mohamad Abdul; Shih, Benjamin; Schulze, Jurgen P.; Tolley, Michael T., Soft Robotics 2021. The dissertation author was the primary investigator and author of this paper.

Chapter 3, or portion thereof, is being prepared for publication of the material. Jadhav, Saurabh; Glick, Paul; Ishida, Michael; Zhang, Ziyang; Chan, Christian; Adibnazari, Iman; Schulze, Jurgen P.; Tolley, Michael T. The dissertation author was the primary investigator and author of this paper.

Chapter 4, or portion thereof, is being prepared for publication of the material. Jadhav, Saurabh; Xu, Zhuoqun; Gasques-Rodrigues, Danilo; Schulze, Jurgen P.; Tolley, Michael T. The dissertation author was the primary investigator and author of this paper.

VITA

2014	B. Tech. in Mechanical Engineering, University of Mumbai, Mumbai, India
2017	M. S. in Engineering Sciences (Mechanical Engineering), University of California San Diego
2021	Ph. D. in Engineering Sciences (Mechanical Engineering), University of California San Diego

PUBLICATIONS

Jadhav, S., Majit, M. R. A., Shih, B., Schulze, J. P., Tolley, M. T. , “Variable Stiffness Devices Using Fiber Jamming for Application in Soft Robotics and Wearable Haptics”, *Soft Robotics*, 2021.

Jadhav S., Glick P., Zhang Z., Ishida M., Chan C., Schulze J.P., Tolley M. T.,“ Dot-matrix display inspired fluidic circuit for distributed control of large array of actuators”, *In prep.*,

Jadhav S., Xu R., Gasques-Rodrigues D., Tolley M. T., Schulze J. P., “SpaceFrameVR: A virtual reality-based tool for design, analysis, and optimization of the automotive space frame chassis”. *In prep*, 2021

Jadhav S., Kannanda V., Kang B., Tolley M. T., Schulze J. P., (2017) “Soft robotic glove for kinesthetic haptic feedback in virtual reality environments”, *IS&T Electronic Imaging: The Engineering Reality for Virtual Reality* proceedings, IS&T Springfield VA, 2017.

Drotman D., Jadhav S., Sharp D., Chan C., and Tolley M. T., “Electronics-Free Pneumatic Circuits For Controlling Soft-Legged Robots”, *Science Robotics*, Vol 6, Issue 51, 2021.

Drotman D., Ishida M., Jadhav S., Tolley M. T., (2018), “ Application-Driven Design of Soft, 3D Printed, Pneumatic Actuators with Bellows” *IEEE Transactions on Mechatronics*, 24:1, pp. 78-87

Sandoval J., Jadhav S., Quan H., Deheyn D., and Tolley M.T., “Reversible adhesion to rough surfaces both in and out of water, inspired by the clingfish suction disc”, *Bioinspiration and Biomemetics* 14, 066016

Christianson, C., Bayag, C., Li, G., Jadhav, S., Giri, A., Agba, C., Li, T., Tolley, M. T. (2019), “Jellyfish-Inspired Soft Robot Driven by Fluid Electrode Dielectric Organic Robotic Actuators”, *Frontiers in Robotics and AI*, 6, 126.

Sandoval J., Ishida I., Jadhav S., Huen S., Tolley M.T., *“Morphological computation in suction discs enables directional adhesion for locomotion in wet environments”*, *Under review*

Minori A., Jadhav S., Chen S., Fong S., Tolley M.T., “Toward Artificial Muscles to Actuate Soft Jumpers using Snap-through of Shells” *In prep.*

Jadhav S., Chopra S., Dragos V., Gravish G., Tolley M.T., “Terrain-Structure Interaction: Framework for Simulation of Soft Bodies interacting with Granular media”, Conference, *In prep.*

Drotman D., Jadhav S., Karimi M., deZonia P., Tolley M. T., (2017) “3D Printed Soft Actuators for a Legged Robot Capable of Navigating Unstructured Terrain”, *Int. Conf. on Robotics and Automation (ICRA)*, Singapore, May 2017.

Minori A., Jadhav S., He Q., Cai S., Tolley M.T. “Reversible actuation of origami inspired composites using liquid crystal elastomers”, *Conference on Smart Materials, Adaptive Structures and Intelligent Systems*, Snowbird, Utah, Sept. 2017

Kalisky T., Wang Y., Shih B., Drotman D., Jadhav S., Aronoff-Spencer E., and Tolley M. T. (2017) “Differential Pressure Control of 3D Printed Soft Fluidic Actuators,” *IEEE/RSJ International Conference on Intelligent Robots and Systems (IROS)*, Sept 2017, pp. 6207–6213.

Chopra S., Jadhav S., Gravish G., Tolley M.T., “Mechanical and actuation asymmetry in soft appendages leads to robotic propulsion in granular media.” *Adaptive Motion in Animals and Machines*. Virtual, June 2021.

Chopra S., Jadhav S., Tolley M.T., and Gravish N., “Parapodia inspired soft appendages enable robot propulsion in granular media.” *Bulletin of the American Physical Society* (2021).

Hsaio J., Shih S., Jadhav S., and Tolley M.T., “Estimation of object stiffness using stiffness adjustable soft tactile sensor”, *In prep.*.

ABSTRACT OF THE DISSERTATION

Fluidically Driven Systems for Tangible and Interactive Media

by

Saurabh Jadhav

Doctor of Philosophy in Engineering Sciences (Mechanical Engineering)

University of California San Diego, 2021

Professor Michael T. Tolley, Chair

The possibility of augmenting existing 3D-interaction devices for virtual reality with haptic feedback has generated wide interest in the field of human-computer Interaction. Designing interaction devices for haptic feedback is challenging due to the densely packed mechanoreceptors on the skin distributed over a large surface area. The widely used solution for the design of haptic interfaces rely on solid-state electronic components such as piezoelectric actuators, voice coils, vibrotactile actuators, or electromagnets that are built with rigid materials. Integrating these electronic components with textiles to match the spatial density of the mechanoreceptors on the skin can cause discomfort. Additionally, the rigid nature of these devices can limit them from conforming to the complex topological surfaces of the human body. The emerging field of soft robotics has the potential to address these challenges by replacing traditional actuators with unconventional materials that have mechanical properties close to those of human tissue. Various actuation strategies in soft robotics (including pneumatic, hydraulic, thermal, and electromechanical actuation) have been previously presented for applications in haptic devices. Fluidic systems have been widely explored in haptics due to their ability to enable actuators with a ease of use. However, most fluidic systems control these actuators with individually addressable electromechanical valves, which make the system difficult to scale in number, to achieve the spatial density desired for haptic interfaces. Additionally, the nonlinear nature of elastomeric devices makes the stable, closed-loop control of such systems very complex. In this dissertation, I describe strategies to simplify the design and control of fluidically actuated systems to enable their application to wearable haptic interfaces and interactive media. First, I present the concept of "Fiber Jamming", a mechanism to achieve variable stiffness by controlling the input pressure in an actuator. I demonstrate the application of fiber jamming using open-loop control in a variable-stiffness haptic glove and a reconfigurable truss structure. Next, I present a dot-matrix-inspired fluidic circuit to individually address actuators in a large array. I demonstrate the application of the fluidic circuit using 10 electromechanical valves to individually address a 2D-Shape Display with 25 actuators. Additionally, I also demonstrate the application of the fluidic circuit to actuate a haptic vest with an array of inflatable pouches. Finally, I present strategies for the design and evaluation of 3D designs to overcome the limitations of the existing 3D-input devices to facilitate tasks requiring precision. I present a tool for three interaction in three dimensions for the design and prototyping of structures in engineering applications. The first two techniques demonstrate how the design and control of fluidic systems can be simplified without compromising their rapid rates of actuation and ease of use. The 3D-interface design and evaluation strategies present techniques to design and evaluate VR applications to enable precision tasks. Overall, the results demonstrate strategies for realizing ubiquitous tangible interfaces for applications in wearable haptic interfaces and exoskeletons.

Chapter 1

Introduction

Commercially available 3D input devices for interaction with virtual environments rely heavily on audio and visual stimuli as a form of sensory feedback to immerse the user and to generate a sense of presence. In the past decade, there has been a lot of research to improve this degree of immersion by augmenting synthetic haptic feedback during interaction in virtual reality (VR). The most common solutions for haptic interfaces initially focused on designing wearable, haptic feedback devices using electrical systems consisting of actuators like vibration motors, electromagnets, voice-coil actuators, piezoelectric actuators, and linear motors that are integrated into fabrics. These rigid actuators embedded into fabrics can be uncomfortable to wear and also have limitations in conforming to the complex topographical surfaces of the human body. Moreover, since these actuators are made from rigid materials, they form stress concentrations on the skin which fail to simulate a continuous stream of touch (e.g. like one experienced when gently stroking the skin). Soft robotics is a maturing field that has the promise to address these challenges by making use of unconventional materials with stiffness properties closer to those of human tissue. Pneumatically actuated soft robots have especially gained a lot of attention as compared to other methods of actuation(e.g., thermal, magnetic, electrical) due to the ability of pneumatic systems to generate rapid responses and systems with high ratios of force to weight ratio. In our previous work, we demonstrate a pneumatically actuated glove for kinesthetic haptic feedback in virtual environments (Fig 4.1). However, pneumatically actuated systems have the following challenges: a) Implementing a closed-loop system using fluidically actuated soft robots is challenging due to the lack of high-fidelity sensors to measure the deformation of such soft actuators; b) Scaling fluidic systems to control a large array of actuators desired in tactile interfaces is difficult as the number of electro-mechanical valves scales with the desired number of actuators; c) Designing 3D-user interfaces for precision tasks is challenging due to the low resolution of sensors and the controls used in such devices. My dissertation is designed to address these challenges by answering three research questions: (a) How to design a passive actuation system (like changing stiffness on the fly) using soft robotics to simplify or completely eliminate the need to use closed-loop control for haptic feedback? (b) How can we minimize the number of required valves to control a large array of actuators, and make the fluidic systems easily scalable? (c) How can the design of 3D-user interfaces support the limitations in the input devices to enable interaction required for tasks that require high-precision?

I test these questions using three different Human-Computer and Human-Machine Interfaces. In Chapter 2 on “Variable stiffness devices using fiber jamming for applications in soft robotics and wearable haptics” I present a pneumatically controlled phase change mechanism capable of withstanding versatile loading conditions, and demonstrate its application in a wearable glove for force feedback during interaction with augmented reality (AR). In Chapter 3, “A Dot-Matrix inspired Fluidic Circuit for Controlling a Large Array of Actuators”, I present a fluidic circuit inspired from a dot-matrix display to control a large array of actuators encountered in tactile feedback devices and shape displays. In Chapter 4, “SpaceFrameVR: A virtual reality-based tool for design, analysis, and optimization of the automotive space frame”, we present techniques for the design of 3D-user interfaces for activities like Computer-Aided Design (CAD) modeling that require higher precision as opposed to recreational interfaces (e.g., for gaming). I also present an evaluation of our interface using demonstrations and preliminary user feedback

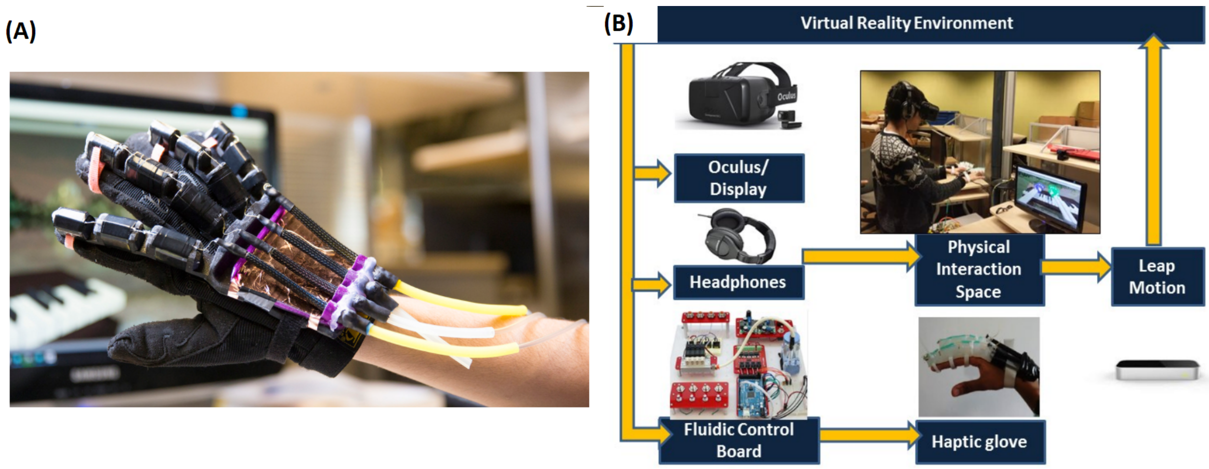

Figure 1.1: A) Fluidically actuated haptic glove for kinesthetic force feedback in virtual environments B) Block diagram of the fluidic system controlling the glove

Here we describe the main contributions and key results from each chapter:

1.0.1 Variable stiffness devices using fiber jamming for applications in soft robotics and wearable haptics:

Variable stiffness actuation has applications in a wide range of fields, including wearable haptics, soft robots, and devices for minimally invasive surgery. There have been numerous design approaches to control and tune stiffness and flexural rigidity; however, most have relatively low specific load-carrying capacities (especially for flexural loads) in the most rigid state that restricts their use in small or slender devices. In this chapter, we present an approach to the design of slender modules with high flexural stiffness based on the principle of fiber jamming. The proposed fiber jamming modules (FJMs) consist of axially packed fibers in an airtight envelope that transition from a flexible to a rigid beam when a vacuum is created inside the envelope. This FJM can provide the flexural stiffness of up to eight times that of a particle jamming module in the rigid state. Unlike layer jamming modules, the design of FJMs further allows them to control stiffness while bending in space. We present an analytical model to guide the parameter choices for the design of fiber jamming devices. Finally, we demonstrate applications of FJMs, including as a versatile tool, as part of kinesthetic force feedback haptic glove, and as a programmable structure. The kinesthetic force feedback-based haptic glove using fiber jamming enables a stable and robust haptic interaction. Additionally, the inherent passivity of the jamming mechanism enables stability even in the presence of quantization or delays in the position tracking.

1.0.2 A dot-matrix inspired fluidic circuit for controlling a large array of actuators:

Controlling a large number of individually addressable soft actuators is a challenging problem especially due to the increase in size and complexity of the system with the increase in the number of electromechanical valves. Previous work has demonstrated the use of pneumatically controlled logic devices to construct electronics-free circuits (similar to electrical transistors) which can completely eliminate the need for using electromechanical valves [2, 3, 4]. However, these electronics-free circuits reported can only execute a pre-programmed sequence and cannot be used to individually address the actuators as desired in the case of haptic interfaces and interactive media. Previous approaches (e.g., those modeled with demultiplexer circuits) led to slower refresh rates since they did not allow any operation that required multiple outputs to be pressurized simultaneously[5]. In this work, we present a pneumatic circuit inspired by a dot-matrix display for independent control of a large array of actuators. We demonstrate the application of this display for the rapid actuation of fluidic flip-flop elements as well as soft elastomeric actuators. The proposed method enables the user to control an entire set of actuators simultaneously enabling shorter refresh intervals for each actuator and thus high refresh rates for the entire fluidic display. We present a model to predict the dynamics of the fluidic circuit and demonstrate the application of our fluidic circuit to control a 2D-Shape display, a haptic vest, and an array of soft actuators.

1.0.3 SpaceFrameVR: A virtual reality-based tool for design, analysis, and optimization of the automotive space frame:

Mechanical design engineers today have limited tools for integrating virtual reality (VR) in their workflow, and the application of VR is restricted to the visualization of the 3D data generated using desktop-based CAD tools. Can 3D-interaction metaphors along with analysis tools help the engineers integrate VR in their product design process while preserving the creative freedom offered by VR? We interviewed design experts and identified recurring challenges for using VR for the design process: 1) a lack of VR-based tools for creating and manipulating the space frame design; 2) the absence of constraints for defining the space frame; and 3) the lack of structural and ergonomic analysis capabilities. How can the existing VR input devices with their inherent limitations be useful for precision tasks? Here we present SpaceFrameVR, a tool for the design, analysis, and optimization of space frame in virtual reality. The designer can use SpaceFrameVR to optimize the space frame design by minimizing the weight and lowering the center of gravity while checking for structural and ergonomic requirements. In this chapter we present the techniques for designing 3D-user interfaces to enable precision tasks and present strategies to evaluate system-level 3D user interface designs.

Chapter 2

Variable Stiffness Devices Using Fiber Jamming for Application in Soft Robotics and Wearable Haptics

2.1 Introduction

Variable stiffness actuation has proven useful in a wide range of potential applications in soft robots, medical devices, programmable and deployable structures, wearable exoskeletons, and energy-absorbing components.[6, 7, 8, 9, 10]. These applications require components to have both (1) high rigidity or stiffness during load-bearing conditions to resist shape change and (2) minimal rigidity during the flexible state to achieve the desired attribute (e.g., shape change, portability, or energy dissipation) as shown in Figure 2.1D–F. (3) Variable stiffness during operation can be achieved either using an electromechanically actuated kinematic mechanism [11, 12, 13, 14, 15, 16], or an active phase-change mechanism [17, 18, 19, 20, 21]. However, most electromechanical kinematic mechanisms contain rigid linkages and components that are not desirable for many applications (e.g., for wearable haptic devices). Thus, work in the emerging field of soft robotics has explored variable stiffness actuation using phase change mechanisms to control and tune stiffness.

The modulation of stiffness in soft robots is usually achieved using external stimuli (e.g. pressure, temperature, electric field, or magnetic field). For example, magnetorheological (MR) or electrorheological (ER) fluids that change viscosity in the presence of external magnetic or electric fields have been previously demonstrated for variable stiffness actuation in haptic gloves,[17] grippers,[18] prosthetics,[19] devices for minimally invasive surgery,[20] and soft robot locomotion [21]. However, phase change mechanisms using MR or ER fluids rely purely on tuning the viscosity or shear resistance of infill material and cannot withstand significant tensional and flexural loads during operation. Temperature-induced phase change using low melting point alloys, thermoplastic elastomers, or paraffin wax can achieve a large range of stiffness but suffer from latency in the phase change response [22, 23, 24]. Hence, many novel applications that require rapid response time use vacuum-induced phase change using “jamming” as a mechanism for variable stiffness actuation.

2.2 Variable stiffness using vacuum induced phase change

2.2.1 Granular jamming or particle jamming

Granular jamming can attain reversible phase change with very low latency ($\sim$ 1 s). Pressure-induced variable stiffness actuation using granular jamming has been widely demonstrated and tested for applications, including jamming skin-enabled mobile soft robots[24, 25], jamming feet for an enhanced robot [25, 26] mobility [26, 27], universal robotic grippers [28], medical devices, haptic interfaces [29, 30, 31], and reconfigurable and deployable load-carrying structures [31]. Steltz et al. and Cianchetti et al., have demonstrated granular jamming as an actuation method for achieving variable flexural stiffness in soft robotic devices.[25, 32] However, vacuum-packed granules are only capable of resisting compressive and shear stresses and are

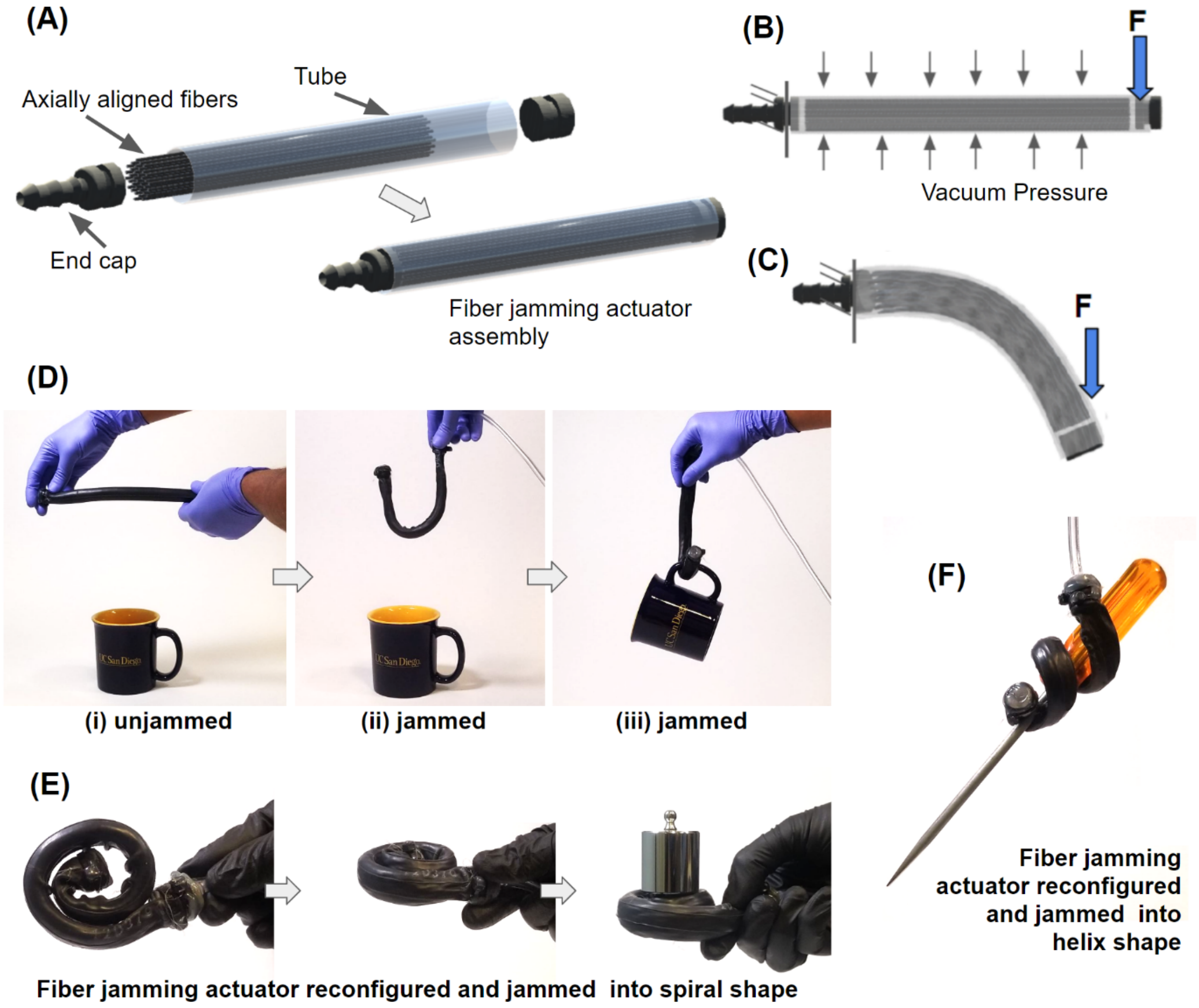

Figure 2.1: Fiber Jamming concept: (A) Schematic of the design and assembly of a FJM. (B, C) Quasi-static response of a FJM in the jammed and unjammed state. The bending stiffness of the FJM in the frozen (jammed) state (B) is significantly higher than the unjammed state (C). (D) Demonstration of a FJM as a morphable tool. The fiber jamming structure is manually deformable in the unjammed state (i); when the vacuum is applied the structure jams to behave like a rigid hook (ii, iii). (E, F) Versatility of a FJM to twist and bend out of a plane to carry eccentric and torsional loads. FJM, fiber jamming module.

unable to resist tensional forces [33] (Fig. 2.2A–H). If the tensional stresses at any point within the particle jamming devices exceed the vacuum pressure under bending loads, the particles will begin to dissociate (Fig. 2.2E). This inability of particles/granules to resist any significant tensile stress is one of the major drawbacks of granular jamming, which causes the design of haptic exoskeletons, soft robotic manipulators, and medical devices using particle or granular jamming to be bulky and weak to bending loads. In addition, the inability of particles to resist tensile stress during granular jamming causes the membrane stiffness of the jamming device to be a significant contributor to the overall stiffness of granular jamming devices [34]. These drawbacks due to the inability to resist tensional loads are addressed using variable stiffness composites using orthotropic material properties, presented in previous work on fiber and layer jamming (Fig. 2.2 B–D).

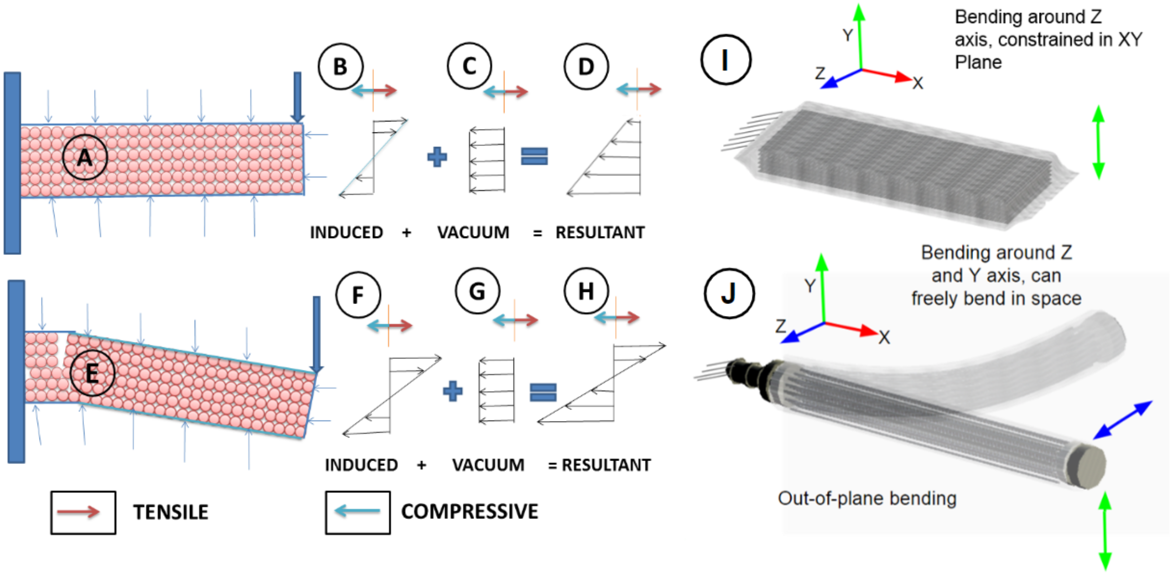

Figure 2.2: Advantages of fiber jamming-based variable stiffness devices relative to granular and layer jamming devices. Granular jamming: (A) The strength of particle jamming actuators in bending is limited by the tensile stresses induced in the beam. In the case where the induced tensile stress (B) is lower than the applied vacuum pressure (C), the resultant stress is compressive (D), and the particles remain packed (A). However, in the case where the induced tensile stress (F) is larger than the pressure of the applied vacuum (G), the resultant stress is partially tensile (H), and the particles lose contact and begin separating (I). Layer jamming: (E) For layer jamming devices, the bending is confined to a single plane. (J) Our proposed FJM design bends freely for about two perpendicular axes in the unjammed state.

2.2.2 Layer jamming

Layer jamming presents a solution for designing compact variable stiffness structures with orthotropic material properties that are optimized for the given loading conditions. Previous work has used stacked sheets to design layer jamming devices that allow bending in one plane in a soft state, but resist bending in a rigid state [35, 36]. Narang et al. presented layer jamming as a solution for designing high aspect ratio jamming devices and “jam-sheets.”[36] However, without twisting or buckling of the sheets (which could negatively impact stiffness control or device lifetime), the layer jamming configuration limits the motion of the device to a single plane (perpendicular to the sheets), which makes it unsuitable for applications that require the devices to bend in space like in an endoscope or a haptic glove (Fig. 2.2I) [37, 38]. Kim et al. presented a layer jamming structure that allows out-of-plane bending but requires complex assembly and manufacturing methods [39].

2.2.3 Fiber Jamming

This work presented in this article, as much of the previous work in variable stiffness actuation, is motivated by a specific application—wearable exoskeletons for haptic feedback in virtual environments. Previous work has demonstrated haptic devices using granular or layer jamming, which suffered from the inherent drawbacks of these technologies [37, 38]. For example, numerous designs for wearable and desktop-based haptic devices enabled by particle jamming have been demonstrated for rendering variable stiffness for haptic feedback in virtual reality (VR). Zubrycki and Grzegorz Granosik proposed a particle jamming-based wearable exoskeleton for providing kinesthetic haptic feedback by rendering virtual stiffness [37]. Simon et al. presented a jamming mitten for haptic feedback in VR. However, these wearable devices require the ability to resist bending force exerted by the fingers, which results in bulky designs that are not user-friendly [40]. Zubrycki and Grzegorz Granosik[37] and Yu et al.[38] have presented haptic glove designs based on layer jamming. However, to consistently control stiffness, haptic glove designs based on the principle of layer jamming constrain the finger and thumb to bend in a single plane. In addition, these designs are less adaptable to different hand sizes due to the inability of the layer jamming devices to consistently control stiffness while bending in space.

In this work, we demonstrate a variable stiffness device based on the jamming of elements with a form factor that lies between the particles of granular jamming and the sheets of layer jamming, namely fibers. The resulting fiber jamming modules (FJMs) (1) allow bending in space with similar flexibility along any longitudinal direction in the soft state (Fig. 2.2J) and (2) stick together to provide higher resistance to this bending (regardless of the bending direction) when a vacuum is applied. Creating a vacuum in the envelope of the FJM significantly increases the frictional force between the fibers causing the FJM to act as a rigid beam (until the point that induced shear stresses to exceed the frictional forces). The ability of the fibers to resist tensional stresses during bending in the transverse direction makes it possible to design devices that are slender and have a high aspect ratio. Brancadoro et al. presented a comparative study on cylindrical fiber jamming devices followed by an application in a surgical manipulator[41, 42, 43]. However, the design of fiber jamming devices presented in previous work was guided by empirical results based on experiments[41, 42, 43]. Previous work has not studied the relationship between the different design parameters of the FJM on its performance, thus making the design of fiber jamming devices a laborious process [43]. Vasios et al., have presented a numerical approach based on 3D finite element methods for predicting the response of fibrous and granular media[44]. Although such finite-element simulation is suitable for accurately predicting the response of fiber jamming, it is cumbersome to use for preliminary design as the analysis is specific to a single design [44]. Such a finite element modeling approach is also computationally expensive and not scalable due to the increase in the contact boundary conditions with the increase in the number of fibers or layers. Hence, the lack of a physics-based model to guide the design of the FJMs is a challenge for the optimization of these modules. Furthermore, previous work has not yet explored how fiber jamming can be used for applications such as manipulation tools, wearable haptic devices, and reconfigurable structures.

In this article, we present the application-driven design and modeling of a slender, variable stiffness module using fiber jamming to achieve a wide range of tunable flexural stiffness and demonstrate its application in soft robotics and wearable haptics. Our article makes the following contributions to the research in soft robotics with a specific application in variable stiffness devices—(1) Design and Fabrication: We propose a design of FJMs consisting of axially oriented fibers enclosed inside a thin cylindrical envelope (Fig. 2.1A). Our fabrication approach for the FJMs is rapid and using off-the-shelf components, which also makes it convenient for mass production. (2) Modeling and Experimental Characterization: We use a physics-based empirical model to understand the relationship between key design parameters of the FJM, to optimize its performance for specific applications. Our study, for the first time, presents rigorous experimental testing supported by a model for "fiber jamming" to study the effects of the critical design parameters on the performance of the FJM. (3) Applications: We demonstrate the ability of FJM to resist versatile loading conditions, including high flexural and buckling loads (Fig. 2.1B–F). We demonstrate the implementation of fiber jamming to overcome the shortcomings of previous jamming approaches in soft robotic applications. We demonstrate the application of fiber jamming in a kinesthetic force feedback haptic glove for grasping objects in augmented reality (AR) and also demonstrate a shape-shifting and deployable truss structure using FJMs.

2.3 Results

2.3.1 Experimental Characterization of FJM

The FJM assembly consisted of a polyisobutylene (butyl rubber, or PIB) envelope filled with axially oriented fiber bundles (Fig. 2.1A). The PIB tube assembly encasing the fibers was capped at both ends to make an airtight chamber connected to a vacuum pump. For modeling

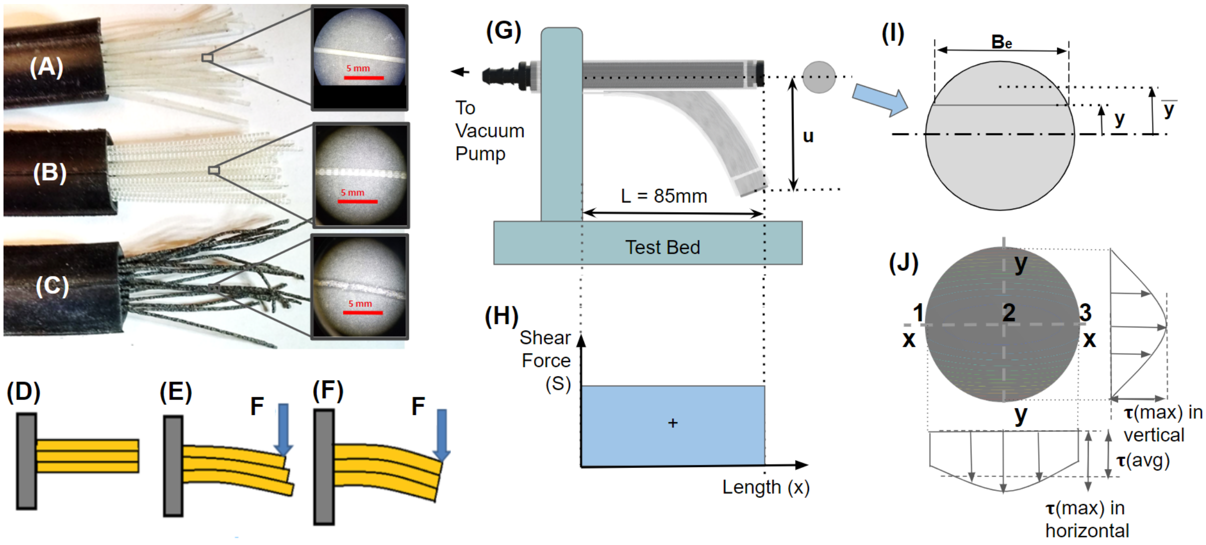

Figure 2.3: Analytical modeling and experimental characterization of FJMs: Image of the end of the FJMs with various fiber materials, including (A) Smooth, 3D Printed fibers, (B) 3D Printed fibers with surface texture, and (C) abrasive cords along with the magnified view. (D–F) The fundamental principle of operation for fiber/layer jamming structures. (D) Layers stacked together in the configuration of a cantilever beam. (E) When the layers are unconstrained, the externally applied force causes the layers to bend and slide relative to each other. (F) When sheets are bonded together, the overall stiffness of the cantilever beam increases. (G) Setup for cantilever beam bending test for the FJMs along with the shear force diagram for a cantilever beam with a point load at the end (H). (I) Schematic of the cross-section defining the terms in Equation (1). (J) Variation in transverse shear stress along the major and minor axis of the elliptical cross-section of the beam. Note that the shear stress varies slightly in the horizontal direction along the neutral axes (major axis) of the beam. The transverse shear stress formula assumes that this variation of shear stress in the horizontal direction is negligible and calculates the average value of the shear stress.

purposes, we assumed that the PIB tube had a negligible effect on the overall performance of the FJM. We fabricated the FJMs with three different kinds of fiber infill materials: (1) 3D printed fibers with a texture, (2) smooth 3D printed fibers, and (3) commercially available aluminum oxide abrasive cords with 180 grit (Mitchell Abrasives) (Fig. 2.3A–C). We experimentally determined the friction coefficient for the fibers using a sliding friction test between two frictional plates with similar fiber material. The packing volume for each FJM was empirically determined using a simple experiment (Supplementary Fig. A.4; see Supplementary Data section for details).

We characterized the performance of the FJMs using a beam bending test consisting of a cantilever beam with a point load at the tip of the module (Fig. 2.3D–G). This loading case represents worst-case loading conditions for applications such as the variable stiffness haptic glove demonstrated in this article (Fig. 2.3G, H). We characterized the force-deflection relationship of the FJMs and compared them to granular jamming modules of the same size and form (using ground coffee and plastic pellets as the infill material). We tested the FJM with different actuation pressures, infill materials, and tube sizes. From experiments, we observed that the FJM is capable of providing flexural stiffness of up to eight times that of the granular jamming device of the same form and size, and as a result, fiber jamming is useful in a variety of applications requiring a wide range of variable bending stiffness.

2.3.2 Design and modeling of FJM

The previous work has presented a 3D finite-element-based numerical approach for predicting the response of fibrous and granular media [44]. Although such finite-element simulation is suitable for accurately predicting the response of fiber jamming, it is cumbersome to use a finite-element-based approach for preliminary design and the development of intuition. In addition, it is cumbersome to use a finite-element approach for optimization since each analysis is specific to a single design. Hence, previous work on the design of fiber jamming devices was guided by empirical results based on experiments. Our article mainly focuses on a physics-based model that studies the relationship between the different design parameters on the performance of the FJM. In this article, we propose a reduced-order model that studies the relationship between the different design parameters of FJMs for application-driven design and optimization of soft robots.

Calculation of force for slipping transitions: We modeled the FJM at the macroscopic level as a single beam. Figure 2.3D–F describes the working principle for layer and fiber jamming. Applying an external shear force induces transverse shear stress within the beam (Fig. 2.3H). In the case of FJM, the friction between the layers resists the transverse shear stress. Applying a differential pressure along the membrane of the FJM increases the frictional resistance, which then increases the resistance of the module to transverse shear stress.

We can approximate the shear stress distribution across the elliptical cross-section with some basic assumptions regarding the stress distribution. The flexural formula used to derive the average shear stress has some characteristic assumptions and limitations. First, we assume that the shear stress always acts parallel to the y-axis throughout the cross-section of the beam (Fig. 2.3I)[45]. Second, the shear stress along the horizontal direction of the beam can vary slightly, and the formula to calculate the average shear stress is based on the assumption that the shear stress distribution along any horizontal section is uniform (Fig. 2.3J). As long as the height of the beam is greater than its width, the shear stress varies only slightly along the horizontal direction, and the average shear stress can be used to approximate the shear stress at any point along the horizontal width of the section (Fig. 2.3J). However, most of the fiber jamming devices we tested have a higher aspect ratio in the horizontal direction. Hence, we introduced a correction factor (kcorrection) to eliminate any error in the shear stress calculation due to the large variation in the aspect ratio of the cross-section. We calculated this correction factor using finite element analyses. Considering these assumptions, the formula for the average transverse shear stress that is induced in a beam with the second moment of area I_e, at any location along the beam where the shear force is S, at a distance of y parallel to the neutral axis along the cross-section of the beam (Fig. 2.3I) is given by:

$$\tau_{induced} = k_{correction} \times \frac{S A_e \hat{y}_e}{I_e B_e} \tag{2.1}$$

where A_e is the area of the cross-section beyond the section at a distance of y away from the neutral axis, y_e is the centroid of that area away from the neutral axis, and B_e is the width of the section at a distance of y from the neutral axis. The accuracy of the above shear stress formula depends on the aspect ratio of the cross section of the ellipse. For very high aspect ratios, $\tau_{induced}$ at X2 (Fig. 2.3G) is much greater than at $\tau_{induced}$ X3 and X1 (Fig. 2.3G), and hence, we can no longer assume that the shear stress is uniform along the width of the section. For such cases, we can multiply the average shear stress obtained using the above formula by a correction factor ($k_{correction}$). For a FJM, slipping between the fibers should start when the induced value of shear stress $\tau_{induced}$ is greater than the maximum transverse shear resistance $\tau_{resistance}$ due to frictional forces between the fibers. Hence, the condition of slip is given by:

$$\tau_{induced} > \tau_{resistance}. \tag{2.2}$$

We modeled the transverse shear resistance per unit area at any section at a distance of y from the neutral axis in terms of the frictional forces in that area.

$$\tau_{resistance} = \frac{\mu_s N}{A_y} \tag{2.3}$$

where μ_s is the static coefficient of friction between the fibers, N is the normal force, and A_y is the transverse area of the cross-section for the beam at the section that is distance y from the neutral axis. However, we know that the normal force N is given by the product of the differential pressure used for jamming (ΔP) and the projected area of the cross-section of the beam (A_p) at a distance of y from the neutral axis. By definition, $A_p = A_y$. Hence, we get transverse shear resistance per unit area:

$$\tau_{\text{resistance}} = \mu_s \Delta P \tag{2.4}$$

We estimated the area of the elliptical cross-section by taking into consideration the volume occupied by the fibers and the packing factor for the fibers calculated based on a simple experiment. We used the estimated area of the elliptical cross-section and the circumference of the outer envelope to calculate the major axis ($2a*e$) and minor axis ($2b*e$) of the elliptical cross-section. We tested the FJM for three different tube sizes. For an elliptical cross-section, the maximum transverse shear stress is at the neutral axis, at $y = 0$. Hence, using Equations (1)–(4), we get the condition for the minimum transverse frictional shear resistance for FJM to avoid slipping:

$$\mu_s \Delta P = k_{correction} \times \frac{4S_1}{3\pi a_e b_e} \tag{2.5}$$

Equation (5) can be used to estimate the force S1 required to initiate slipping along the elliptical cross-section of the beam at the major axis of the ellipse (Fig. 2.4A, B). Immediately after the slipping motion between the fibers starts at the neutral axis, the system acts like two semielliptical beam sections sliding relative to each other at the contact interface along the major axis of the ellipse (Fig. 2.4A, C-II). The semielliptical sections of the beam also experience traction force due to Coulomb friction at the contact interface (Fig. 2.4A, C-II). The traction at the sliding interface is directly proportional to the product of the kinetic coefficient of friction of the fiber material and the vacuum pressure P. The kinetic coefficient of friction influences the response of the FJM for any subsequent slipping transition. The distribution of shear stress after the beam splits into two semielliptical cross-sections sliding along the contact interface is a combined effect of the shear stress that is induced to overcome traction and the shear stress that is induced to resist further slipping within each semielliptical cross-section for any additional load applied (Fig. 2.4C-III).

Additional slipping between the fibers will occur within the two semielliptical cross sections simultaneously when the induced shear stress exceeds the transverse shear resistance $\tau_{resistance}$ due to frictional forces between the fibers (Fig. 2.4C-III). If the kinetic and static coefficient of friction for the fibers is approximately equal (e.g., stick-slip behavior in the case of sandpaper, refer to the Empirical Determination of the Coefficient of Friction for the Fiber Material section in Supplementary Data for more details), then the traction at the sliding interface of the two beam sections is equal to the shear stress that is induced to initiate slipping ($\mu_s \Delta P$). In this case, the total shear stress $\tau_{induced}$(total) is maximized at the sliding interface, and the slipping penetrates from the neutral axis to the outermost fibers upon subsequent loading. Hence, if $\mu_s = \mu_k$, the slipping will transversely propagate from the neutral axis to the outermost fiber of the ellipse (Fig. 2.4C-III), and the transition in the Force versus Deflection curve is continuous (Fig. 2.4B). This transition is observed with abrasive cords as infill material since the abrasive cords demonstrate stick-slip behavior during sliding, and their kinetic and static coefficient of friction for the fibers is approximately equal (Fig. 2.5A).

If the kinetic friction coefficient is lower than the static friction coefficient ($\mu_s >> \mu_k$, e.g., textured fibers, see Empirical Determination of the Coefficient of Friction for the Fiber Material section in Supplementary Data and Supplementary Fig. A.3 for more details), the force-deflection response of the fiber jamming devices is more complex involving the beam splitting into multiple sections. In the case of $\mu_s >> \mu_k$, for the scope of this article, we approximate the stiffness of FJM in the post slip regime for as constant and equal to the stiffness after the slipping is initiated at the neutral axis.

The calculated slipping forces for relative vacuum pressures of 90 and 45 kPa applied inside FJMs with 3D printed fibers and abrasive cord as infill are presented in Figure 2.5A and B. Figure 2.5 C presents the calculated slipping forces for three different tube/module sizes for textured 3D printed fibers at a 90 kPa vacuum. Figure 2.5D presents the effect of different coefficients of friction at a 90 kPa vacuum in contrast with the particle jamming modules. We compared plots for Force versus Deflection in each case with our analytical prediction obtained using numerical methods (see Supplementary Data for more details). The Force versus Deflection plots for smooth 3D printed fibers as infill with the calculated slipping forces are represented in Supplementary Figure A.7(A). Supplementary Figure A.7(B) represents the representative trials for fiber jamming beam in three-point bending. We also compare the fit obtained using the analytical model presented in this article with the experimental results for fiber jamming presented by Brancadoro et al. [43] in Supplementary Figure A.8.

Calculation of pre and post slip flexural stiffness of FJM The instantaneous stiffness of the FJM at a given point during loading in the Force-deflection curve can be approximated by the total stiffness of slipped sections of the beam in parallel (represented as springs). If the deformation is before the slipping transition (i.e., the induced shear stress is below the maximum shear stress for the applied vacuum), we model the system as conservative (i.e., the fiber modules will return to their initial position when they are released; Fig. 2.4C-I). In this case, the FJM can be represented with a cantilever beam with equivalent stiffness as previously proposed by Brancadoro et al[42]. We modeled the cantilever beam with a point load F at the end as a spring with stiffness K, and the force F is acting on the beam as shown in Figure 2.4. The deflection of the tip of the beam (u) when the force F is under the first slipping force ($S1$) can be calculated using the flexural stiffness of the beam and force acting on the beam (Fig. 2.4C-I).

$$F = K_{ellipticalbeam} \times u \tag{2.6}$$

We empirically obtained the initial flexural stiffness for the jammed cantilever beam in each case by fitting the initial section for the Force versus Deflection curve before the predicted slipping force $S1$ Once the slipping between the layers starts at the neutral axes of FJM, any subsequent force applied to the cantilever beam causes the upper and lower semi-elliptical section of the beam to slide relative to each other. The bending stiffness of the FJM at slipping is modeled as two beams with half elliptical cross-section bending together with the load applied shared between the two beams. We model the instantaneous stiffness of the FJM after slipping as two beams (the upper and lower halves of the elliptical cross-section) with bending stiffness $K1$ and $K2$ parallel to each other (Fig. 2.4C-II). By Parallel Axis Theorem, the second moment of area of half ellipse about its centroid at a distance of $2b/3\pi$ from the neutral axes is given by:

$$I_{NA} = \frac{\pi ab^3}{8} - \frac{\pi ab}{2} \times \left(\frac{4b}{3\pi}\right)^2 \tag{2.7}$$

From Equation (6), the stiffness of beam after slipping starts (at $F = S1$) is given by:

$$dF/du = 6EI_{NA}/L^3 \tag{2.8}$$

Hence from Equations (7) and (8), we can calculate the ratio of stiffness of the FJM before and after slipping. Using a similar approach, we can calculate the equivalent flexural stiffness of the FJM for any additional load beyond the slipping (Fig. 2.4C-III). Trapezoidal rule was used to estimate the centroid and second moment of area for each constituent beam (Supplementary Fig. A.5). When the static and kinetic coefficient of friction is similar (Fig. 2.4C-III), we approximate the equivalent stiffness of the beam as two beams of bending stiffness $K1$ and $K2$ acting in parallel since the bending stiffness of the section along the neutral axes where slipping has initiated is negligible. Hence, the instantaneous stiffness of the fiber jamming device in the postslip regime that is separated into N parallel sections is given by:

$$K_{inst} = \frac{dF}{du} = \frac{3E}{L^3}\sum_{i=1}^{N}(I_{NAi}) \tag{2.9}$$

where K_{inst} is the slope of the force-deflection response of the fiber jamming device in the post slip regime, and I_{NA} is the second moment of area of each separated section of the beam bending in parallel. When the kinetic coefficient of friction is negligible (as in the case of textured and smooth 3D-printed fibers), we can approximate the equivalent stiffness of the beam as multiple beams of bending in parallel, where the stiffness of each beam is proportional to its composite cross-sectional inertia.

The first-order modeling approach presented in this article can also be adapted for the fiber jamming structures bending in complex shapes (Fig. 2.6). A finite element model using beam elements can be used to calculate the maximum shear force in the FJMs for applications requiring the FJMs to bend in complex shapes. For example, we calculate the maximum shear force acting on the FJMs used for the demonstrations shown in Figure 2.1 using a commercial finite element tool. This maximum shear force can be used further in the analytical model to calculate the critical design parameters for the fiber jamming device. If the shear force at any point in the module exceeds the maximum shear stress that the fibers can resist, the FJM will undergo a slipping transition and would fail to resist the loading condition. The first-order modeling approach presented in this article can also be used to approximate the toughness of the fiber jamming device using the area under the force-deflection curve. The toughness of the FJMs is especially useful for the design of fiber jamming devices subjected to impact loading.

2.4 Design and fabrication of fiber jamming based haptic glove

We demonstrated the application of the FJM in a variable stiffness haptic glove for kinesthetic force feedback while grasping in Virtual or AR environments (Fig. 2.7A, B). Previous designs of particle jamming-based haptic gloves are bulky and cannot render high reaction forces Using fiber jamming allows us to fabricate slender modules which allow bending for about two perpendicular axes and enable the glove to accommodate different hand sizes. The actuation of the FJMs used in the haptic glove is controlled using a fluidic control system (see Control of the Pneumatic System section in Supplementary Data and Supplementary Fig. A.1). We created an AR application where a user wearing an AR headset (Meta2, Meta) could grab virtual balloons floating around them. When the user grabbed a balloon, the glove was actuated and the finger motion was constrained thus providing kinesthetic force feedback to simulate the balloon Figure 2.7C–E. The sudden loss of stiffness when the balloon was taken near a sharp object (along with audio feedback) simulated the balloon popping.

The design parameters for the fiber jamming haptic glove included the diameter of the outer tube envelope, length of the module, type of infill fiber material, coefficient of friction of the fibers, and actuation pressure. The selection of these parameters was made based on the analytical model presented here (along with the ergonomics of the hand). The dimensions for the assembly of the haptic glove, including the length of the module and spacing between the modules, were calculated to accommodate hands up to the 95th percentile in size, as shown in Figure 2.7B. The maximum diameter of the FJM was limited by the width of the finger. The positioning of the FJM in the glove worn on the user's hand was approximated as a cantilever beam (Fig. 2.7G, H) with a length of 85 mm based on the 95th percentile anthropometric data [45]. We chose the maximum fingertip force to render as 7 N based on the previous force feedback glove designs [46]. Equation (5) guided the design choice for the infill ratio and choice of infill material for the module to resist the force of 7 N without undergoing a slipping transition. The maximum stiffness of the virtual object was rendered by the FJM in the jammed state before slipping transition was calculated using Equation (6). We chose FJM with textured 3D printed fibers as infill material for the haptic glove due to its lower initial stiffness for the haptic glove in the unactuated state compared to abrasive cords as infill. FJM beams were attached to the hand at an angular offset to reduce the stiffness of the module perceived by the user when the fist is open, and there is no stiffness being rendered (Fig. 2.7F). The design of haptic glove using FJMs allows the control of stiffness in all directions during operation, while the user explores the virtual space (see Fabrication of Fiber Jamming Based Haptic Glove and Morphing Structure section in Supplementary Data and Supplementary Fig. A.6). Preliminary user feedback suggests that the FJMs were effective in simulating the size of the virtual object. However, we leave a detailed investigation and full user study for future work.

2.5 Design and fabrication of fiber jamming based haptic glove

Previous research has explored granular jamming for applications in deployable and reconfigurable structures, including cast concrete structures, reconfigurable carports, and deployable bridges [31].We present the implementation of FJM to design portable, deployable, and lightweight reconfigurable truss structures. In Figure 2.8A–C, we demonstrate a deployable tetrahedral morphing truss structure with a high load-carrying capacity. A previous shape-shifting truss structure was constructed using beams made of granular material, which made the structure bulky with high aspect ratio columns and occupied a large volume in the flexible state. By contrast, fiber jamming enables the design of slender members with a higher load-carrying capacity, thus providing more internal space within the truss. The truss structure could be folded into a small confined volume when not in use and deployed to act as a load-bearing component with the modules jammed. The FJM is versatile and can be programmed into any form, as demonstrated in Figures 2.1, 2.6, and 2.8. For the tetrahedral truss structure with point load, the transverse load acting on its members was negligible compared to the axial load. Hence, the main failure mode for the structure was the buckling of the inclined members (Fig. 2.8D–F). In the unjammed state, the axial load acting on the members was carried by individual fibers separately and the column buckled easily (Fig. 2.8B). However, in the jammed state, the fibers together acted as a single column, increasing its load carrying capacity significantly (Fig. 2.8A). Knowing critical design parameters for the FJM it is possible to calculate the critical buckling load for the module. However, we leave the detailed investigation of FJM in buckling for future work.

We have also demonstrated load-bearing components with programmable shape and stiffness using fiber jamming activated by thermal stimuli instead of vacuum. Figure 2.8G-I shows fibers bundled in a hook shape within a heat-shrink envelope. For this demonstration, the hook shape was manually programmed in the soft state and fiber jamming was activated using thermal stimuli to increase the stiffness. Although actuation using heat shrink is irreversible, reversible smart materials (e.g., shape memory alloys1) could enable similar reversible fiber jamming without pneumatics. The pressure applied by the heat shrink on the enclosed fibers in the activated state can be calculated using the formula for hoop stress. After calculating the equivalent pressure applied by heat shrink, one could use an approach similar to that presented in the article to calculate the performance of the FJM.

2.6 Materials and Methods

We have explained the details of the design, modeling, and experimental characterization in the Supplementary Data section. To facilitate navigating the Supplementary Data section, we list the parts of the Supplementary Data section here:

2.6.1 Design of the fiber jamming devices:

FJM fabrication and assembly The FJM assembly consisted of a butyl rubber or PIB envelope filled with axially oriented fiber bundles (see Supplementary Table S1 for more details on the outer envelope). Three different kinds of fibers were used as infill material: 3D printed fibers with a texture, smooth 3D printed fibers, and commercially available aluminum oxide abrasive cords with 180 grit (Mitchell Abrasives). We fabricated the 3D printed fibers out of a rigid but thin photopolymer (VeroClear RGD810; Stratasys) using a commercial 3D printer (Connex3 Objet350; Stratasys).

Design parameters: FJM sizes The size of the FJMs (major and minor axis of the elliptical cross section) was calculated based on the size of the tube (tube circumference) and the amount of infill (number of fibers). The FJM collapses into an elliptical cross section when a vacuum is applied. The circumference of the ellipse is equal to the circumference of the tube [see Supplementary Table S1 for the tube sizes used; Eq. (S1)], and the area of the cross section of the ellipse is equal to the amount of infill of fibers in the module.

Coefficient of friction for fibers The coefficient of friction for 3D printed fibers was experimentally determined using a sliding friction test between two frictional plates with similar fiber material (VeroClear RGD810) and texture (smooth and square wave texture) on the surface of the plates (Supplementary Fig. A.3). We determined the coefficient of friction between the abrasive cords using a sliding friction test between sandpapers made of similar material (aluminum oxide) and grit size (180) (Supplementary Fig. A.3). We used a single sample test with a minimum of seven trials for each case. Supplementary Table S2 presents the results from the experiment for calculating the coefficient of friction for each fiber material.

2.6.2 Experimental characterization

We fabricated the fixtures for bending test using a commercial stereolithography 3D printer (Form2, FormLabs), mounted the test setup on a mechanical testing machine (3342, Instron, Inc.), and characterized the force-deflection relationship of the fiber jamming devices. We tested the FJM with different fiber infill, tube sizes, and actuation pressure. We used a single sample test with a minimum of seven trials in each case for the jammed state (90 and 45 kPa), and a minimum of three trials for the unjammed state (0 kPa). The pressure inside the FJM was controlled using a bleed valve connected in parallel to the FJM.

2.6.3 Analytical modeling

Limitations of analytical model The physics-based empirical model presented in this article is a piece-wise linear approximation that can be used for a preliminary investigation of the relationship between key design parameters on the FJM performance. This first-order approximation can be used to guide the design choices of the fiber jamming devices.

In the post-slip regime, the model ignores any effect of frictional dissipation or traction along the cohesive longitudinal sections of the beam undergoing slipping transitions. The model assumes that the resistance to bending is mainly caused by the flexural stiffness of the cohesive sections of the beam and assumes the resistance due to traction between these sections to be negligible (Supplementary Fig. A.2). For fiber materials with a low frictional coefficient, the FJM will undergo slipping transitions at relatively lower shear force, and the resistance to bending due to the traction between the layers will dominate in the post slip regime (Supplementary Fig. A.2). Hence, in the case of the fibers with a low coefficient of friction, the model will deviate for large displacements in the post slip regime (see Assumptions in the Analytical Model section in Supplementary Data).

Empirical calculation of initial bending stiffness and correction factors of the FJM The initial bending stiffness of the FJM was calculated empirically by fitting the initial half region of the Force-Deflection curve under the calculated slipping transition force S1. To minimize the error due to the assumptions in the analytical model, the correction factor for each sample is empirically calculated using ANSYS as described in Supplementary Table S7.

Numerical and computational methods The Slope versus Deflection curve for the regime after slipping starts was numerically calculated. The trapezoidal rule was used to estimate the cross-sectional moment of inertia after the slipping transition. Please refer to Numerical Simulation to Calculate the Moment of Area section in Supplementary Data for more details [Supplementary Eqs. (S3)–(S6)].

Chapter 2, in full, is a reprint of the material as it appears in Soft Robotics, 2021. Jadhav, Saurabh; Ramzi Majit, Mohamad Abdul; Shih, Benjamin; Schulze, Jurgen P.; Tolley, Michael T., Soft Robotics 2021. The dissertation author was the primary investigator and author of this paper.

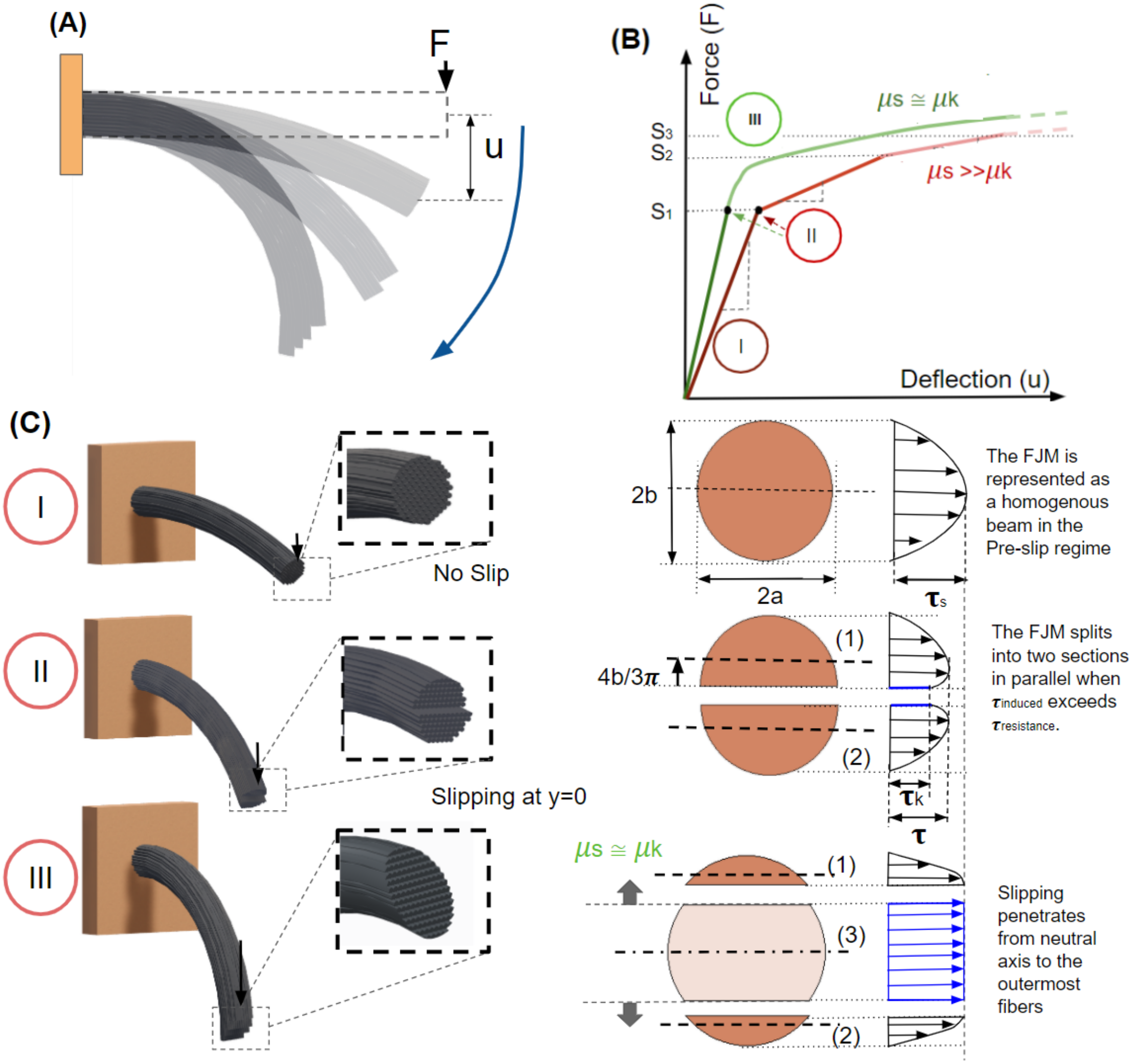

Figure 2.4: Illustrative schematics for analytical modeling of FJM: (A) Side view of a cantilever beam with slipping transitions. (B) Illustrative Force versus Deflection plot for FJM as a cantilever beam. (C-(I)) The fibers adhere together to behave as a single beam before slipping transition. (C-(II)) Slipping of fibers starts relative to each other at the locations of the beam where maximum shear stress exceeds the resistive shear stress during bending. After slipping transition, the FJM behaves as an assembly of independent beams in parallel (blue region indicates stress to overcome traction) (C-(II)), (C- (III)). Subsequent slipping transition behavior after S1 will vary based on the ratio of kinetic to the static coefficient of friction. In the case where static friction is equal to kinetic friction coefficient (as in the case of abrasive cords), the instantaneous stiffness of the FJM gradually decreases for any increase in force above the slipping force (S1).

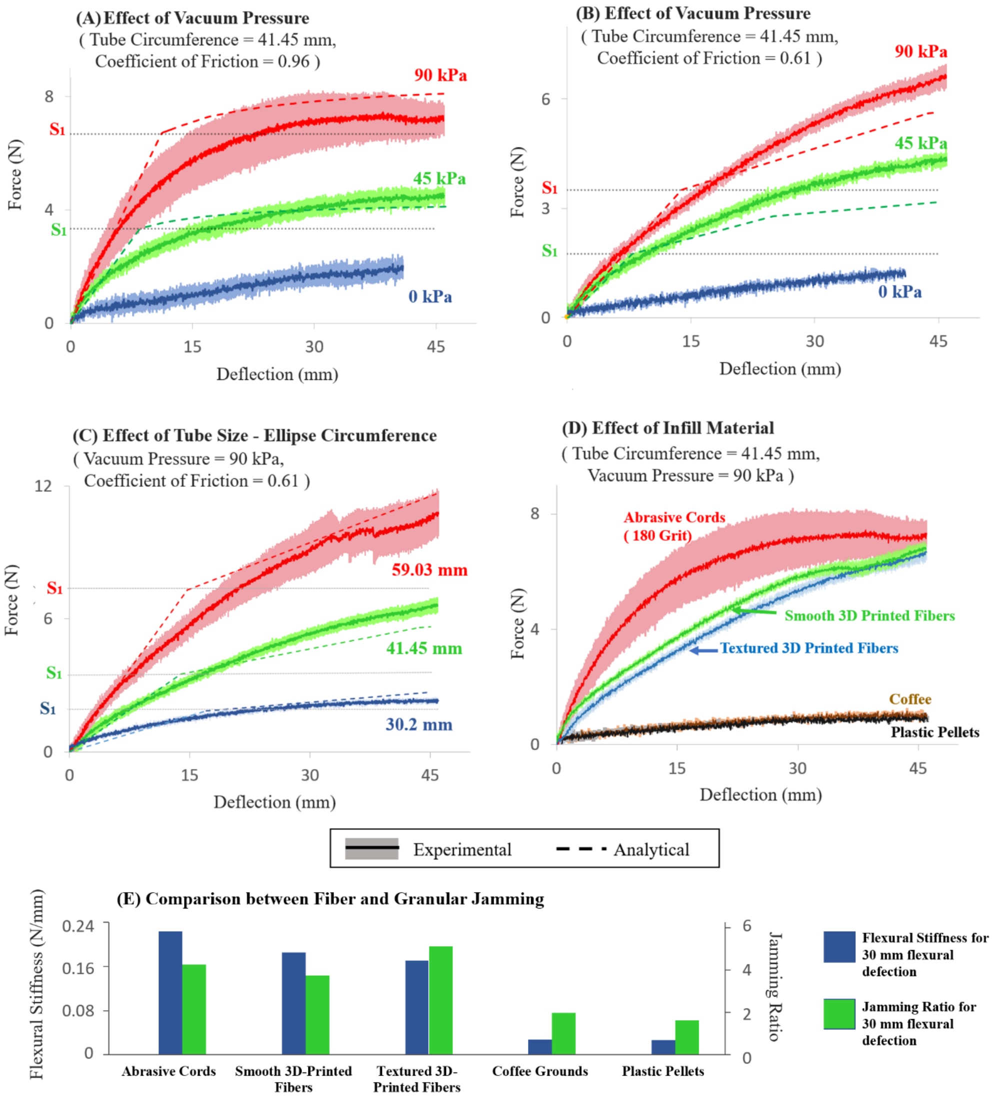

Figure 2.5: Analytical fits and experimental validation of the Force versus deflection plots from beam bending tests of the FJM: Force versus deflection at 90, 45, and 0 kPa for abrasive cords (A), 3D printed fibers with texture (B). Force versus deflection plots from beam bending tests for FJMs with varying tube sizes (C) and varying coefficients of friction for fiber material along with the comparison of the FJMs with granular jamming devices of the same size and form (D). (E) Comparison of the absolute flexural stiffness and jamming ratio for the jamming devices with different kinds of infill in a cantilever beam configuration at 30 mm flexural deflection. Note that the force for slipping transition (S1) increases proportionally with the increase in vacuum pressure, cross-section area, and coefficient of friction. From (E), we see that the FJMs can provide up to eight times the absolute flexural stiffness compared to particle jamming devices in the jammed state. The shaded region represents $1-\sigma$ (67% confidence interval).

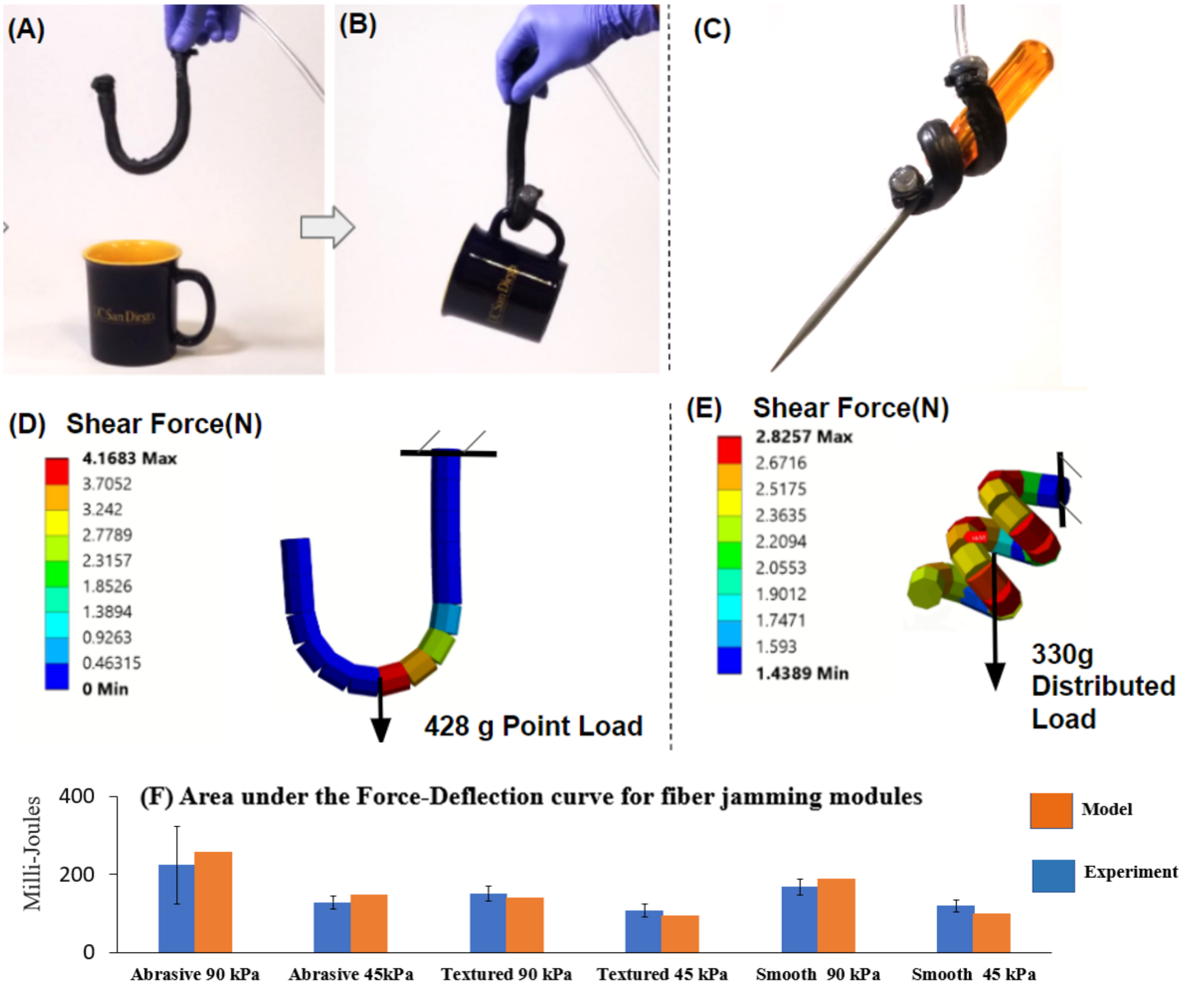

Figure 2.6: Adaptation of the analytical model for the design of fiber jamming structures under complex loading conditions (A), (B) The FJM is bent into a hook shape and subjected to carry a load of 428 g. (C) The FJM is formed into a helical shape to carry a load of 330 g. (D) For the boundary conditions given in (A)& (B), a maximum shear force of 4.16 N is induced in the hook-shaped module. (E) For the boundary conditions are given in C, a maximum shear force of 2.82 N is induced in the helical-shaped module. These maximum shear force values obtained from F.E. analysis can be used as a design input to size the FJMs and operate in the preslip regime. (F) Comparison of analytical prediction for the area under the Force-Deflection curve for FJMs with the results obtained using experiments within ±3σ. This area under the Force-Deflection curve can be used to calculate the toughness of FJMs for applications with impact loading conditions. FE, finite element.

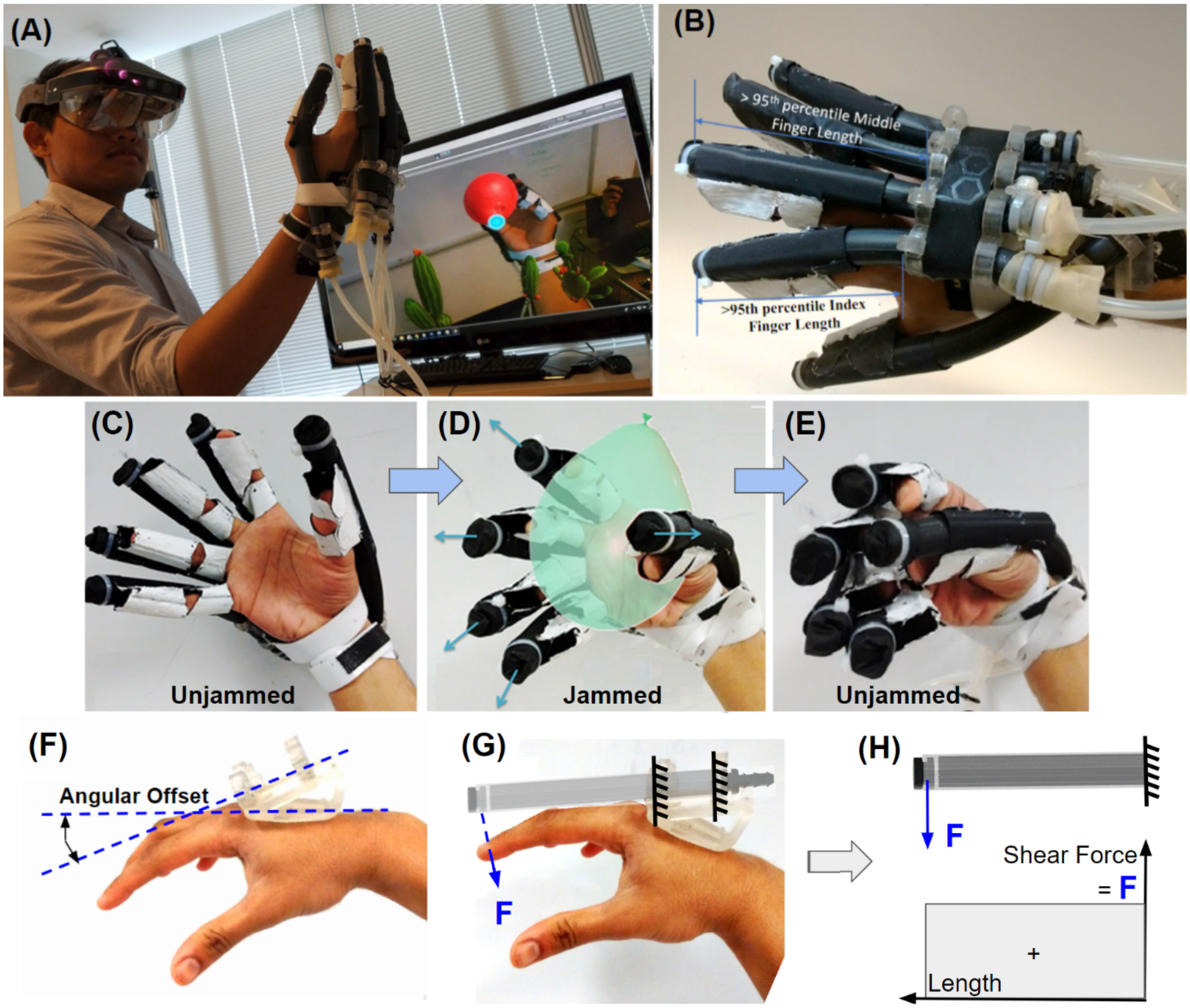

Figure 2.7: Demonstration of the FJM in kinesthetic force feedback haptic glove. (A) Demonstration of the haptic glove using a commercial AR headset. (B) Design and assembly of the haptic glove—the length of the FJMs for the glove was calculated to accommodate hands up to the 95th percentile in size. The FJMs were able to bend out of the plane to accommodate different hand sizes. (C) The unjammed haptic glove allows uninhibited motion of fingers. (D) The haptic glove jams to simulate a virtual balloon resisting finger motion. (E) The glove unjams to simulate the popping of a balloon, and the hand is again free to move. (F) The base support of the FJMs for the glove was given an angular offset to reduce the overall stiffness of the haptic glove in the unjammed state. (G) FJM is approximated as a cantilever beam with a point load equivalent to the maximum fingertip force to render. (H) Shear force diagram for FJM approximated as a cantilever beam for the haptic glove. AR, augmented reality.

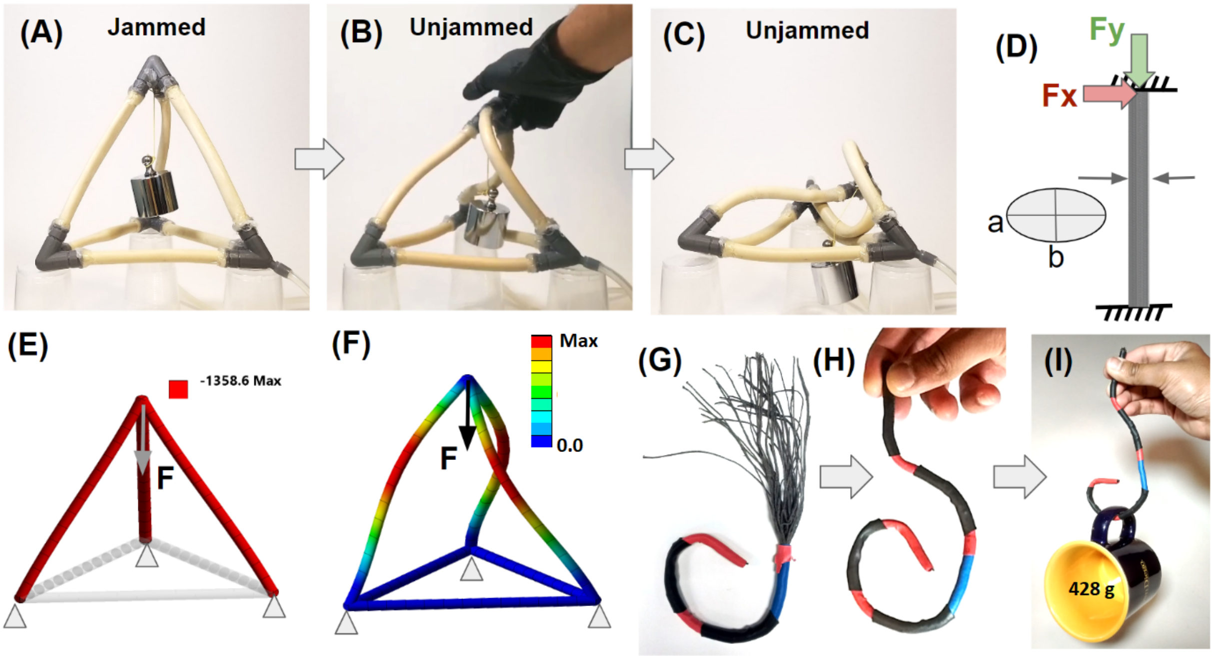

Figure 2.8: Demonstration of FJM in programmable and deployable structures. (A) In the jammed state, the deployable fiber jamming truss structure holds a weight of 500 g (external force) acting at the tip of the structure. (B) When unjammed, the FJMs acting as members begin buckling due to the external force acting at the tip of the structure. (C) The deployable structure completely collapses due to the external force. (D) The members in the deployable structure can be approximated as columns fixed at both ends with axial and transverse loads. (E) Plot for the ratio of axial loads to transverse loads acting on the inclined members of the tetrahedral truss structure (transverse/flexural load acting is negligible). (F) Plot for the total deformation for the third buckling mode of the tetrahedral truss structure (Ansys Academic Research Mechanical, Release 2019R1). Note the similarity to the experimentally observed buckling mode shape in (B). (G) Fibers are programmed and jammed into a hook-like shape using heat shrink tubing. (H) The jammed hook retains its shape due to pressure from the heat shrink tubing. (I) Demonstration of the load-carrying capacity for the FJM using thermal actuation for jamming.

Chapter 3

Dot-Matrix Inspired Fluidic Circuit for Independent Control of Large Arrays of Actuators

3.1 Introduction

Controlling a large array of independently addressable actuators has been a central issue in the field of haptic interfaces and soft robotics [47, 48, 49]. Integrating a high spatial density of actuators in textiles is of particular interest for the design of wearable devices for tactile and kinesthetic feedback [49]. Traditionally, actuators such as vibration motors, electromagnets, voice-coil actuators, piezoelectric actuators, and linear motors have been used to control these large arrays of individually addressable actuators[47]. However, these traditional actuation strategies have consisted of rigid materials integrated into fabric, resulting in devices that were uncomfortable to wear and also had limitations in conforming to the complex topographical surfaces on the human body. Recent investigations have turned to the use of soft robotic actuation strategies for wearable interfaces to overcome the challenges posed by traditional rigid actuator designs [47].

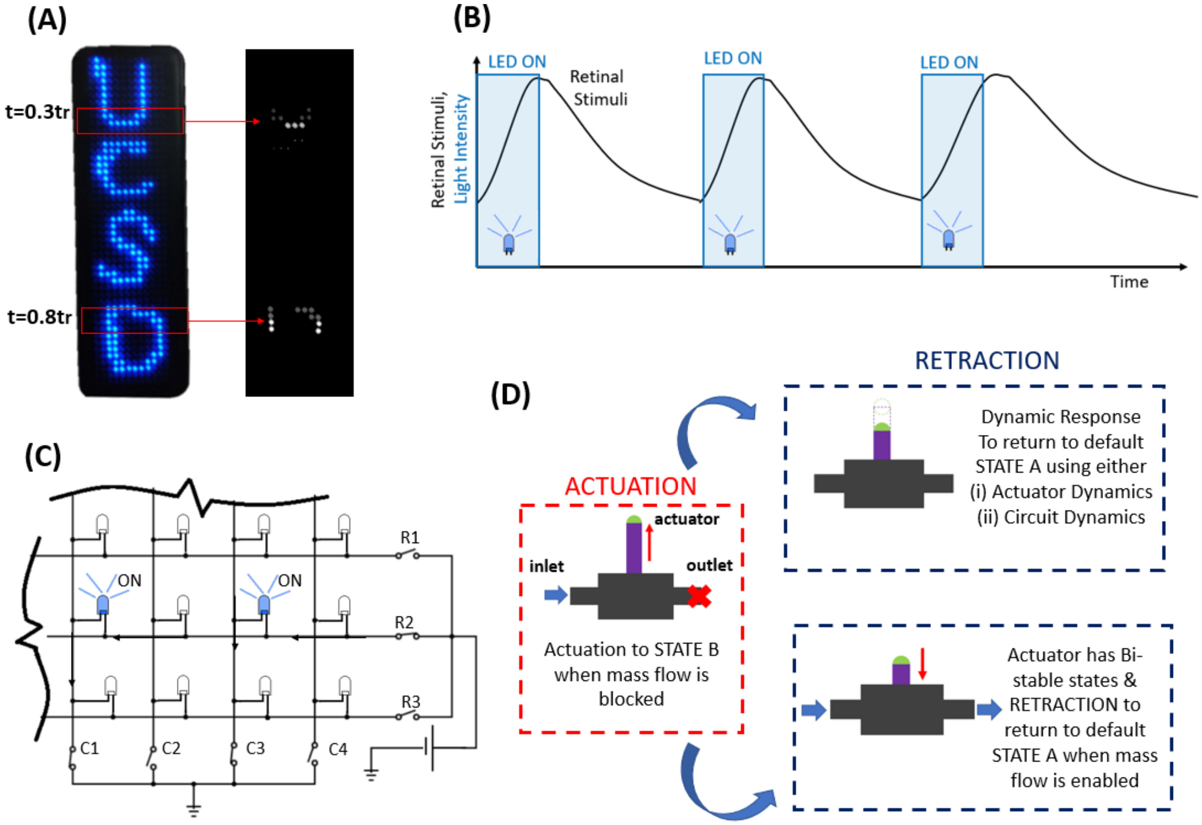

Figure 3.1: Abstracting the requirements of the fluidic circuit elements by studying the working principle of a dot-matrix display (A) A dot-matrix LED display displaying "UCSD". A photograph captured while the display was being refreshed shows a single row of LEDs illuminated. The image is displayed by cycling through a singer row of LEDs at a time. Since the refresh interval is within the visual persistence time or "Flicker fusion threshold", the viewer perceives a still image (B) The dynamics of Persistance of Vision (POV) display as reported in [50]. The LED flickers periodically as the image is refreshed on the dot-matrix display. Since the flickering of LED is within the flicker fusion threshold, the retina perceives the LED to be constantly on. (C) The corresponding row and column switch is closed to complete the circuit and allow the current to flow to turn the corresponding LED on. (D) The requirements for the fluidic actuator and circuit elements abstracted from a dot-matrix display.

Many recent studies have focused on using actuation strategies in soft robotics such as thermally responsive materials [51], dielectric elastomers [52], and eletrohydraulic actuators [53] for the design of high density individually addressable actuators. However, thermally responsive actuators (e.g., liquid crystal elastomers) have low actuation frequency which limits their use in applications requiring rapid response time like haptic devices [51]. Although Dielectric Elastomer Actuators (DEAs) and electrohydraulic actuators like HASELs can provide rapid actuation response, they require a high voltage for actuation which can be difficult to integrate into wearable devices due to safety concerns [53]. Fluidically actuated systems have been widely explored for the actuation of soft robots due to their lightweight, versatility, and ease of use [6, 54]. Pneumatics offers a promising solution for the design of high force-to-weight ratio actuators that can be integrated into wearable devices [47]. Using pneumatics enables the power source and the control system to be located offboard which facilitates the design of low-cost and lightweight actuators that can be integrated into textiles [49]. Additionally, the negligible viscosity of air enables the design of compact and narrow channels to control fluidic systems using high actuation frequencies [55].

Many interactive surface displays and interfaces use fluidic systems for the independent control of a large array of actuators. Harrison et al. demonstrated pneumatically actuated air pockets used as physical buttons that were overlaid on a visual display [56]. Follmer et al., demonstrated malleable shape-changing interfaces enabled by pneumatics to achieve phase transition that responds rapidly to vacuum using particle jamming [57]. Aegus hyposurface presented a wall-size visual display where each element of the display was connected to a pneumatically actuated piston [58]. Stanley et al., presented a deformable, jamming-based display that could control both stiffness and shape by tuning different sequences of vacuum and air pressure [59, 60]. Koehler et al., presented a similar design with particle jamming to achieve variable stiffness modulation of a 3D shape [61]. Although these variable stiffness displays rendered two different haptic modalities—shape and stiffness of the object, they required independent pneumatic control lines to individually address each modality which limits the scalability of such haptic displays. The number of actuators used in fluidically controlled shape displays presented in previous work was limited due to the number of individually addressable control lines available to actuate each element on these displays [60, 56, 58].

Scaling the pneumatic systems to enable them to individually address the pneumatic actuators is also of wide interest to enable high-density, wearable haptic devices. Previous work presented fluidically controlled wearable haptic devices to generate tactile and kinesthetic haptic feedback for interaction with virtual environments [62, 63, 64, 65]. The resolution and fidelity of these wearable haptic interfaces could be enhanced by increasing the spatial density of actuators used in these devices. However, in most cases, the spatial density of these actuators was limited by the pneumatic system used to control these devices. Most existing pneumatically actuated interfaces have used electro-mechanical valves or solenoid valves to individually address every actuator. Previous demonstrations for haptic vests normally used a set of electromechanical/ solenoid valves to address each pouch motor individually from the large array [65]. Addressing each pouch motor individually using a set of electromechanical valves is not scalable with the increase in the spatial density of pouches. Additionally, using miniature solenoid valves to miniaturize the system results in high fluidic resistance which affects the overall response time of these pouch motors. Delazio et al. attempted to address this challenge by using a high-pressure source to inflate the pouch motor and an additional vacuum pump to drain the pouch motors to improve the response time of the pouches.Because these valves are usually bulky and expensive, the scalability of the previous systems (to large numbers of actuators) has been limited.

There is little work addressing the scalability of pneumatic systems for the independent control of a large number of pneumatic actuators. Traditionally, most soft robotic systems have used fluidic control boards [66] for the pneumatic control of their soft robots. However, these control boards tend to be bulky and not scalable with an increase in the number of outputs. Many recent studies have focused on making the fluidic control systems for soft robots modular and easily accessible to a wide range of audiences [67]. Systems such as Pneudino, Lego pneumatics, haptic pneumatic toolkit, and FlowIO platform provide modular hardware platforms that can be used to control the pressure and airflow for pneumatically actuated soft robots [49, 67]. Robertson et al. presented a vacuum-actuated reconfigurable surface that was compact and easily scalable

[68]. The scalability was achieved using a modular design of the actuator element by packaging each module as an actuator connected to the solenoid valve [68]. Although considerable attention has been given to making the pneumatic control systems more modular, rather less attention has been paid to the design of autonomous pneumatic circuits to reduce the number of valves required to individually address each actuator. Bartlett et al., addressed this issue using a pneumatic demultiplexer inspired from previous demultiplexer designs in microfluidics and electronic circuits [5]. Although pneumatic demultiplexing addresses the challenge of using a limited number of solenoid valves (N) to independently control a large array of actuators (2^{N-1}), it has one major limitation—only one actuator can be addressed at any given time. Hence, a large array of actuators would take a significant amount of time to refresh using a pneumatic demultiplexer as the multiplexer cycled through one actuator at a time to refresh the entire display. Recent work in the development of pneumatic equivalent of electrical circuits like relays and oscillators has a considerable potential to minimize the number of electromechanical valves used in the system [4, 3, 2, 69]. However, these pneumatic circuit components can only be used to control the actuators in a pre-programmed pattern and cannot be used to address each actuator independently as desired in haptic interfaces and interactive media.

In this chapter, we present a fluidic circuit, inspired by the dot-matrix circuit found in LED displays, for the independent control of a large array of pneumatic actuators with a rapid refresh rate. Additionally, we demonstrate the application of this fluidic circuit for the actuation of a 2D-Shape Display, a wearable tactile vest, and an array of soft actuators. We also validate the design of the fluidic system for the control of soft actuators using an analytical model. We make the following contributions within soft robotics with a specific application in scalable pneumatic circuits for controlling a large array of fluidic actuators: (A) Our work for the first time presents a fluidic circuit inspired by an electrical circuit of a dot-matrix display to enable lower refresh intervals along with independent control of a large array of fluidic actuators. (B) Lumped parameter system modeling to predict the dynamic response of the pneumatic actuators—We present rigorous modeling and analysis for the fluidic system using equivalent electrical circuits, which enables us to predict the dynamic response of the system and choose the critical design parameters for various components in the fluidic circuit.

3.2 Background

Previous work has looked into electronic circuits for inspiration to design scalable fluidic circuits. Preston et al. demonstrated a soft bistable valve to control the flow in an output line based on the pressure in an input line, which is conceptually similar to how an electrical relay works [3, 2]. Preston et al. further demonstrated the application of this soft bistable valve to construct oscillator circuits (similar to electrical oscillators) which can completely eliminate the need for using electromechanical valves to control a periodic sequence of actuation [2, 3]. Drotman et al., demonstrated using the soft ring oscillator to control an electronics-free quadrupedal robot with mechanical sensing to completely eliminate the need for using electrical valves or sensors [4]. However, these electronics-free circuits reported in previous work can only execute a pre-programmed sequence and cannot individually address the actuators as desired in the case of haptic interfaces and interactive media. Another inspiration for designing pneumatic circuits for independent control of actuators are demultiplexers used to control Persistance of Vision (POV) based 7-segment displays. These demultiplexers periodically cycle through each of the 7 LED segments to display a digit on the 7-segment display. The digit is perceived as a constant image by the observer since the refresh interval to address each LED is under the visual persistence time of the human eye. Bartlett et al., took inspiration from this concept to design a fluidic demultiplexer to control a large array of soft actuators [5]. However, similar to the electrical multiplexer, only one actuator could be addressed at a time using the fluidic multiplexer. Findings reported by Bartlett et al., suggest that the dynamics of the fluidic system did not allow cycling through all the actuators at a high frequency. Thus, it was not possible to perform an operation that required multiple outputs to be pressurized simultaneously [5]. This drawback limited the application of the demultiplexer to specific use cases in soft robotics as it did not result in a fluidic system that could be scaled to control a large number of outputs simultaneously.

In this work, we considered an alternative inspiration for the design of fluidic circuits—dot-matrix display circuits (see Figure 3.1[A]). Dot-Matrix displays consist of Light Emitting Diodes (LEDs) that are arranged in a matrix. All cathodes of the LEDs are connected together along each row in a matrix and all the anodes of the LEDs are connected together along each column in the matrix (Figure 3.1[B]). To turn on a particular LED, the corresponding row and column in the LED matrix are connected to the voltage source. An LED can be treated as an equivalent to a resistor in series with a p-n junction diode. Rapidly cycling through a single row of LEDs with a refresh interval higher than the visual persistence time of the human eye causes the observer to perceive a still image on the display Figure 3.1[B]. A fluidic actuator is conceptually equivalent to an electrical capacitor with a single input line controlling the pressurization and depressurization of an actuator chamber. However, to construct a fluidic circuit similar to the dot-matrix display we needed an intermediate circuit element that was conceptually similar to a resistor with a p-n junction diode. As a result, we determined the following design requirements for the actuator and the intermediate circuit element from the insight obtained by studying the operation of a dot-matrix display:

3.3 Results and Discussion

3.3.1 Design Requirements

Requirements for the actuator— The LED dot-matrix display cycles rapidly by addressing a single row of LEDs at any given time and relies on the persistence of vision (visual inertia) of the observer to perceive a constant image. Since the electrical signals travel close to the speed of light, it is possible to achieve very high refresh rates (>100 Hz) using a LED dot-matrix display. However, based on previous studies, the dynamics of fluidic systems are not capable of achieving refresh rates over the kinesthetic dynamic threshold of the human body (20-30 Hz)[47]. Hence, the design of the fluidic circuit should be such that either the actuator holds its state (actuated or retracted) throughout the refresh interval, or the dynamics of the circuit allow the actuator to slowly return to its default state (see Figure 3.1[D]).

Requirements for the intermediate circuit element— Similar to the way a resistor generates heat or light energy when current is allowed to flow through the resistor, the intermediate circuit element should perform either actuation when the mass flow through the circuit element is enabled, and should perform retraction when the mass flow through the circuit element is disabled (see Figure 3.1[D]).

Vacuum ejector devices as primary circuit elements— We analyzed and iteratively prototyped various designs that satisfy the requirements of the intermediate circuit element listed in the prior section of this work. Based on the requirements, a circuit element that can generate both pressure and vacuum would be ideal for switching the state of an actuator that can hold its state in the absence of any input signal (e.g. flip-flop actuator like a bistable membrane). Literature shows that the design based on vacuum ejector devices is most suitable to generate vacuum by using pressurized air as input [70]. Additionally, vacuum ejectors are easy to fabricate and robust due to the absence of any moving parts. Hence, we chose vacuum ejectors as the circuit element for the matrix [70].

The design and analysis of vacuum ejectors are well understood as reported in the literature[70, 71, 72, 73]. A single-stage vacuum ejector consists of three main sections—a primary nozzle, a mixing section, and a diffuser (Figure 3.2[A, B]). When a pressure source is connected at the inlet of the vacuum ejector, the primary nozzle accelerates the airflow according to Bernoulli's equation (Figure 3.2[C]). This high velocity, low static pressure air flow exiting the primary nozzle induces a secondary flow from the suction chamber and accelerates it along with the mixing chamber (Figure 3.2[C, D]). The diffuser at the exit lifts the static pressure of the mixed flow to be close to atmospheric pressure. The literature shows that the diameter of throat (D_t/D_m), the position of primary nozzle exit to the entrance of the mixing chamber (L_{pm}/D_m), and the angle of the diffuser section (β) most significantly affect the vacuum generated by the Venturi pump (Figure 3.2[A,B]) [70].

Building on the literature, we conducted empirical tests to determine the ideal design parameters of a Venture tube vacuum generator for our dot matrix display inspired fluidic circuit. The narrowest constriction in a fluidic system has the largest impact on its overall resistance [74]. Hence, for a Venturi pump, the diameter of the throat (D_t) significantly affects the resistance of the fluidic system as the throat is the smallest constriction to mass flow (Figure 3.2[C]). Hence the throat diameter is the most critical design parameter for the design of the vacuum generators as circuit elements. Although a considerable amount of effort has been devoted to the optimization of Venturi pumps for maximizing the vacuum generated in the suction chamber, rather less attention has been paid to the effect of changing the design parameters on the fluidic resistance of the vacuum generator. Hence we experimentally tested the effects of the change in the diameter at the exit of the primary nozzle on the overall fluidic resistance of the vacuum generator (Figure 3.2[G-I]). Since the dot-matrix-inspired fluidic circuit involves system design and integration, the optimum Venturi pump design as a stand-alone component does not necessarily reflect as an optimum design when Venturi pump as it is integrated into a system. Hence, we considered the tradeoffs between the fluidic resistance of the Venturi pump and the maximum vacuum generated by the Venturi pump and selected the vacuum generator with 1.39 mm diameter at the exit of the primary nozzle as the optimum design for our use case.

Similar to a dot-matrix-based LED display, the Venturi pumps were all arranged (in a matrix) with the inlets to the Venturi pumps connected in a row and outlets of the Venturi pumps connected together in a column. Since the dot-matrix-based fluidic circuit was addressed one row at a time, we explain the working principle of using a single row of Venturi pumps to control an array of actuators (syringes in this case) in Figure 3.3[A-C].

3.3.2 Integrated fluidic circuit to control a 5×5 2D-Shape Display

We demonstrated that an array of actuators (syringes) can be controlled by switching the output of the vacuum ejectors connected in parallel to a single row (Figure 3.3[A-C]). The refresh interval of the 2D-shape display depended on the sum of the minimum refresh interval required by each row to update the states of each of the flip-flop actuators (syringes). Rapidly cycling through multiple rows of Venturi pumps enabled the control of a 2D shape display as shown in 3.4, 3.5. Figure 3.4 [A]-[C] shows the stages during the assembly of a 5×5 dot-matrix-inspired fluidic circuit. The circuit was wall-mounted (Figure 3.4 [A]-[C]) with the inputs to the row channels and output from the column channels connected to electromechanical valves controlled using a micro-controller (Figure 3.4(E)). A 5×5 2D-Shape display (Figure3.5) was controlled by rapidly cycling through each row of the matrix and updating the states of the corresponding actuators (Figure 3.4, 3.4).

Modeling the fluidic circuit to optimize the refresh rate of the 2D-Shape Display The refresh interval for each row in the circuit as we cycle through the matrix should be sufficient to actuate or retract the syringes to their desired state. We modeled the row of Venturi pumps connected to a common input channel as an equivalent resistor-capacitor (RC) circuit that we used to calculate the pressure response and estimate the minimum refresh interval desired to update the state of the actuators. The fluidic resistance of the electromechanical valves (R_{sys}), Venturi pumps (R_v), and the leak through the system (R_{leak}) were empirically calculated by measuring the time constant of the R-C circuit where the Resistance (R) was the unknown value as shown in Figure 3.2[E, F]. The resistance of the tubing (R_{tubing}) that connected the Venturi pumps to the syringes was modeled using the Darcy-Weisbach Equation 3.1.

$$R_{tube} = \frac{\Delta P}{\dot{m}} = \frac{128\mu L}{\pi \rho D^4} \tag{3.1}$$

The output channels where flow through the channels is blocked are modeled as capacitors with an equivalent pneumatic capacitance of $N_{closed}C_{col}$. The output channels where flow through the channels is enabled can generate a vacuum at the throat section to retract the corresponding syringes back to the default position. These open channels are modeled as resistance in parallel R_v/N_{open} to the pressure source as shown in Figure 3.4[D]. The pneumatic capacitance of the columns (C_{col}) and syringes (C_{syr}) is proportional to their internal volume and calculated using Equation 3.2 (assuming isothermal compression, $T_{atm} = 298K$, $R = 287J/KgK$)

$$C_{res} = \frac{dm}{dP} = \frac{V_0 \mathrm{M}}{\mathrm{R}T} \tag{3.2}$$

When the flow through the output channel is blocked, the pressure response of C_{syr} actuates the corresponding syringes. This pressure response can be used to model the dynamic response of the plunger in the syringe Figure 3.4[D]. The circuit shown in Figure 3.4[D] is a second-order system, with the transfer function for the pressure response at C_{syr} derived using Kirchoff's law as given below: 3.3:

$$P_{syringe}(s) = R_{parallel}P_{pump}/(P + Qs + Rs^2) \tag{3.3}$$

where,

$$P = R_{syr} + N_{closed}R_{parallel} \tag{3.4}$$

$$\begin{multline} Q = N_{closed}(C_{col} * R_{syr}R_{parallel} + C_{col}R_{syr}R_{series} + C_{syr}R_{syr}R_{parallel} + \\ C_{col}R_{parallel}R_{series} + C_{syr}R_{syr}R_{series} + C_{syr}R_{syr}R_{tubing} + C_{syr}R_{parallel}R_{series} + \\ C_{syr}R_{parallel}R_{tubing}) \end{multline} \tag{3.5}$$

$$R = N_{closed}^2(C_{col}C_{syr}R_{syr}R_{parallel}R_{tubing} + C_{col}C_{syr}R_{syr}R_{series}R_{tubing} + C_{col}C_{syr}R_{parallel}R_{series}R_{tubing}) \quad (3.6)$$

$$R_{parallel} = (R_{leak}R_v)/(N_{open}R_{leak} + R_v) \quad (3.7)$$

$$R_{series} = (R_v)/(N_{closed}) \quad (3.8)$$

The response of the syringes can be calculated by modeling the pressure response of the fluidic circuit. The fluidic circuit is shown in Figure 3.4(D) is a second order system. However, the resistance of the tubing (R_{tubing}) that connects from the Venturi pump to the syringe is negligible as compared to the other resistance values within the circuit. Hence, (R_{tubing}) can be neglected and the circuit can be simplified to a first-order system to be solved using Thevenin's theorem. Once the pressure response in the syringe is known, the dynamic response of the syringe to travel its full stroke length can be calculated using the equations of motion. The acceleration of the syringe during actuation can be calculated using the following formula:

$$a = (P_{syr}(t)A_{syr} - M_{plunger}g - F_{friction})/M_{plunger} \quad (3.9)$$

A similar approach is used to calculate the time required to retract the syringe back to its default state. Figure 3.4[D] shows the circuit for retraction of the syringe. The value of P_{vac} is the vacuum generated by the Venturi pump for the given input pressure. We assumed the minimum refresh interval for the row to be the great of: 1) the time required to actuate, or 2) the time required to retract, the syringe to its desired state. Based on the circuit parameters we estimated empirically, we calculated the refresh interval for each row as a function N_{open} and N_{closed} (For a 5×5 circuit, N_{open} and N_{closed} = 5; see Table 3.1). Our experimental evaluation showed that the friction between the plunger and the syringe varied greatly due to the viscoelastic behaviour of the plunger material. Hence, we used a refresh interval of 7.5 seconds (1.5 seconds for each row X 5) in all our demonstrations for the shape display.

$$R_{Sys} = 3.327X10^7(Pa - s/Kg)$$

$$R_v = 12.979X10^7(Pa - s/Kg)$$

$$R_{leak} = 10.393X10^7(Pa - s/Kg)$$

$$R_{tubing} = 8.575X10^6(Pa - s/Kg)$$

$$C_{Col} = 1.209X10^-9(Kg/Pa)$$

$$C_{Syr} = 9.2525X10^-11(Kg/Pa)$$

Table 3.1: Actuation time for updating the states of syringes as a function of the number of output valves in open/ closed state

N_{open}	N_{closed}	$t_{actuation}(s)$	$t_{retraction}(s)$	$t_{max}(s)$
0	5	0.1	0	0.1
1	4	0.14	0.04	0.14
2	3	0.145	0.045	0.145
3	2	0.145	0.055	0.145
4	1	0.145	0.065	0.145
5	0	0	0.09	0.09

Manipulating and Object using the Topography generated by the 2D-Shape Display

We demonstrate manipulation of a spherical object using the height profiles generated by our shape display in Figure 3.6. The static height profiles produced by the shape display guide the ball in the desired direction. Dynamic modification of the height profiles helps us to manipulate the object as shown in Figure 3.6.

3.4 Demonstration 2: Integrated fluidic circuit to control a pneumatically actuated haptic vest

In this section, we present a haptic vest consisting of pneumatically inflatable airbags that provide force feedback to the user when the bag is inflated (Figure 3.7[A]).Previous work has demonstrated haptic vest designs with inflatable airbags (pouch motors) with individually addressable electromechanical valves that control the inflation of pouches [65]. We present an interface where the user can click a button to actuate the corresponding pouch on the vest and experience the sensation of being hit by a soft object (e.g. snowball). We select the design parameters and actuation time for the vest based on previous work [65]. When the user selects a pouch from the interface, the fluidic control board activates the valve controlling the corresponding row and column to which the pouch is connected. We inflate the pouch to a target pressure of 15 psi. The pouch is then rapidly deflated to give a sensation of being hit by a soft object. The deflation of the pouch is accelerated by enabling flow through the Venturi pump connected to the pouch which generates a vacuum in the airbag. We calculated the response time of the pouches by using the equivalent circuit shown in Figure 3.7 [F] and formulas presented in section 1.41 of this chapter. We estimate the time taken to inflate the pouch motor to 15 psi to be 0.35 sec for 35 psi input pressure and no leakages. We compared the pressure response of the pouch motor with our analytical model based on the R-C circuit presented in 3.7 [F] for both with and without vacuum cases.

3.5 Demonstration 3: Dynamic control for an array of soft actuators

Although Demonstration 1 presented the control of a 5 × 5 shape display using our multiplexed fluidic circuit, the actuators used in the shape display were flip-flop devices that could hold their state. However, most soft robots consist of elastomeric actuators, that return to their default state in the absence of any actuation pressure. This property of elastomeric devices makes the control of soft robots using demultiplexing devices challenging since the soft actuators tend to return back to their default state as the circuit cycles through the array of actuators. We present an approach to introduce a modification in the circuit to dynamically control such soft devices using a separate channel during deflation of the actuator. The inflation of these soft actuators was similar to the inflation of the syringes as described in the section 3.3.2. However, during deflation, the actuator drained through a tuned fluidic resistance instead of the Venturi pump. Tuning this fluidic resistance enabled us to introduce a delay in the response of elastomeric actuators during deflation. This delay in the response time during deflation enabled us to control the pressure in the soft actuators between P_{min} and P_{max} throughout the refresh interval.

3.5.1 Modeling the fluidic circuit to tune $R_{orifice}$

The pressure in the actuator during the inflated state is desired to be within a chosen range (P_{min}, P_{min}). We chose a range of (2.5 psi, 15 psi) based on the non-linear pressure response of our soft actuators (Figure 3.9 (D)). The first order circuit during inflation of soft actuator (Figure 3.9(A)) can be modeled as an equivalent R-C circuit using Thevenin's theorem (Figure 3.9 (C)). The equivalent resistance and capacitance of the R-C circuit during inflation (Figure 3.9 (A)) can be derived using Thevenin's theorem.

$$R_{Th} = R_{orifice}||(R_{Th}/N_{closed} + (R_v/N_{open}||R_{sys})) \tag{3.10}$$

$$C_{Th} = C_{col} + C_{act} \tag{3.11}$$

Hence, the time response for the R-C circuit for inflation (Figure 3.9 (C)) is given by:

$$t_{inflation} = R_{TH} * C_{TH} * ln(P_{max}/P_{pump}) \tag{3.12}$$

Hence, the time response for the R-C circuit during deflation (Figure 3.9 (B)) is given by:

$$t_{deflation} = R_{orifice} * C_{act} * ln(P_{min}/P_{max}) \tag{3.13}$$

Since the dot-matrix inspired fluidic circuit presented in this paper had 5 rows, $1/5^{th}$ of the total refresh interval was devoted to each inflation cycle, and the soft actuators deflated during the other $4/5^{th}$ of the total refresh interval. As a generalization,

$$t_{deflation} = (N_{rows} - 1) * t_{inflation} \tag{3.14}$$

Hence,

$$R_{orifice} * C_{act} * ln(P_{min}/P_{max}) = (N_{rows} - 1) * R_{TH} * C_{TH} * ln(P_{max}/P_{pump}) \tag{3.15}$$

We used the above equation to calculate the equivalent fluidic resistance required ($R_{orifice}$) to maintain the pressure in the actuator between the desired pressure range during the inflated state. Once $R_{orifice}$ was known, we were able to calculate the diameter of the orifice required to generate an equivalent fluidic resistance by using the following formula [74]:

$$R_{orifice} = 307/d^2_{orifice} \tag{3.16}$$

For the parameters in our circuit and by experimentally calculating the leakage in our system, we calculated the $R_{orifice}$ to maintain a pressure range between (2.5 psi, 15 psi). We experimentally simulated the pressure response for a single row of soft actuators with two actuators being inflated and compared the pressure response with our analytical prediction (see Figure 3.9[E]).

Chapter 3, or portion thereof, is being prepared for the publication of the material. Jadhav, Saurabh; Glick, Paul; Ishida, Michael; Zhang, Ziyang; Chan, Christian; Adibnazari, Iman;

Schulze, Jurgen P.; Tolley, Michael T. The dissertation author was the primary investigator and author of this paper.

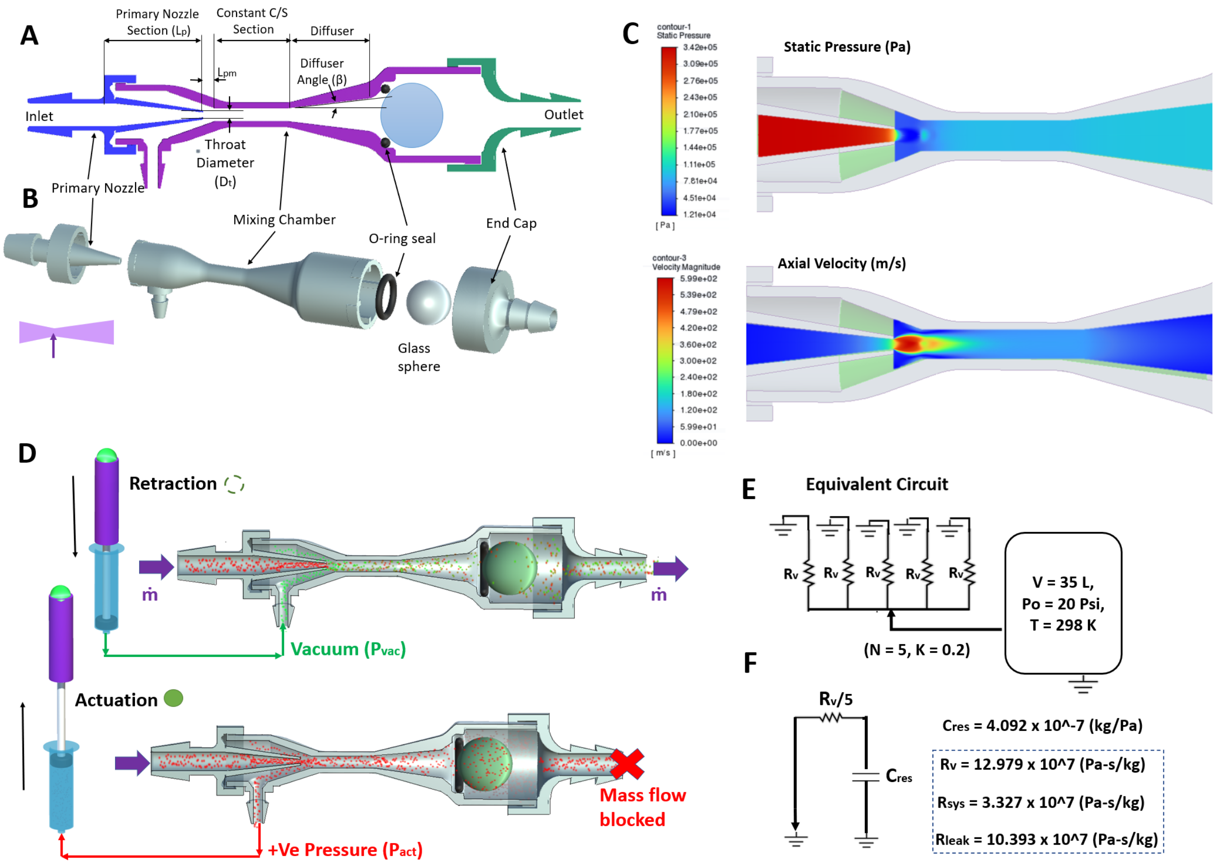

Figure 3.2: Design and analysis of Vacuum Ejector Device. (A) and (B) Construction and assembly of vacuum generator device. The assembly of vacuum generators consists of three parts: a primary nozzle, a mixing chamber, and an end cap. The critical design parameters of the vacuum generator to generate a vacuum in the suction chamber are the primary nozzle throat diameter, the length of the primary nozzle, and the angle of the diffuser section. A glass marble with an O-ring on the seat acts as a one-way valve. (C) CFD analysis of the vacuum generator showing the pressure and axial velocity contours in the vacuum generator. The flow through the primary nozzle is under-expanded and the axial velocity reaches a Mach no. of 1.7 at the exit of the nozzle. (D) Working principle: When air flows through the nozzle generating a vacuum in the suction chamber, the plunger is retracted. When the mass flow through the nozzle is blocked, the air escapes through the suction chamber and actuates the plunger. (E) & (F) The fluidic resistance of the vacuum ejectors is measured by filling a chamber with a known value of fluidic capacitance with air, and letting the air in the chamber drain to find the time constant of the circuit. We filled up the chamber with air up to a pressure of 20 psi, and drained the air until it had a pressure of 10 psi, to measure the time constant. We drained the chamber using a combination of vacuum generators (between 1 to 5) in parallel.

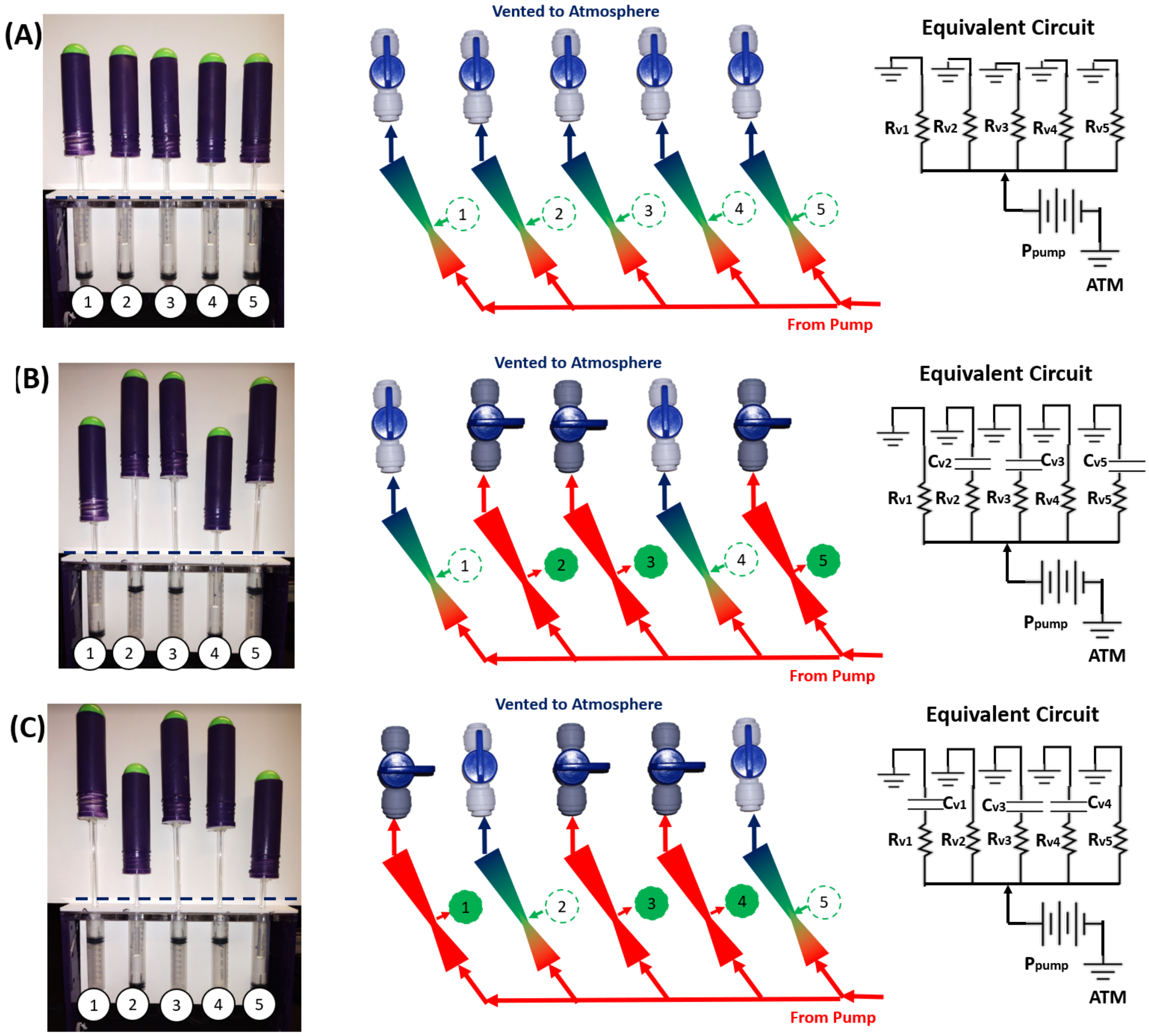

Figure 3.3: Working principle of the fluidic circuit using a single row of vacuum generators. All the vacuum generators are connected in parallel to a common pressure source. (A) The outlet of all vacuum generators is open, thus enabling airflow through the Venturi pumps. This generates a vacuum at the throat for all five Venturi pumps and keeps the plungers retracted to their defaults states. (B) Outlets to vacuum generators 2,3, and 5 are closed, thus blocking the mass flow through these 2,3, and 5 Venturi pumps. The pressure in the Venturi pumps 2,3, and 5 rises up to the downstream pressure, thus causing the plungers 2,3, and 5 to actuate. (C) Outlets to 2 and 5 are opened thus enabling mass flow through these Venturi pumps and generating vacuum at the throat. This retracts the plunger 2 and 5. Outlets to vacuum generators 1 and 5 are closed, thus blocking the mass flow through Venturi pumps 1 and 5, and generating positive pressure to actuate the corresponding plungers. Since outlet to vacuum generator 3 remains closed, plunger 3 retains an actuated state.

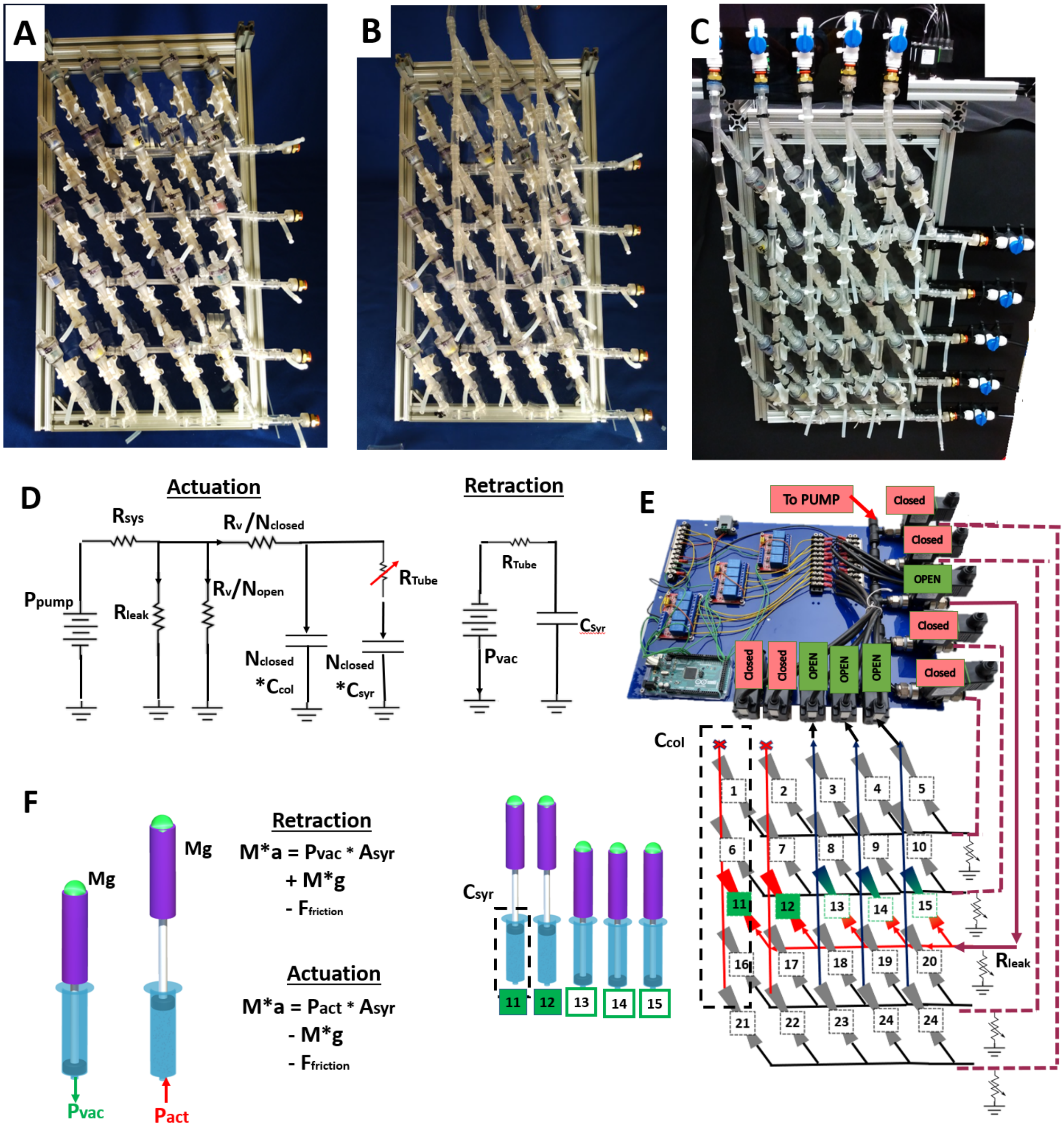

Figure 3.4: Dot-matrix-inspired fluidic circuit to control a 5 × 5 2D-Shape Display. (A)-(C) Images of time-lapse during assembly for the fluidic circuit. (D) Equivalent circuit of a single row of the fluidic circuit controlling the corresponding actuators on the 2D shape display. (E) The 5 × 5 dot-matrix-inspired fluidic circuit is controlled using 10 electro-mechanical valves. Air supply to the row $(11 - 15)$ is enabled to control the plungers in the corresponding row. Outlets to vacuum generators 11 and 12 are closed thus generating pressure in the Venturi pump and actuating the corresponding plungers. Outlets to 13, 14, and 15 are opened thus generating vacuum and retracting the corresponding plungers. (F) The dynamics of the plunger can be calculated using force balance, and equations of motion.

Snapshots while cycling through each row to display ‘U’ followed by ‘C’

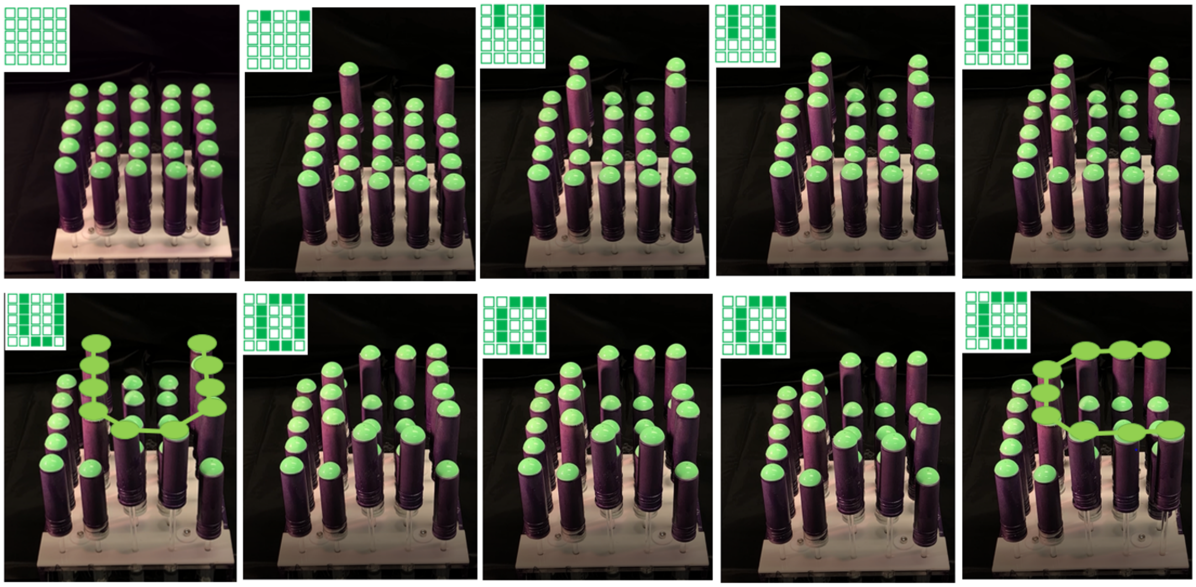

Snapshots of each frame while displaying numbers ‘0’ to ‘9’

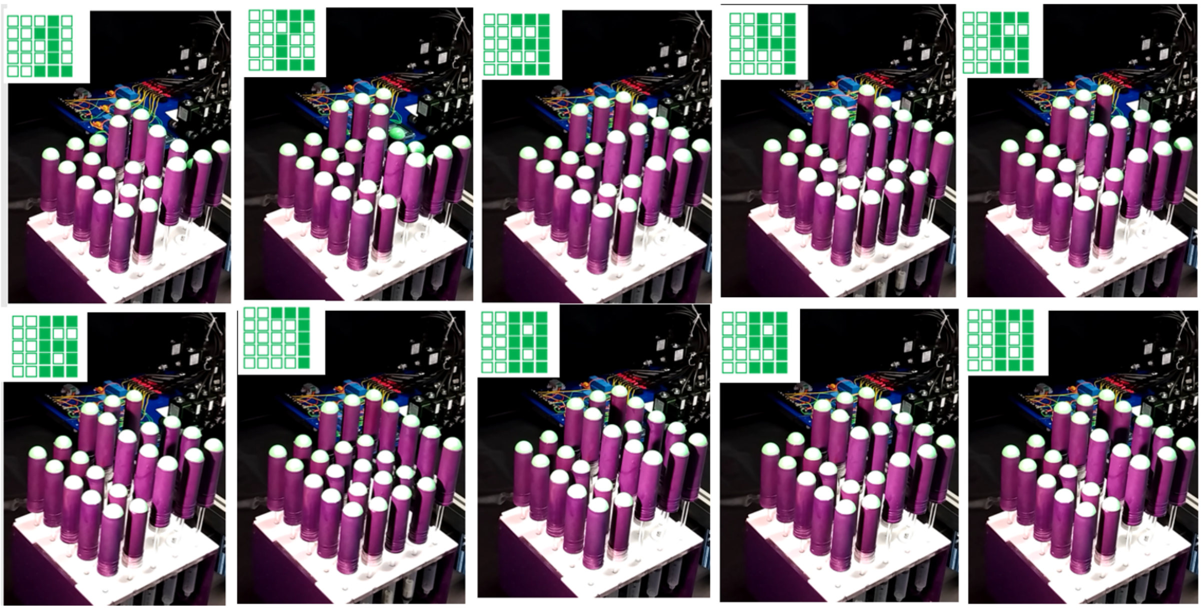

Figure 3.5: Time lapse of 2D-Shape Display rendering alphabets and numbers. (TOP) Rendering on the shape display as each row on the shape display is updated to display ‘U’ followed by ‘C’ (BOTTOM) Rendering on the shape display as each frame is updated to display numbers ‘0’ to ‘9’.

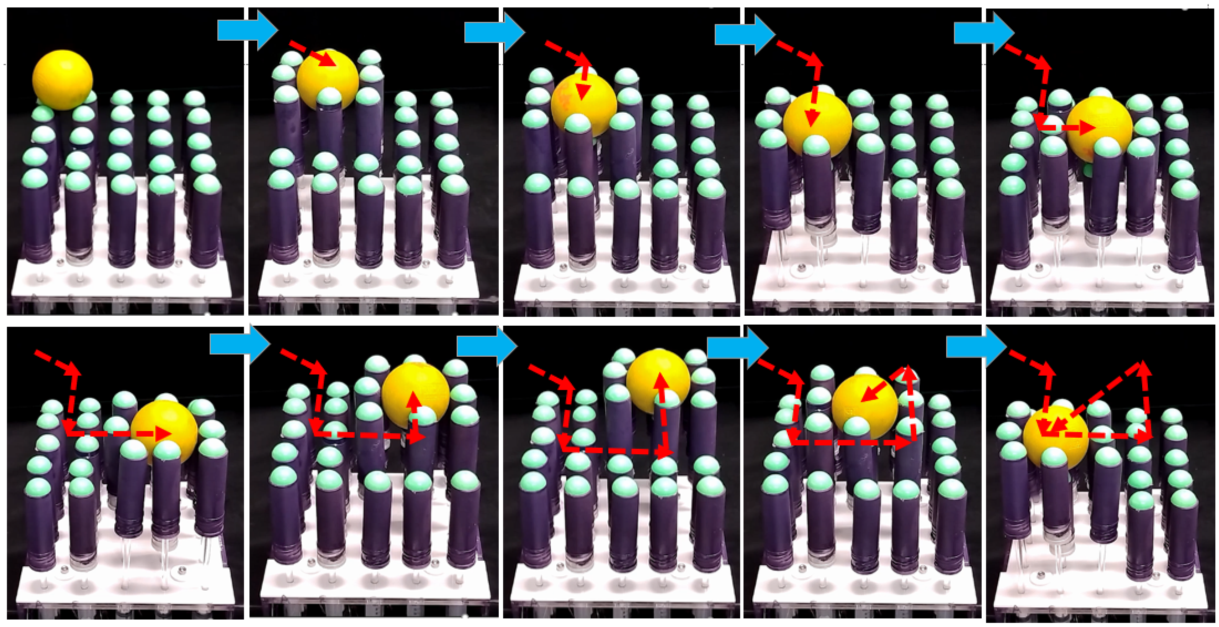

Figure 3.6: Time lapse of 2D-Shape display controlling and manipulating a spherical object. The ball is first constrained between the taxels of the shape display and manipulated in the desired direction.

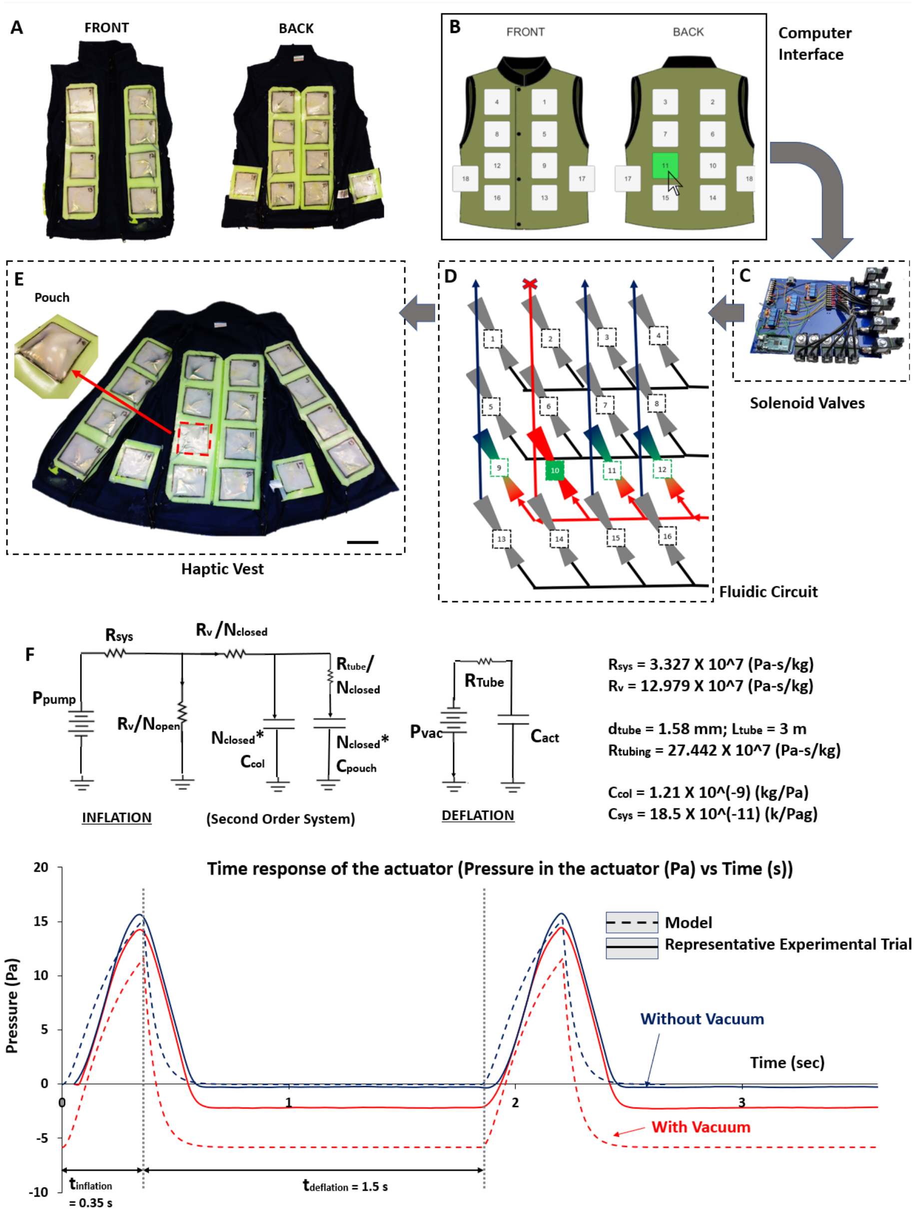

Figure 3.7: Dot-matrix-inspired fluidic circuit to control a pneumatically actuated haptic vest. (A) The front and back of the haptic vest turned inside-out to display the pouches on the vest. The haptic vest has 18 pouches (6 cm × 6 cm) connected to the fluidic circuit. (B) An interface is used to actuate the pouch to a pressure of 15 psi. When a particular pouch is clicked, the interface communicates with the fluidic control board (C) which activates the electro-mechanical valves controlling the row and column connected to the corresponding pouch. Thus, positive pressure generated in the corresponding Venturi pump inflates the pouch (E). (F) Equivalent circuit for inflation and deflation of pouches in the haptic vest. Note that the tubing resistance between the Venturi pump and the pouch is higher as compared to the other resistances in the system. Hence, the tubing resistance cannot be neglected. Pressure response of the pouch for actuation time of 0.35 sec and periodic actuation with a time period of 1.85 sec.

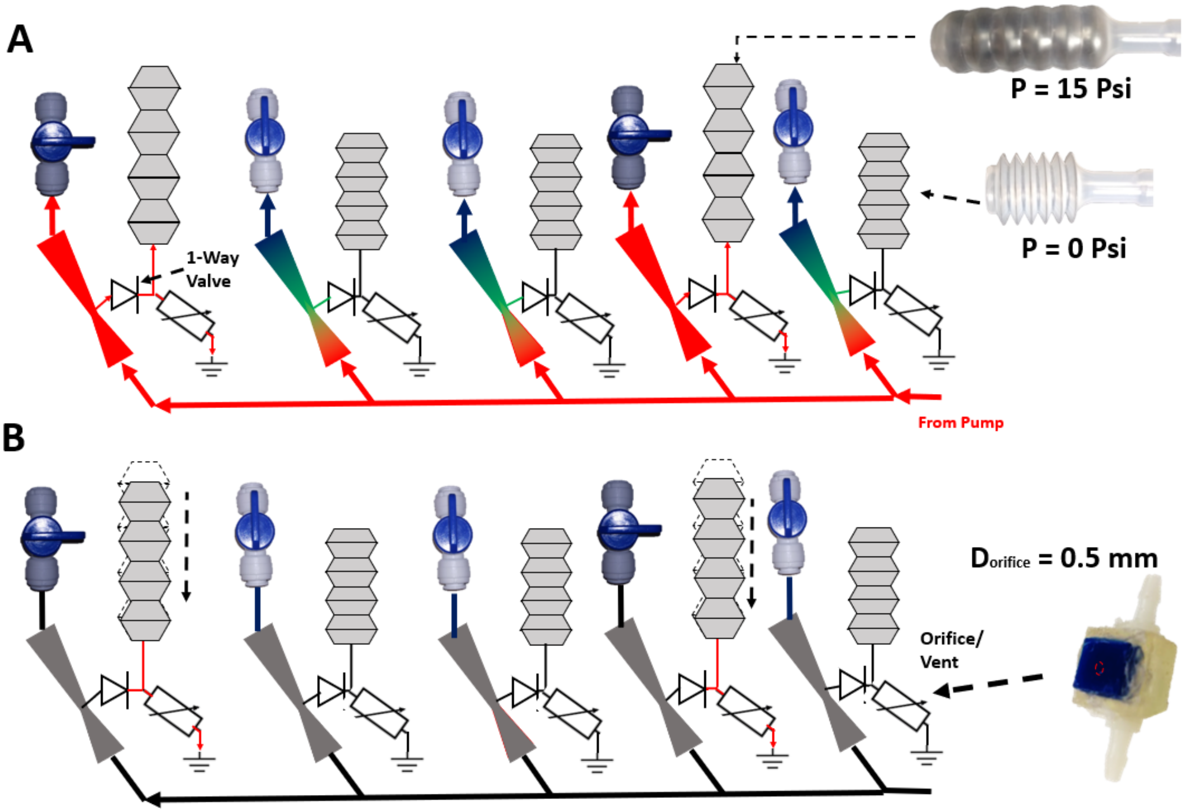

Figure 3.8: Demonstration for a single row of the fluidic circuit controlling an array of soft actuators. (A) During the actuation cycle, the outlets to Venturi pumps corresponding to the actuators to be inflated were closed. The airflow inflated actuators 1 and 4, while some air escaped through the orifice. (B) In the unactuated (no pressure) state, the inflated actuators slowly drained to the predefined minimum pressure until the circuit cycled back to inflate the desired actuators.

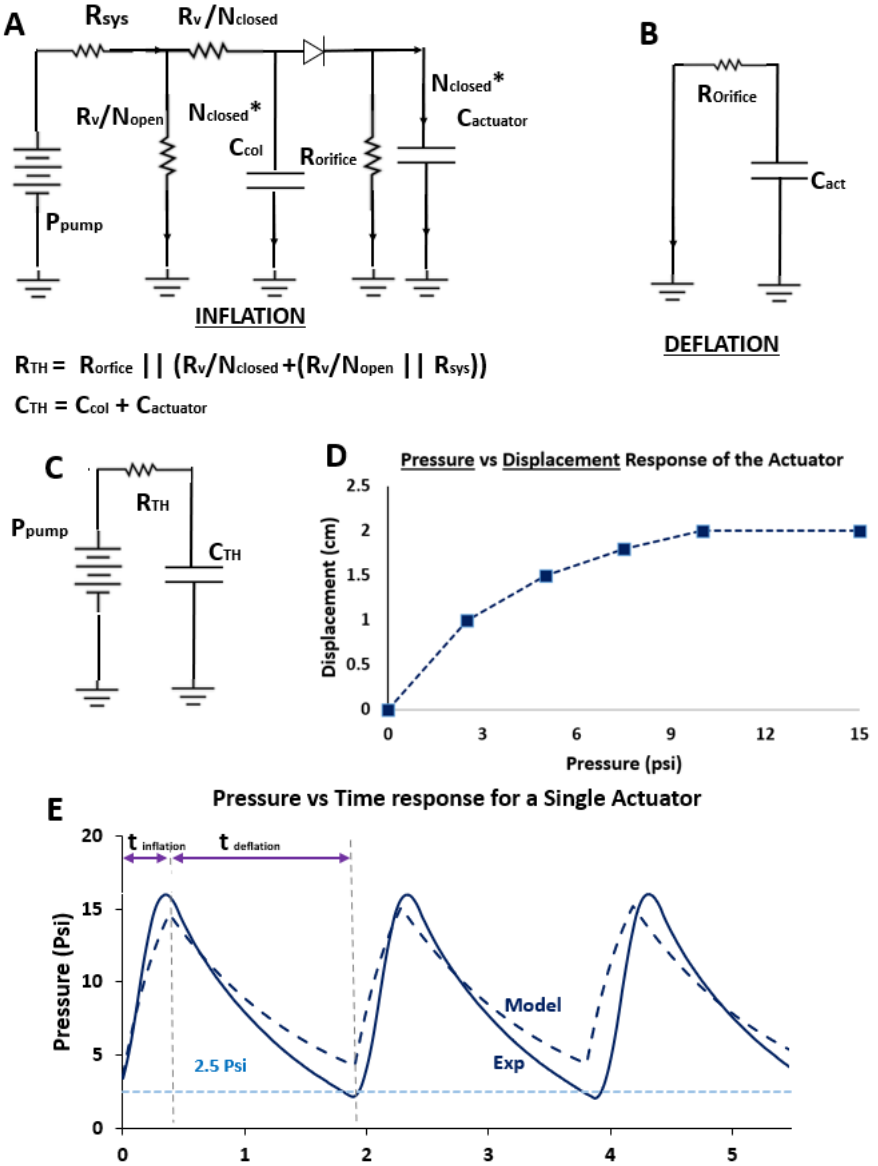

Figure 3.9: Modeling the fluidic circuit used to control the soft actuators. (A) & (B) Equivalent circuit during inflation and deflation of the corresponding soft actuators. (C) During inflation, the circuit is a first-order system and can be simplified to an equivalent RC circuit using Thevenin's theorem. (D) The non-linear response of the soft actuator was used to set the range of desired pressure in the soft actuator. In our case, we kept the pressure in the soft actuator within 2.5 to 15 Psi in the inflated state. (E) The time response of the soft actuator overlapped with the analytical model based on our equivalent circuit.

Chapter 4

SpaceFrameVR: A 3D-User Interface for design, analysis, and optimization of the space frame

4.1 Introduction

Computer-Aided Design (CAD) has become a ubiquitous part of the product development process with a wide range of applications including three-dimensional (3-D) design, visualization, simulation, and digital prototyping [75, 76]. The inherent qualities of Computer-Aided Design tools, including easy modifications and revisions to the designs [77], ease of collaboration[78], and advanced analysis capabilities like Finite Element Analysis (FEM), have increased the overall efficiency of the product development process by reducing the errors and the increased product quality [75, 79, 76]. Nevertheless, many product design activities still involve building multiple physical mockups to evaluate the merit of the digital design and to identify any weak points in the design. Full-scale mockups give designers a way to visualize and perceive their design concept at its true scale and interact with the design in an intuitive way to identify any feasibility issues.

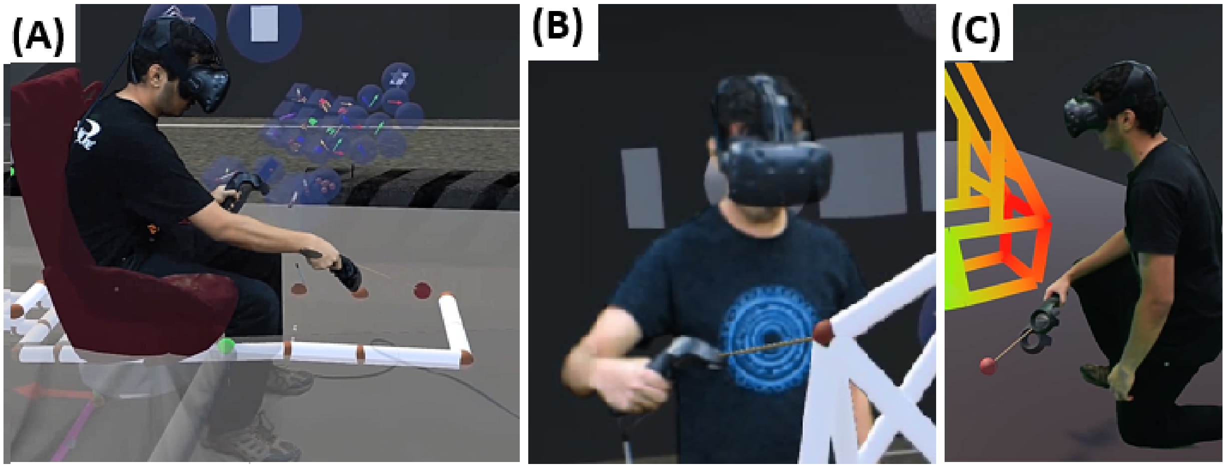

Figure 4.1: SpaceFrameVR's design and analysis workflow example: A designer wants to prototype and optimize a space-frame. (A) The designer starts prototyping the space frame by precisely placing points in 3D space around him using the virtual fixtures and constraints. The designer starts with prototyping the base frame. (B) The designer manipulates the spaceframe design in VR. And (C) The designer performs a finite element analysis to evaluate structural integrity and analyze the loading scenarios.

However, iterating using full-scale physical mockups is a resource-intensive task that limits the number of iterations of the product that can be tested during the conceptualization stage. Hence, design teams usually seek low-cost alternatives, like immersive virtual environments, to refine their designs and to explore any feasibility issues during the initial stages of the design process.

Visualizing the designs using immersive Virtual Reality (VR) environments has proven to be valuable for performing design reviews without constructing physical mockups, especially in industries like automotive, aerospace, and construction. The automotive industry has especially championed use of virtual reality to enable realistic spatial perception of CAD models across number of design activities including aesthetic evaluation, vehicle packaging, ergonomic analysis, visibility evaluation, and vehicle assembly. Many commercially available CAD tools today enable exporting meshes generated using CAD data for visualization in immersive virtual environments. Furthermore, VR-based interfaces has lead to the hope of making 3D-modeling more intuitive for the designer with less cognitive load for spatial visualization. However, most of the existing commercial tools use virtual reality as a stand-alone visualization environment and do not support real-time creation and modification of native CAD data in VR. Due to the identified drawbacks in VR-CAD integration, the designers have been constrained from taking full advantage of the modern VR-based interfaces while using state-of-the-art CAD tools.

Although considerable research has been devoted to exploring the feasibility of 3D-user interfaces for CAD modeling, none of these techniques have had a long-lasting impact on the evolution of the mainstream CAD systems or changed existing design workflow. Very few design engineers use virtual reality-based systems for their day-to-day design activities, especially since most of the 3D-modeling is done using the traditional 2D-interfaces (mouse and keyboard). In contrast, modern VR devices like Head Mounted Displays(HMD) offer low-cost, high-fidelity solutions for a fraction of the cost of traditional VR systems (e.g. CAVEs). It would thus be interesting to investigate how the new generation of VR devices would enable the adoption of VR more ubiquitous in the existing design workflow. Here we identify three key issues that have impeded the adoption of VR in the existing workflow: (a) It is very difficult for a small team of academic researchers to replicate all the capabilities of state-of-the-art CAD systems in VR. Hence, most VR-based interfaces for CAD modeling, as presented in previous work, tend to focus on a very specific feature or task. Furthermore, these features are generally evaluated using artificial domains or scenarios. Although this is useful to empirically study the "usability" of an interaction technique for a specific feature, it gives very little information about the "usefulness" of the new technique to the designer. The tasks encountered in a real-world conceptual design activity (like the design of automotive space frame) entail confounding complexities where the design needs to be concurrently evaluated using diverse domains (e.g. structural integrity, ergonomics, aesthetics, etc). For the systems proposed in the previous work, there is very little evidence of the designers being directly involved in the development of the workflow. (b) Previous work presented techniques that would require the designer to adapt to a completely new workflow. The proposed VR systems should blend into the existing workflows of the designer and communicate the geometric data with state-of-the-art tools. Although previous work has presented a technique to modify native CAD parts, the technique was evaluated for a task with very little confounding complexity. (c) Most of the VR-based CAD interfaces proposed in previous work were limited in application due to the high cost of legacy VR mediums, viz., Computer-Aided Visualization Environments (CAVEs), used for the interface. These legacy systems (CAVE environments) were normally reserved for high-priority tasks due to their capital cost. Thus the access to these CAVE systems for the day-to-day design activities was restricted, which also affected the adoption of VR in the design process.

This paper evaluates the feasibility of using a low-cost, commercially available VR hardware for the design, analysis, and optimization of an automotive space-frame, with the focus on the integration of the VR-based interface to the existing design workflow of mechanical design engineers. Previous research tends to focus on the interaction technique for a specific CAD feature or hardware technology for 3D user interaction in CAD, rather than on studying and integrating the VR interface with the existing design workflows of engineers. Hence, the adoption of VR technology for day-to-day design activities is uncommon. Therefore, to study the feasibility and the usefulness of VR for a specific engineering design task, we focus on a very specific user population encountered in most university settings with engineering programs. The members of the undergraduate student body are predominantly mechanical engineering students who participate in the annual design competitions organized by the Society of Automotive Engineering (SAE). The goal of this competition is to enable students to design, test, and build a formula racing vehicle to compete with other collegiate teams from around the globe. These formula racing vehicles are built using a space frame (or tubular frame chassis) which acts as the major structural component of the vehicle that supports the weight of other major components like engine, transmission, and fuel tank .We used the design goals obtained from task modeling to implement SpaceFrameVR: a virtual reality-based tool for design, analysis, and optimization of the automotive space frame. A review study shows that SpaceFrameVR can enable faster design workflow for the space frame, and reduce the physical prototyping cost by completely

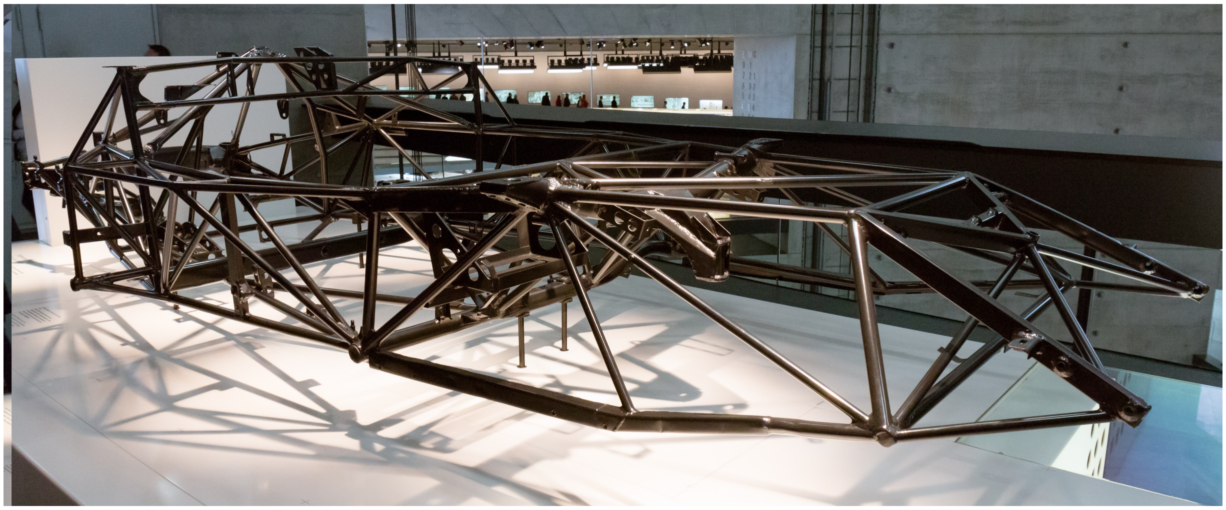

Figure 4.2: W198 space frame, Mercedes-Benz Museum, Stuttgart, Germany. File reproduced under Creative Commons Attribution-ShareAlike 3.0 [1].

replacing some parts of the design process. The preliminary review suggests that SpaceFrameVR can encourage more design iterations for optimizing the design and stimulate creative solutions.

Our paper makes the following contributions to the research in 3D user interfaces with specific applications in Computer-Aided Design for engineers:

1. This paper, for the first time, presents a fully VR-based prototyping framework that integrates modeling and analysis tools along with 3D modeling aids necessary to achieve precision and constraints required for engineering designs. The concept of using virtual fixtures and virtual constraints to achieve precision can also be extended to other VR prototyping applications.
2. We demonstrate the basic principles and feasibility of using Virtual Reality for Computer-Aided Design, with an application in the context for designing a space frame.

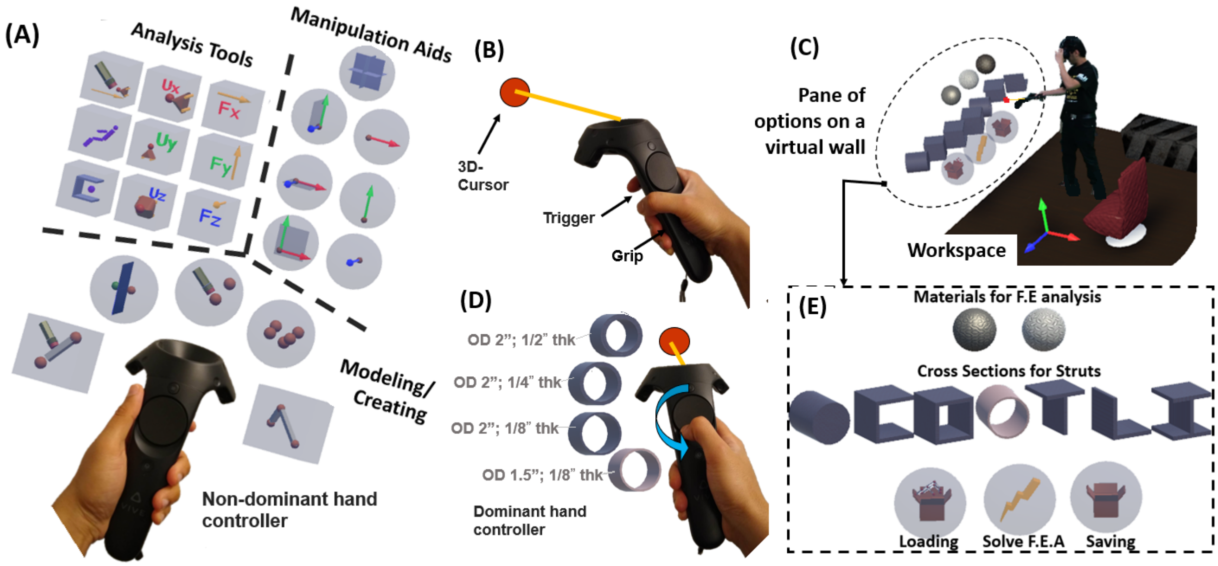

Figure 4.3: SpaceFrameVR's User Interface: The designer uses 3D-controllers (A) and (B) to interact with the virtual environment. The 3D controller in the dominant hand behaves like a spatial mouse with a spherical cursor (B). The designer uses the trigger, thumbpad, and grip buttons for design, selection, and manipulation in VR (B) and (D). The user interface in the virtual environment is separated into two parts—interface elements on the controller of the non-dominant hand (A), and interface elements along the wall of the virtual environment (E). Frequently used elements, such as those required for modeling, manipulation, and analysis, are placed on the controller grabbed by the non-dominant hand for quick access to the buttons (A). The options are visually grouped according to their functionality (A). Sparsely used interface elements, like those required for the selection of materials, selection of cross-sections, and file operations are represented on the wall in the virtual environment (C) and (E).

4.2 Relevant Work

Instead of using digital mediums, like CAD applications, many designers have preferred using physical mediums such as free-hand sketching or creating physical mock-ups for conceptual design [79, 80, 81]. Designers in the automotive industry have traditionally created concept sketches using black photographic tape placed on large vertical surfaces—a process called “Tape Drawing” [82]. These 2D tape drawings are then converted into 3D form by sculpting clay models using “styling clay”[83]. Although such design and visualization at the 1:1 scale factor are useful to evaluate the aesthetics, it is tedious to digitize these designs into 3D data and maintain the original designs [82, 84]. Previous research has proposed 3D-user interfaces for digital tape drawing and clay modeling [82, 84, 85]. However, tape drawing or clay modeling equivalents only take into consideration the aesthetic evaluation, thus leaving complex considerations, like structural and ergonomic evaluations, for further steps in the design workflow [85]. Previous research by Peng et al. and Mueller et al., have proposed 3D-printing the low-fidelity wireframe prototypes to analyze and verify the critical aspects of design [86, 87]. Leet et al., and Agarwal et al., have suggested approaches to create physical mockups of space frame structures [88, 89]. However, the greatest drawback of physical mockups is that the designs cannot be manipulated or iterated without creating a new prototype. Additionally, 3D printing prototypes is not always possible, especially for large scale objects (e.g., automobile) where evaluation using a 1:1 scale factor is desired.

Previous research has suggested novel interaction techniques that augment the desktop-based interface to make 3D modeling intuitive. Kim et al. presented “SketchingWithHands,” a 3D modeling interface where the designers can continuously record hand postures and use the captured hand posture data to prototype hand-held devices while maintaining a proper scale and ergonomics for those devices [90]. Song et al. presented an interface where the sketches made on the physical model can be interpreted by the system to trigger operations in the CAD environment[91]. However, the approach presented by Song et al. and Kim et al. requires physical objects to be integrated into the design workflow, which might be expensive for large scale products. Numerous approaches of using tablets tracked in 3D space have been proposed for interior design and architectural modeling [92, 93, 94, 95]. For example, Li et al. presented a sketch-based interface using a tablet for interior designing, where the users can perform exploratory 3D modeling in the context of images of the interiors [92]. However, most of these interaction techniques are standalone systems for design and lack compatibility with the existing design workflow.

Sketch-based and freeform modeling interfaces that emulate sculpting have long been used in the artistic designs. Sketch-based modeling interfaces, like "ShapeForm" [96] and "Teddy"[97], enable the flexibility to create free-form models, like stuffed toys, using a digital pen. Qin et al., suggested a physics based frameowrk approach for Computer-Adied Geometric Design[98]. Matsumiya et al., and Evans et al. have demonstrated a 3D interface for a freeform design using implicit surfaces [99, 100]. However, these freeform design tools lack the precise model representations required for engineering designs and do not emulate the design workflow of an engineer. Schulze et al., and Hughes et al. presented a VR modeling interface using a Constructive Solid Geometry-based approach that limits the user to the creation and modification of predefined 3D-shapes, which can lead to premature design fixation [101, 102]. 3D-painting using VR has been explored in applications like "Google TiltBrush"[103] and "CavePainting"[104]. However, most commercial and academic CAD tools (like AutoDesk VRED [105], Ansys OPTIS[106],Advanced Systems Design Suite (ASDS)[107]) use VR for visualization of the 3D geometric generated using desktop tools and do not allow manipulation of geometric data directly in VR.

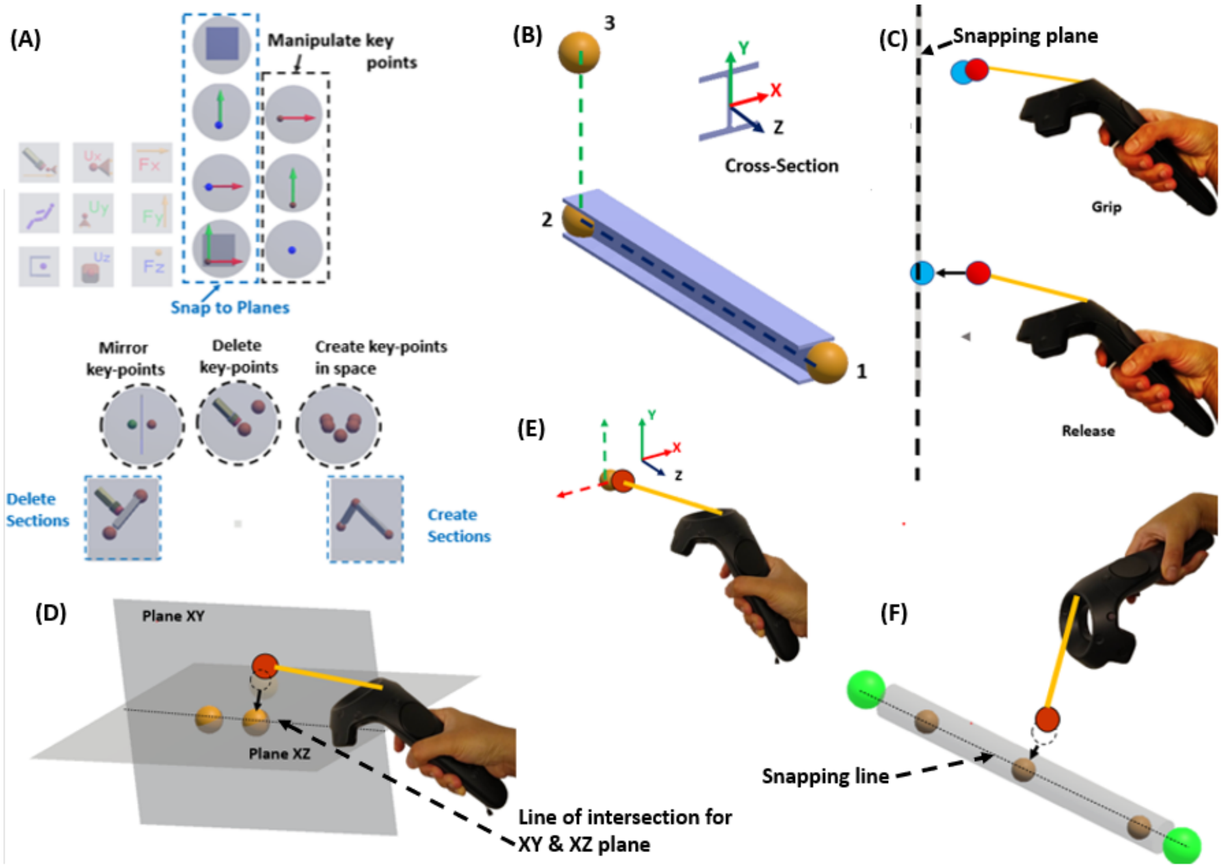

Figure 4.4: SpaceFrameVR's Interface and Workflow for Modeling and Manipulating the space frame. (A) The user interface enables the user to create, manipulate, delete, and mirror the key-points; and create and delete the structural members. (B) The designer can create the structural members by defining two endpoints of the member (i.e., 1-2) and the third point to define the orientation of the cross-section (i.e, 2-3). (C) The designer can either define a virtual "snapping plane" or use a pre-existing snapping plane to constrain the points to a single plane. All the points within a certain threshold away from the snapping plane will be constrained to that plane. (D) If the snapping planes intersect, the key-points will snap to the line intersection for the two planes. (E) The user can manipulate the key-points by constraining their motion along a specific direction.(F) The user can also define a "snapping cylinder" to ensure that the selected key-points are collinear.

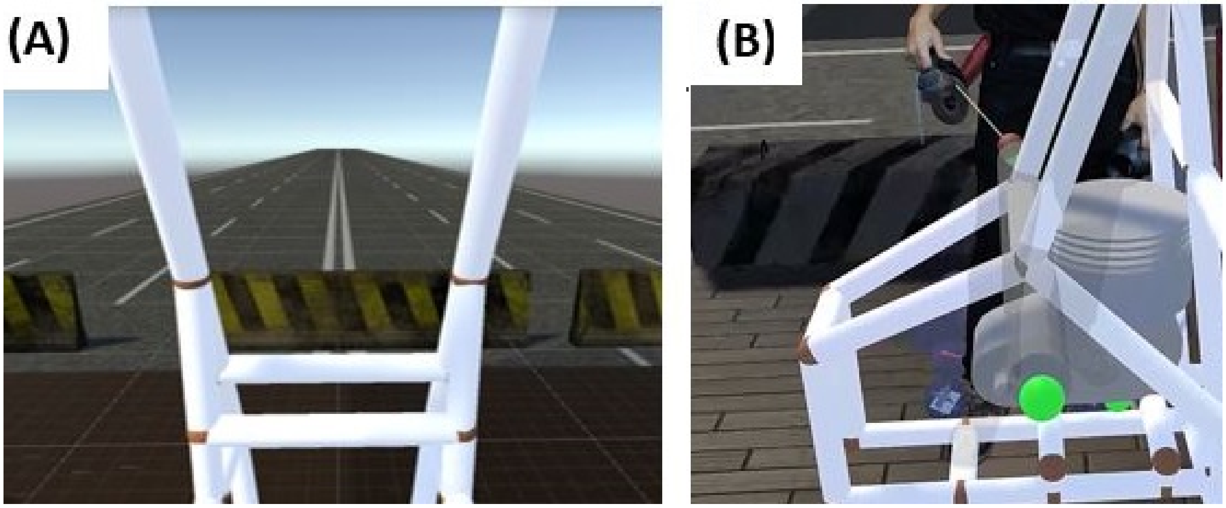

Figure 4.5: SpaceFrameVR's interface for performing a volumetric visualization. (A) The user can evaluate his access to the dashboard and the steering wheel (B) The designer can use the 3D volumetric models of the bulky components, like engine, to evaluate their accessibility for maintenance.

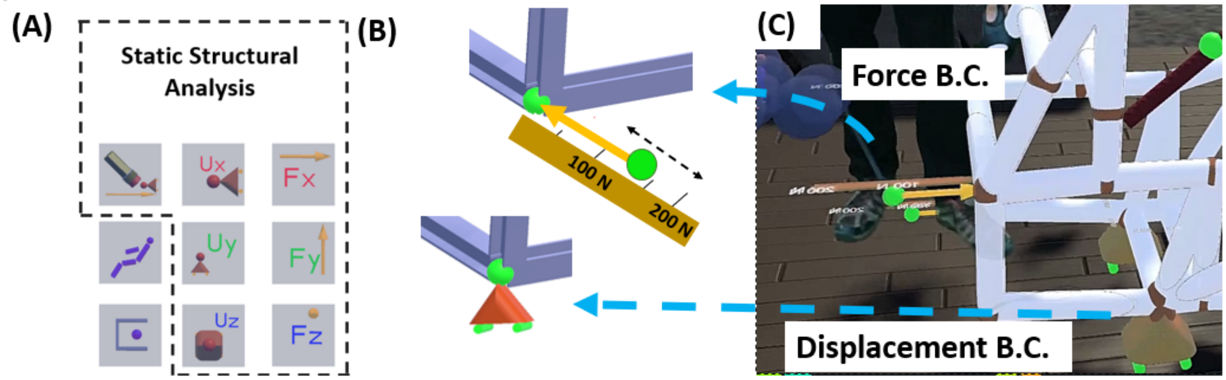

Figure 4.6: SpaceFrameVR's interface and workflow for performing a finite element analysis (FEA) on the space frame structure. (C) SpaceFrameVR enables the designer to apply or modify the existing forces and displacement boundary conditions in X, Y, and Z direction. (A) and (B): The designer can directly apply these boundary conditions in the desired direction on the key-points of the structure in VR. The user can adjust the magnitude of the force by scaling the force arrow. A reference scale allows the user to visualize the approximate magnitude of force applied.

4.3 Understanding the Design Goals

Based on the contextual inquiry exercise, as presented in previous work, the workflow in the VR should not be drastically different than the traditional workflow, but rather it should support and extend the existing work practices [108]. The design goals obtained from the task models succinctly describe the features, qualities, and capabilities desired in new VR system. Based on the results from the contextual enquiry, we distilled the following main design goals for our VR tool to facilitate smooth integration with the engineer's design workflow:

DG1: Create and manipulate the spatial envelope in VR with the desired precision and constraints

DG2: Enable ergonomic evaluation of the prototypes without the need to construct physical mockups.

DG3: Enable structural analysis (using FEA) of prototypes and visualization of results within the VR tool

DG4: Intertwine the design and analysis tools for iterative prototyping and easy integration into the existing design workflow.

4.4 The SpaceFrameVR System

Here we reiterate the principles of user-interface design for SpaceFrameVR as described in the previous work:

4.4.1 User Interface and Interaction

Interaction Hardware: The most popularly used virtual reality interfaces today are head-mounted displays (HMDs), which are also easily accessible in the market. These HMDs allow the users to interact with their environment using 6-DOF controllers with interaction techniques similar to those used by gaming controllers. Hence, to make the tool accessible to a wider audience, we use a commercially available HMD (over table-top displays or CAVE systems) for the design of our VR interface. Additionally, the task of designing a space frame at a 1:1 scale factor involves moving around in space and interacting with the space frame from different viewing perspectives. Hence, we chose a VR interface that enables interaction at the room-scale, the HTC Vive, as the VR HMD for the SpaceFrameVR system. Although, in theory, SpaceFrameVR can be used with any commercial VR HMD.

Interaction Technique: We use a spherical cursor on the spatially tracked controller for the dominant hand for selection, manipulation, and interaction with the menus and the virtual environment (Fig.4.3(B)). We use the trigger button on the controller to create, delete, and select the geometric elements (e.g., key-points, member structures) for the space frame prototype (Fig.4.3(B)). We use the grip button for manipulation of the space frame geometry and to position the virtual snapping planes in the virtual environment (Fig.4.3(B)). The use of the thumbpad is limited to make a secondary selection for the tubing size or gauge used for modeling the space frame structure. The user can select the options on the wall menus by physically walking to the wall and interacting with the menus using the 3D cursor in the virtual environment (Fig.4.3(C) and (E)).

Interface Layout: We prototyped various user interface layouts using volumetric techniques in a virtual environment. We evaluated their feasibility based on the ease of use, similarity to existing interaction metaphors, and minimal physical effort required by the designer. We found that an interface with the frequently used menus options on one of the controllers (preferably the controller for the non-dominant hand) and sparsely used options in the menus on the virtual wall to be the best suitable layout for our application. Using the task model, we estimated the frequency of each menus option and configured the layout for our SpaceFrameVR UI as a combination of frequently menu options on the controller (Fig.4.3 (A)) and sparsely used menu options along the wall of the virtual environment(Fig.4.3(C) and (E)). The menu on the controller presents options to trigger features that are frequently used, such as creation, manipulation, and analysis of space frame (Fig.4.3(A)). The options for creation, manipulation and analysis are presented distinctly in the menu based on the Gestalt's principles of grouping, as shown in Fig.4.3(A). Interface elements that are sparsely used, such as the options to select the state of the system (e.g., material and the type of cross-section for modeling the structural members, and file operations such as loading, saving) are presented on the wall in the virtual environment (Fig.4.3(C) and (E)).

Visual Affordances: Affordances are interface elements that help the designer to predict the actions possible after selecting a specific option, and also help predict the interaction [109]. Useful affordances reduce the time to learn and get familiar with the new interface [109]. Our menu buttons consist of 3D mesh models that are inspired by the metaphors and symbols from an existing CAD interface in order to facilitate the designer to recognize the functionality of these buttons easily. e.g., the option for solving the FEA analysis is represented by an equivalent "lightning" symbol, which is used commonly in a commercial FEA package [106] (Fig. 4.3(E)).

4.4.2 Design Rationale and Workflow

We used the design goals (DGs) obtained from the contextual inquiry to guide the rationale for the SpaceFrameVR workflow. SpaceFrameVR has features that enable the design engineer to meet each of the design goals (DGs) obtained using the contextual inquiry, as described in Section-2 of this paper. The SpaceFrameVR workflow for the design of the automotive space frame can be described using a case study, as presented in Fig. 4.1. Here we describe how the key features of SpaceFrameVR were used to achieve the design goals (Section-2 of this paper) and to prototype the space frame (Fig. 4.1):

Step 1: Creation of key-points for the spatial envelope of the space frame (DG1)

Creation of key-points using* virtual fixtures*: The first step for the design of a car frame is a task predominantly requiring a spatial sense. In this step, the location of the key-points for the frame is estimated, and the spatial envelope is prototyped based on factors like driver comfort, visibility, and the packaging of bulky components (e.g., engine). In SpaceFrameVR, the designer simulates being seated in the car and starts prototyping the spatial envelope by directly placing the key-points in the 3D space around him. The designer starts prototyping the base frame by creating the key-points and the members connecting the points . The designer uses a virtual fixture, which we call *snapping plane*, to ensure that all key-points in the base frame are constrained to a single plane (Fig. 4.4(C)). The designer can also enforce a collinearity constraint for the desired key-points in the space frame by either (A) Using another virtual fixture, which we call *snapping line* (Fig. 4.4(F)), or (B) Using two intersecting *snapping planes* (Fig. 4.4(D)).

Functionality of* virtual fixtures*: The functionality of *virtual fixtures* differentiates SpaceFrameVR from other art-based prototyping tools. Virtual fixtures enable the designer to enforce geometric constraints on the design elements. There are two main virtual fixtures presented in SpaceFrameVR: *snapping plane* and *snapping line*. The snapping plane enables the user to constrain a set of points to a single plane. The position on a key-point that is created within 2.5 cm from the plane is automatically updated to the nearest position on the plane, and the point remains constrained to that plane (Fig. 4.4(C)). When the key-point is created or manipulated near the intersection of two *snapping planes*, the key-points are constrained along the line of intersection between the two planes (Fig. 4.4(D)). Similar to *snapping plane*, *snapping line* enforces a collinearity constraint to all points within the cylindrical threshold (Fig. 4.4(F)). The user creates and can align the *snapping line* along any direction and position in space. SpaceFrameVR enables grabbing and manipulating the key-points of the design constrained manner in X, Y, and Z directions. These virtual fixtures enable the designer to build prototypes with the precision and constraints required for an engineering design (Fig. 4.4(F)). Using these virtual fixtures early on in the prototyping process also reduces the amount of post-processing required later in the design workflow.

Reflecting the key-points for symmetric design: The designer then uses the option to reflect the key-points about the symmetry plane of the car (Fig 4.4(A)), Mirror key-points). Reflecting the key-point along the symmetric plane ensures that any spatial manipulation to the key-point is also reflected on the other side of the space frame. The designer then proceeds to the next step for creating the member sections connecting the key-points.

Step 2: Creation of spatial envelope by connecting the key-points of the space frame (DG1)

The designer selects the material and cross-section of the structural members from the selection panel (Fig 4.3 (C),(D),(E)). The designer then connects the key-points in space with the structural members to create a prototype of the space frame. The structural members are defined using three key-points (Two endpoints and third point to define the orientation for the cross-section of the member, (Fig 4.4(B)).

Step 3: Ergonomic analysis for occupant comfort and safety (DG2)

Traditionally, the ergonomic analysis was performed by physically constructing the mockup of the space frame or by using a virtual human model in the CAD environment. Previous work has demonstrated the success of using immersive visualization for ergonomic analysis and visibility simulation [110]. However, most of the approaches for ergonomic analysis before are stand-alone visualization systems without the ability to manipulate the design in VR[110]. SpaceFrameVR enables the designer to manipulate the space frame while evaluating the occupant's comfort. In SpaceFrameVR, the designer can experience being seated in the car and evaluate front and side visibility from the car seat. The designer can construct the maximum-reach-envelope in

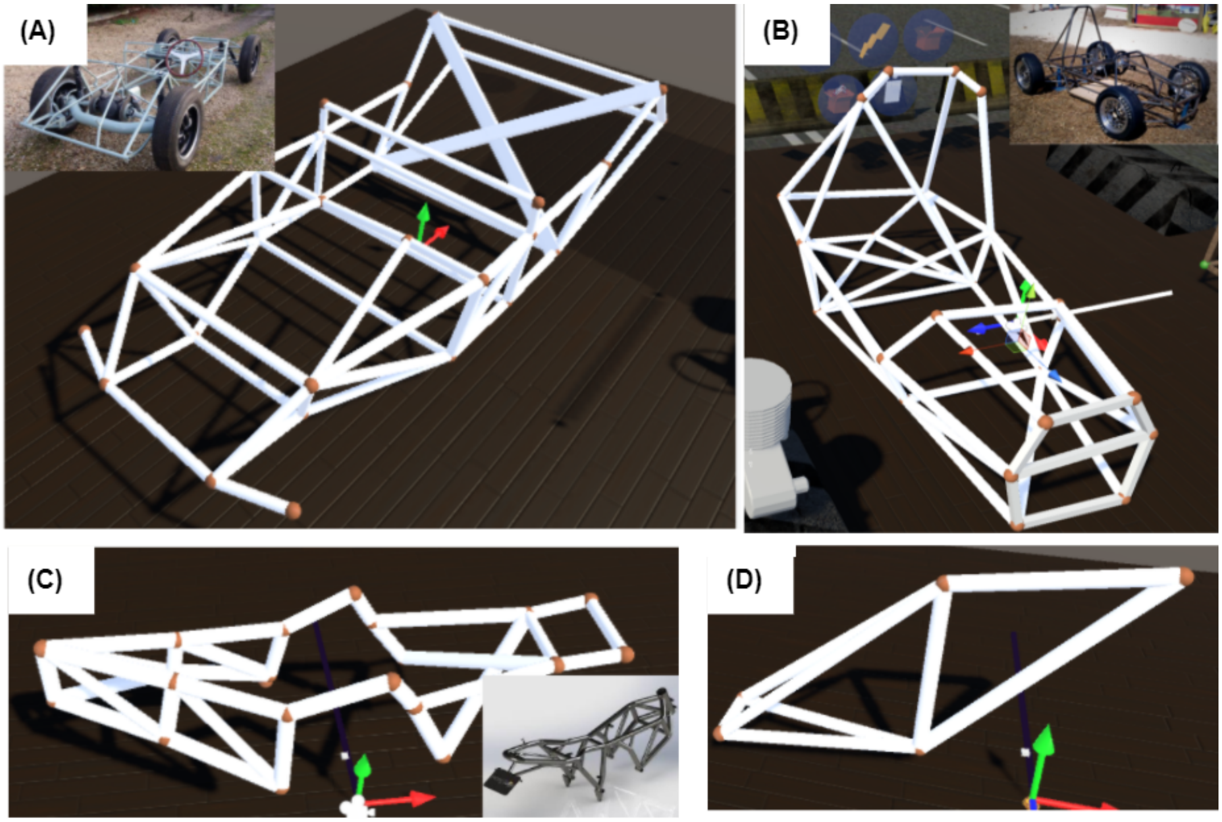

(E) Benchmarking with state-of-the-art

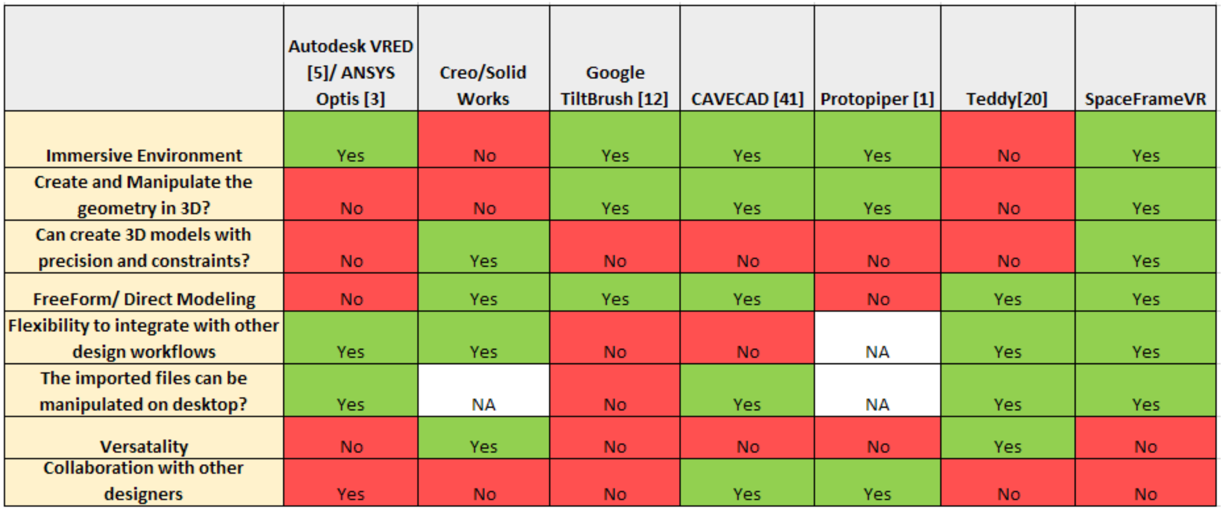

	Autodesk VRED [5]/ ANSYS Optis [3]	Creo/Solid Works	Google TiltBrush [12]	CAVECAD [41]	Protopiper [1]	Teddy[20]	SpaceFrameVR
Immersive Environment	Yes	No	Yes	Yes	Yes	No	Yes
Create and Manipulate the geometry in 3D?	No	No	Yes	Yes	Yes	No	Yes
Can create 3D models with precision and constraints?	No	Yes	No	No	No	No	Yes
FreeForm/ Direct Modeling	No	Yes	Yes	Yes	No	Yes	Yes
Flexibility to integrate with other design workflows	Yes	Yes	No	No	NA	Yes	Yes
The imported files can be manipulated on desktop?	Yes	NA	No	Yes	NA	Yes	Yes
Versatality	No	Yes	No	No	No	Yes	No
Collaboration with other designers	Yes	No	No	Yes	Yes	No	No

Figure 4.7: Evaluation of SpaceFrameVR using (A-D) Demonstrations created using SpaceFrameVR. (E) Benchmark evaluation by comparing the key features of VR modeling tool with the state-of-the-art

space and evaluate the reachability of steering and other critical controls on the dashboard (Fig. 4.5 (A)). Additionally, the designer can use 3D volumetric models of the bulky components, like engines, to evaluate their accessibility for maintenance (Fig. 4.5 (B)). SpaceFrameVR intertwines the creation and manipulation of CAD data with ergonomic evaluation, thus eliminating the need to go back-and-forth between a 2D CAD tool and the VR environment for visualization. SpaceFrameVR has the potential to completely replace the need for physical or CAD mockups for ergonomic evaluation of space frame.

Step 4: Finite element analysis to evaluate the structural integrity and visualize the loading scenarios (DG3)

Traditionally, finite element analysis is performed for a preliminary evaluation of the structural integrity of the space frame. Traditionally, the designs have to be imported in a commercial FEA tool and evaluated for all structural requirements. This process of interfacing between different software tools can be complicated and time-consuming. SpaceFrameVR enables applying the input boundary conditions for FEA, including forces and constraints, in the virtual environment(Fig. 4.6). The designer can solve the FEA analysis for the desired loading conditions and immediately visualize the results in the VR environment (Fig. 4.6). SpaceFrameVR enables the designer to manipulate the space frame structure and visualize the effects of those changes within the VR interface. SpaceFrameVR offers an advantage by saving the complex effort of transitioning between VR and desktop-based analysis tools.

Step 5: Design exploration by iterative manipulation and integration with a commercial CAD/CAE tool (DG4)

The total weight and the position of the center of mass are the critical optimization parameters for the design of a space frame. It is desirable to have the center of mass as low as possible to allow steep turns without rolling over. The horizontal position of the center of mass should be between the front and rear axle, and should be biased towards the rear axle to achieve equal load distribution on all tires during deceleration and braking. SpaceFrameVR enables the designer to rapidly iterate the designs to optimize the weight and center of mass while enabling the designer to evaluate the designs for structural and ergonomic requirements. The intertwined workflow for design, visualization, and analysis offered by SpaceFrameVR enables rapid iterations in the designs and avoids design fixation observed in the desktop-based CAD tools.

4.5 Evaluation

In this section, we first discuss the existing methods for evaluating systems research. We then derive which of these evaluation methods are appropriate and useful to evaluate SpaceFrameVR. We then elaborate the evaluation of SpaceFrameVR using four methods: (a) Demonstration using a range of example designs and use cases, (b) Formative studies using walk-through demonstrations and open-ended interviews, (c) Evaluation using Olsen's framework, (d) Benchmarking against the state-of-art.

4.5.1 Discussion on Evaluation Methods

Choosing the appropriate method to evaluate systems research is challenging, especially since misapplied evaluation methods can mute creative ideas that are still in the early stages of development [111, 112]. Researchers perform evaluation to show the efficiency or effectiveness of a particular technique or to demonstrate improved human performance using a new interface. Empirical evaluation using controlled user studies is a commonly practiced technique for evaluating user interfaces in the HCI community [112]. Although usability evaluation is valuable in many situations to produce statistically comparable results, a user study would only be able to examine a small subset of the SpaceFrameVR tool, and would not demonstrate the usefulness of SpaceFrameVR in its context of use [111, 112]. Additionally, controlled user studies fail to capture the subjective arguments, opinions, and reflections of the design experts who are the intended users of SpaceFrameVR. As summarized by Olsen[113] in his review paper on evaluating toolkits research, usability evaluation or usage study would be inadequate for evaluating systems research like SpaceFrameVR for the following reasons: (a) The “walk-up and use” assumption—SpaceFrameVR is intended for a particular target audience (mechanical engineers designing automotive space frame) and requires specialized domain knowledge like principles of space frame design, a background on CAD modeling, and an understanding of basic principles of mechanical engineering. Hence, a usage study that assumes that all participants have minimal training or similar skills might not be valid. Additionally, it is difficult to obtain users with specialized domain knowledge in the numbers required to produce statistically significant outcomes. (b) The Standardized task assumption—There is no standard way to approach the problem of automotive space frame design, and the design outcome depends on the skills and experience of the designer. The inherent variability in the knowledge and skills of the potential users would result in a variability the outcome. (c) The scaling problem—Designing an automotive space frame for participating in annual competitions organized by the Society of Automotive Engineering (SAE) is a lengthy process with confounding complexities. This process of designing and optimizing the space frame for the annual competitions is undertaken by students over a period of six to nine months. A usage study completed in a period of one to two hours does not accurately mimic the context of use of SpaceFrameVR.

Previous work has identified several overarching strategies that we believe are also relevant for evaluating a toolkit such as SpaceFrameVR. We use a combination of these strategies to demonstrate the value or the usefulness of SpaceFrameVR for mechanical engineers (specifically engineers designing automotive space frame). In the next section we demonstrate and show the vision of what could be the expected scenarios, use cases, or case studies where SpaceFrameVR is useful. We then perform a preliminary user feedback session using walkthrough demonstrations to verify that the tool is conceptually clear and valuable to the space frame designers. We record the opinion, preferences, and reflections of the designers to understand the impact of SpaceFrameVR within its context of use. We finally apply an established standard (Olsen's thematic framework) used for evaluating complex systems to reflect on the feasibility of SpaceFrameVR. We also benchmark the performance of SpaceFrameVR with the state-of-the-art VR design tools.

4.5.2 Example Design and Use cases

As discussed earlier in the paper, we interviewed the designers and perform work modeling to understand the requirements of the designer. We probe the demands of the designer and develop understanding of the existing design process. The workflow and the design rationale of SpaceFrameVR was motivated by understanding the requirements of the designer using a user-centered design process. Throughout the *SpaceFrameVR system* we explore and elaborate SpaceFrameVR in depth by demonstrating the functionality and showing how the different pieces of SpaceFrameVR come together. In addition, here we elaborate the functionality and feasibility of SpaceFrameVR within other complex design scenarios. In Figure 4.7 (A) & (B) we demonstrate SpaceFrameVR being used to prototype a complex commercial (space frame for Lotus MK XI) and academic (space frame for the Formula SAE competition by students from the Mechanical Engineering Department at the University of Western Australia) space frame designs respectively. These prototypes, which would normally take a few hours to be recreated in a CAD environment, were created by the authors in under 45 minutes. The prototypes in Fig 4.7(A) & (B) show that SpaceFrameVR reduces the complexity and effort required to develop space frame designs. We believe that application of SpaceFrameVR can easily be extended to neighboring design spaces like Motorbike and bicycle framr design. Fig. 4.7(C) shows the chassis design for Ducati Trellis prototypes using SpaceFrameVR. Fig. 4.7(D) shows a bicycle frame prototyped and analyzed for structural integrity by a new user in the 30 minutes of using SpaceFrameVR. The prototype of a bicycle created by a new user demonstrates the user's ability to get started with SpaceFrameVR. Overall, we demonstrated SpaceFrameVR's purpose and exhibited the feasibility, breadth, and depth of its applications.

4.5.3 Preliminary user feedback

The target audience and the usefulness of the design of new systems and toolkits is often unclear [112]. To overcome this challenge, SpaceFrameVR was developed using a user-centered design approach by understanding the requirements of the target audience. We performed an informal user evaluation with a group of students from mechanical engineering to verify that the tool is conceptually clear. During the feedback session with the chassis designers we asked a set of questions to understand the value of SpaceFrameVR in their existing workflow for the design of automotive chassis.

Participants: Since the target audience for this tool were the students in department of Mechanical and Aerospace Engineering, we interviewed students to understand the usefulness of this tool. We had students from our university's formula racing organization to participate in the feedback session. They were a part of the formula racing organization participates in the SAE (Society of Automotive Engineering) Formula racing competition held annually, where university student organization compete with other teams in the areas of design, analysis, and commercialization. The organization compromises of undergraduate students predominantly in Mechanical and Aerospace Engineering department at our university. All participating designers were proficient in SolidWorks for CAD/ 3D modeling and two participants were proficient using the finite element software packages. In addition to the chassis designers, we also interviewed graduate students in Mechanical and Aerospace Engineering who were proficient in using commercial CAD and analysis tools, and have past experience participating in Formula SAE events.

Procedure: We first conducted a guided session showing the toolkit to the participants and gathered overall impressions on SpaceFrameVR. During the guided session we explained the different elements of SpaceFrameVR together with the examples and limitations. Using SpaceFrameVR, we then imported and visualized one of the current designs that the formula racing team was working on for the next season of competition. We then conducted an open-ended interview and a feedback session on the workflow utility and usefulness of SpaceFrameVR. The opinions from the feedback sessions are summarized in the following sections:

Overall impression and feedback: In general, the participants were enthusiastic about using SpaceFrameVR in their existing workflow in designing the space frame of a formula racing car for the upcoming FSAE competition. All participants were excited to spatially visualize the design of their chassis using SpaceFrameVR, thus eliminating the need to build physical mock-ups. Two participants appreciated the ease of using a 3D-controller to modify the chassis design in 3D space. All participants from the university formula racing team believed that SpaceFrameVR would stimulate creative design solutions and would encourage more iterations on the design. We believe that more design iterations enable the designers to prototype and refine their ideas quickly without any fatigue. One participant believed that SpaceFrameVR can reduce the cost of physical prototyping by completely replacing some parts of the design process. One participant quoted that "in such a virtual reality-based system, only imagination is the limit for our car design". We have currently deployed SpaceFrameVR to be used by the formula racing team for designing their chassis for the upcoming FSAE competition.

Shortcomings discovered: We also discovered some designer preferences and usability issues during the feedback session. The designers were able to get an idea of the spatial envelope around the driver by sitting at the drivers seat and viewing from a first-person perspective. However, most designers preferred having a virtual mannequin in the VR environment for performing ergonomic analysis. The designers preferred the ability to have a mannequin that they could move and modify in the VR environment, as normally used in conventional CAD tools. The designers believed that a third-person view gave them a better sense of the spatial envelope for ergonomic analysis. The participants mainly expressed concerns about not being able to view the entire body (feet, hip, etc.) in VR. Additionally, participants would have preferred to have the ability to collaborate on chassis design by connecting virtually in the same VR space. We are in the process of addressing both these designer preferences in future work. The designers also suggested to incorporate haptic feedback for events and operations such as modifying the chassis, selecting key-points, and applying forces or boundary conditions, etc.

New opportunities discovered: Although we designed SpaceFrameVR to support the spatial layout (or vehicle architecture) of critical components, the participants were excited about another use case with similar goals—chassis fabrication and assembly. The space frame described in this paper are normally fabricated by welding pipe sections together. The quality of weld in this process (e.g., tungsten arc welding) is affected by the welding tool used for the difficult-to-reach areas. The chassis designers were interested to see the feasibility of using different styles of welding tool in the difficult-to-reach areas in their current Computer-Aided Design, and requested us to import the true scale model of their weld tool for spatial visualization and ergonomics analysis during fabrication of the space frame. Future work could implement improvements in the features to analyze design for manufacturability. Additionally, one participant proposed the ability to scale the virtual world to perform ergonomic analysis on space frame for population throughout the range of percentiles (e.g., for people who are short or tall).

4.5.4 Performance Benchmarking

We qualitatively compared SpaceFrameVR with the state-of-art CAD solutions, VR tools, and methodology for creating physical mockups. Although SpaceFrameVR performs better for free-form modeling and direct manipulation of the design, the tool still lacks versatility and collaboration aspect Fig 4.7(E). We found that although SpaceFrameVR was best suited for the application of the design of space frame structures, the tool lacked key features like versatility and collaboration.

Chapter 4, or portion thereof, is being prepared for publication of the material. Jadhav,

Saurabh; Xu, Zhuoqun; Gasques-Rodrigues, Danilo; Schulze, Jurgen P.; Tolley, Michael T. The dissertation author was the primary investigator and author of this paper.

Chapter 5

Conclusion

In this work, we have explored three major research questions: (a) How does actuation system with inherent passivity (like changing stiffness on the fly),be used to enable a device for stable and robust haptic interaction? (b) How can we minimize the required number of electromechanical valves to control a large array of actuators, and design systems that scale favorably in complexity with the number of actuators? (c) How can the design of 3D-user interfaces support the limitations in input devices to enable the interaction required for the high-precision task? We addressed these questions in each of the previous three chapters, respectively.

In Chapter 2, we presented the modeling and versatile applications of fiber jamming—a phase changing mechanism useful for application in devices that require slenderness and controllable flexural stiffness. We introduced an analytical model to predict the stiffness curve for the FJM for various loading conditions. We experimentally tested our model at different vacuum pressures, different tube sizes, and choice of infill fiber material. We tested the performance of the FJM with three choices of infill fibers and contrasted it with the performance of a granular jamming FJM of the same size and form. We demonstrated the implementation of our model to design a kinesthetic force feedback haptic glove for interaction with AR environments. The glove design enabled a full range of motion in the fingers and full hand closing while providing a finger, palm, and side opposition in the jammed state. The glove design was application-driven, and the size and form of the FJMs for the glove were calculated based on the analytical model presented in this article. The slender modules made the haptic glove compact and compliant for varying hand sizes. Finally, we demonstrated the FJM as a load-bearing component in a deployable truss structure.

Future work could explore replacing the existing components for the pneumatic actuation setup with miniature valves and vacuum pumps and also study the effects on the latency of actuation. While we have also presented an alternative thermal actuation method using heat shrink tubing as the outer envelope for the fibers, this actuation method is irreversible. Future research could explore non-pneumatic methods of actuation, using materials that respond to thermal or chemical stimuli, creating an effect similar to the pressure-induced by applying a vacuum to the inner chamber. Shape memory alloys surrounding the envelope could be used to apply external pressure on the jamming structure and actuate it reversibly. Regardless of the method of actuation, it is possible to predict the performance of the FJM by calculating the equivalent pressure acting on the fibers and then using the analytical model presented in this article.

Another drawback of FJMs is that they have relatively high bending stiffness in the unjammed state compared to granular jamming modules. The bending stiffness of the FJMs, in the unjammed state, may be reduced by packing more fibers in the FJM (i.e., using smaller fiber diameters to reduce the overall stiffness of the FJM in the unjammed state).

Overall, this work presents the concept of fiber jamming as an alternative for variable stiffness actuation in robotics. The analytical model presented in this article can be used in any application-driven design to calculate the size and form of FJM, the type of fibers required, and the vacuum pressure required in the system. This approach has the potential to provide a low-cost solution for high force-to-weight devices for application in soft robots, medical devices, and wearable interfaces.

In Chapter 3, we presented a pneumatic circuit inspired by a dot-matrix display for the

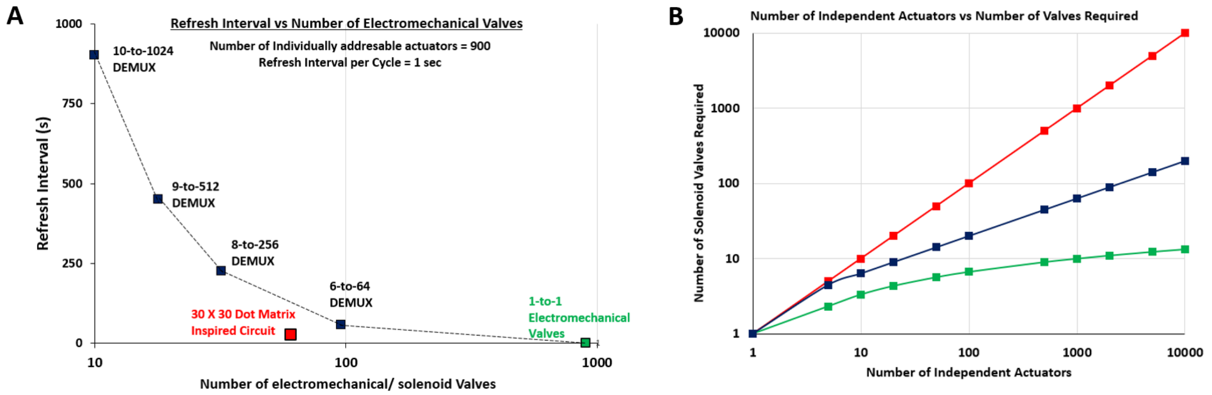

Figure 5.1: Comparison of the dot-matrix-inspired fluidic circuit to the previously demonstrated demultiplexing and conventional approaches for using electro-mechanical valves. (A) The dot-matrix-inspired fluidic circuit has a lower refresh interval as compared to demultiplexing approach for same number of electro-mechanical valves controlling 900 actuators individually. For controlling 900 valves with a refresh interval of 30 s, the dot-matrix-based circuit requires 60 valves and the demultiplexer requires 150 valves. (B) Comparison of the number of valves needed using each approach for controlling a known number of actuators. The dot-matrix-inspired circuit is a tradeoff between minimizing the number of valves required and the refresh interval for the display.

independent control of a large array of fluidic actuators. We demonstrated the application of this display for the rapid actuation of flip-flops (syringe) as well as soft elastomeric actuators. Previous work in microfluidics and soft robotics has used pneumatic multiplexing for distributed control of a large array of actuators which can only control a single actuator at any given instant. Our method enables the user to control an entire set of actuators simultaneously enabling shorter refresh intervals for each actuator and thus high refresh rates for the fluidic displays. The Figure 5.1 compares the scalability of our approach with the traditional approach of using 1-to-1 electromechanical valves, and demultiplexing approach presented by [5]. We demonstrated the application of our proposed design to control a 5 × 5 2D shape display and a pneumatically actuated haptic vest. Future work could include scaling down the system that would increase the portability of the system for applications in untethered soft robots or onboard wearable devices.

In Chapter 4, we presented SpaceFrameVR, a tool based in virtual reality for the design, analysis, and optimization of space frame. Using SpaceFrameVR, we demonstrate the techniques and principles for designing 3D-User Interfaces for high precision task with existing commercially available hardware. The features and the workflow of SpaceFrameVR were formulated based on the design goals. The VR interaction was designed with the principles of user interface design and interaction in mind. We demonstrated a step-by-step case study to illustrate the aspects of SpaceFrameVR. We benchmarked SpaceFrameVR with state-of-the-art applications for designing and prototyping. We also demonstrate the versatality of SpaceFrameVR in different problem spaces. Our anecdotal review suggests that SpaceFrameVR would stimulate creative design solutions and can lead to faster product development and iteration. SpaceFrameVR extends the designer's work practice instead of completely replacing it. After optimizing the space frame design in SpaceFrameVR, the user still needs to create drawings to cut the pipe sections, design and analyze the welded joints, and physically prototype the space frame. We believe that virtual reality interfaces can augment certain parts of the traditional design process, but cannot wholly replace the 2D CAD tools.

Our work addresses the following advancements over previous work as compared using Olsen's thematic framework approach [113], as previously used in [114, 115]:1) Problem not previously solved; 2) Reduced Solution Viscosity to enable rapid prototyping of spaceframe; 3) Power in Combination: we use commercial CAD tool for integration of VR in the existing workflow; 4) Empowering new design participants: The VR tool itself is easy to use and has low barriers to entry, which could people from different discipline to participate in the design process.

Future work could focus on studying collaboration in VR for engineering designs. Another aspect to explore is novel interaction techniques to augment features from commercial CAD tools (e.g., SolidWorks by D'Assault Systèmes) in the VR interface. We believe that the interaction techniques presented in this paper would encourage the application of virtual reality in diverse activities requiring high precision and the control of the virtual tools. Future work could focus on adding more modeling functionalities (i.e., adding tools tailored for the design of structures beyond space frames), and also studying the aspects of collaborative design in VR.

Appendix A

Appendix A: Supplemental Material for Variable Stiffness Devices Using Fiber Jamming for Application in Soft Robotics and Wearable Haptics

Control of the pneumatic system: The actuation of the fiber jamming-based haptic glove is controlled by switching the state of 3/2 flow control solenoid valves (VQ 300 Series, SMC Pneumatics; Fig. S1). The solenoid valves are part of the fluidic control board with a microcontroller (Arduino Mega, Arduino) that communicates with the virtual environment (Meta2, Meta; Fig. S1(B)). When the user grabs the balloon, a signal is sent by the virtual environment to the fluidic control board to actuate the glove (Fig. S1). A pump with a high flow rate is desired to minimize any latency. In the experiment, a pump with a flow rate of 3 cubic feet per minute was used to avoid latency in the haptic feedback experienced by the user and to make response time under 1 second, which was unnoticeable to the users.

Assumptions in the Analytical Model: The flexural formula assumes that the plane

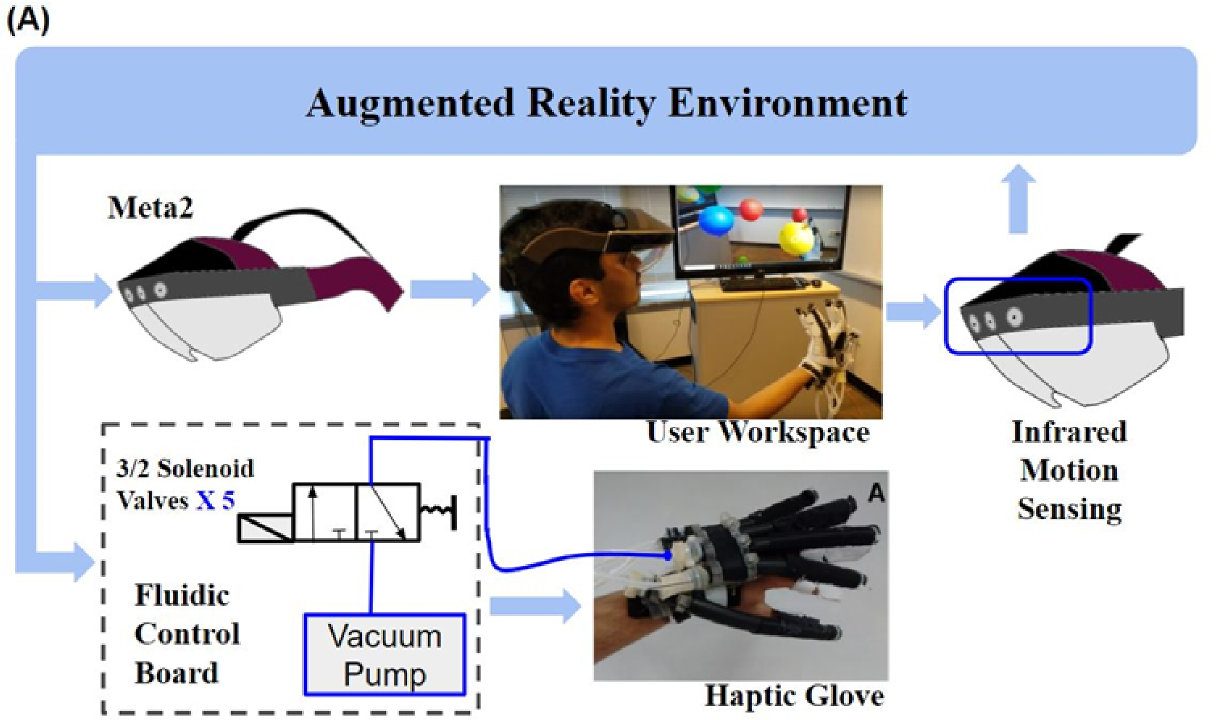

Figure A.1: Schematic of the pneumatic system for the haptic glove: The schematic of the system shows the user interacting with the virtual balloons using the AR headset and wearing the fiber jamming-based haptic glove to grab and pop the balloons. The hand is tracked using the inbuilt optical tracking system in the headset and the feedback signal is provided to the software and the fluidic control board to actuate the haptic glove.

sections along the beam remain plane, and longitudinal fibers curve uniformly along the length of the beam. However, in reality, as the module bends, deformation occurs within the plane of the section. The section of the ellipse which is in tension above the neutral axes will contract perpendicular to the direction of fibers, and the section of the ellipse below the neutral axes, which is in compression, will expand as evident from the representative simulation in Fig. S2 (right). This phenomenon causes a change in the ellipse size by slightly rearranging the fibers. The extent of change in cross-section depends on the external vacuum pressure. This property of the FJM explains the variation in its bending stiffness before slipping, as a function of the external vacuum pressure. The FJM behaves like granular material in the transverse direction. The approach to calculating the deflection of the composite beam after slipping based on the bending stiffness is predicated on the assumption that the traction force during slipping has a

Table A.1: Outer Envelope Properties for the FJM Test Specimens

Tube Material	Commonly Used For	Nominal Tube Size	Measured Inner Circumference of the Tube
Butyl Rubber	Bicycle tube	700 X 32C-35C	59.03 ± 0.68 mm
Butyl Rubber	Bicycle Tube	700 X 20C-28C	41.45 ± 0.83 mm
Silicone Elastomer	Milk hose/ Dairy tubing	No nomenclature defined	9.62 ± 0.39 mm (DIAMETER)

negligible effect on the overall performance of the beam.

The dimension of the Outer Tube Envelope: We tested the analytical model presented in the paper using three different cross-section sizes of the FJM, which we refer to small, medium, and large size. The size of the outer envelope affects the module cross-section. We used butyl rubber tubes as an outer envelope for medium and large-size FJMs. Since butyl rubber is very elastic with a small thickness, it would produce a negligible effect on the bending stiffness of the FJM in line with our assumptions. We used a silicone tube for small-size FJM. Since these commercially available tubes have a wide variety of size ranges, we measured the length of the inner circumference of the tube manually to be used further in our calculations. Table S1 describes the details of the tubes used in the experiments. All readings are presented at a 68% confidence interval.

Empirical Determination of the Coefficient of Friction for the Fiber Material: We tested the analytical model presented in the paper using three different fiber surface roughness. The slipping force is dependent on the coefficient of friction for the fiber material. We used aluminum oxide abrasive cords and 3D printed fibers with two kinds of surface topography to

Table A.2: Properties of fiber material

Fiber type	Fiber Material	Diameter of Fiber	Static Coefficient of Friction
Mitchell's Abrasive 54	Aluminum Oxide, 180 Grit	0.762 mm	0.96 ± 0.13
3D Printed	VeroClear with a square wave texture (Pitch = 2 mm, Amplitude = 0.5 mm)	1.000 mm	0.61 ± 0.20
3D Printed	VeroClear without texture (Smooth)	1.000 mm	0.28 ± .04

compare with our model. We calculated the coefficient of friction for the fibers from the sliding friction test using an Instron UTM. Fig. A.3(B) describes the test setup used for the sliding friction test. For the sliding friction test, we used aluminum oxide sandpaper of grit size equivalent to abrasive cords and glued the sandpaper to the base to estimate the coefficient of friction for the aluminum oxide abrasive cords. We 3D printed the base and the sliding plate with a topography similar to fibers and estimated the coefficient of friction for 3D printed fibers. The maximum pulling force obtained using a sliding friction test was used to calculate the static coefficient of friction. Table S2 describes the results of the experiment. We conducted a minimum of seven trials for each case, and all readings are presented at 68% confidence interval.

Fabrication and Assembly of the FJM: The fibers were packed in the tube envelope to ensure that there is sufficient clearance between the fibers to avoid any prestress effects caused by force applied by stretching of the envelope around the fibers.

Empirical Determination of the Packing Factor and FJM Cross-Section Dimensions: We estimated the packing factor for each module empirically to estimate the amount of the volume in FJM that is occupied by fibers. We measured the total volume occupied by the FJM by jamming the module and submerging it in a measuring cylinder (Fig. A.4).

We estimate the equivalent cross-section area of the module sample by knowing the length of the FJM and the total volume occupied by the FJM as obtained from the experiment. We then calculate the ellipse dimensions for each sample by using the known circumference of the outer envelope and the equivalent cross-section area of the ellipse as described in equation (S1), (S2).

$$\text{Approximate Circumference } = \pi(a+b) \tag{A.1}$$

$$\text{Area } = \pi * a * b \tag{A.2}$$

Empirical Determination of the Initial Bending Stiffness for the FJM: If the beam were made up of homogeneous material, we would have used Young's modulus of fiber to calculate the bending stiffness of the beam. However, in the case of FJMs, we estimated the initial bending stiffness of the FJM by fitting the initial half region of the Force-Deflection curve under the calculated slipping transition force S1.

Numerical Simulation to Calculate the Area Moment of Inertia: The centroid and moment of area for higher-order slipping transitions is calculated numerically using the trapezoidal rule technique for all partial elliptical cross-sections (Fig. A.5). The area, centroid, and moment of inertia for partial elliptical cross-sections were calculated using the formulas described in equations (S3)-(S6). The maximum step size (h) used for all numerical calculations is 0.5 mm.

Explicit representation of ellipse equation:

$$x_i = \frac{a}{b}\sqrt{b^2 - y_i^2} \tag{A.3}$$

Area of the elliptical cross-section in y-direction:

$$A_{1\to n} = 2\sum_{i=1}^{n-1} \frac{h}{2} * (x_i + x_{i+1}) \tag{A.4}$$

The centroid of the elliptical cross-section in y-direction:

$$y_c = \frac{\sum_{i=1}^{n-1} \frac{h}{2}\left(x_i + x_{i+1}\right)\left(y_i + \frac{h}{2}\right)}{\sum_{i=1}^{n-1} \frac{h}{2}\left(x_i + x_{i+1}\right)} \tag{A.5}$$

Moment of inertia of the elliptical cross-section about an axis parallel to the neutral axis passing through the centroid of the section:

$$I_{xx} \text{ at } y_c = 2\sum_{i=1}^{n-1} \frac{h}{2}\left(x_i + x_{i+1}\right)\left(y_i + \frac{h}{2} - y_c\right)^2 \tag{A.6}$$

Experimental Characterization: We performed the cantilever beam bending experiments at three different values of vacuum pressure- 90 kPa, 45 kPa, and 0 kPa (No vacuum). All experiments conducted were a single sample test with seven trials for 90 kPa and 45 kPa actuation pressure, for each sample. We conducted three trials for 0 kPa (no vacuum) case.

Finite Element Modeling to calculate the correction factor for elliptical cross-sections ($k_{elliptical}$): In the case of layer jamming, the points along the cross-section of the beam in the horizontal direction start slipping simultaneously when the shear stress exceeds the maximum shear resistance (hence, in this case, the average shear stress can be used to predict the slipping condition). However, in the case of fiber jamming, the fibers along the cross-section in the horizontal direction can start slipping independently along the single layer, similar to crack propagation. Hence, it is more appropriate to use the maximum shear stress along the horizontal direction to predict the yield condition for the beam. The correction factor used to calculate the shear stress at slip corrects the failure stress to the maximum shear stress induced in the elliptical beam as explained in Figure 2.3 (J) of the main text. We used ANSYS Mechanical to calculate the correction factor for varying aspect ratios of elliptical cross-sections. We modeled the cantilever beam with the orthotropic material property. Based on Saint-Venant's principle, we plotted the shear stress distribution in the cantilever beam for center 80% of the length of the beam to avoid

Table A.3: Correction factor for a range of ellipse cross-sections

The ratio of Major-to-Minor Axis (ae/be)	$k_{correction}$	The ratio of Major-to-Minor Axis (ae/be)	$2*k_{correction}$
0.01	0.882105	0.81	2*1.029552
0.04	0.94839	1.5625	1.097431
0.0625	0.98108	2.25	2*1.182654
0.25	1.015067	4	1.398525
0.49	1.014556	5.0625	2*1.498903

noise due to stress concentrations near the boundary conditions since the shear stress distribution can be significantly affected at the boundary regions where the point load and the fixed support is applied. We used the maximum and average stress obtained from the shear stress distribution to obtain the correction factors.

Fabrication of Fiber Jamming based Haptic Glove and Morphing Structure: The fiber jamming glove and the morphing structure were fabricated using Butyl rubber tubes as the envelope for fibers. The parts used for these demonstrations are 3D printed using a commercial 3D printer (Form 2, FormLabs). The variation in spacing between the fingers for different hand sizes requires the exoskeleton that is anchoring the variable stiffness modules to be adaptable and compliant. A layer jamming based haptic glove design as presented by I. Zubrycki et al., and Y. Zhang et al., would not be adaptable to this variation in finger spacing since the layer jamming modules cannot bend in the plane of the layers. Additionally, the thumb (which can move and bend in space) is constrained to bend in a single plane by the layer jamming based glove design (31,39). The ability of the fiber jamming modules to bend in space makes the fiber jamming based haptic glove design compliant to different hand sizes and does not constrain the motion of the thumb to a single plane.

Calculation of Shear Force for Complex shapes of Fiber jamming Module: A finite element based approach can be used to calculate the maximum shear force in the fiber jamming modules for applications requiring the FJMs to bend in complex shapes. For example, we calculate the maximum shear force acting on the fiber jamming modules used for the demonstrations shown in Fig 2.1 using a commercial finite element tool. This maximum shear force can be used further in the analytical model to calculate the critical design parameters for the fiber jamming device. If the shear force at any point in the module exceeds the maximum shear stress that the fibers can resist, the fiber jamming module will undergo slipping transition and would fail to resist the loading condition.

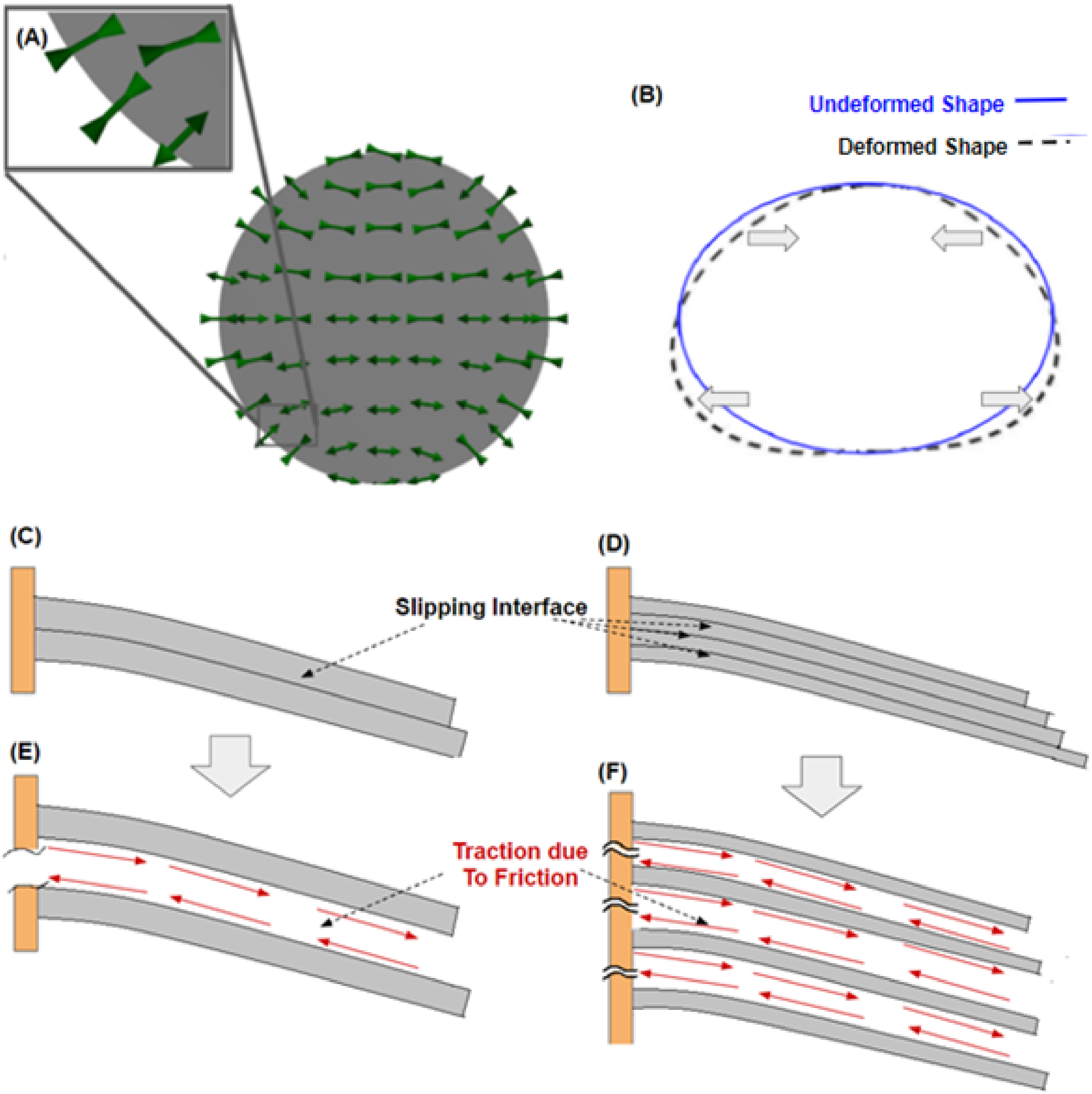

Figure A.2: Limitations of the analytical model (A) The direction of longitudinal shear stress in the ideal case is always orthogonal to the boundary of the outer elliptical envelope. For modeling purposes, we assume that the direction of shear stress is always parallel to the neutral axes. (B) In-plane deformation plot of a cross-section of a cantilever beam with point load: The plot shows x-direction deformation of points within the elliptical cross-section. The neutral axis of the ellipse is along the x-direction. As seen from the figure, when a point load is applied to the end of the cantilever beam, the top half of the circular cross-section tends to contract, and the bottom half of the ellipse tends to expand. This tendency of the cross-section of the cantilever beam causes the fibers to rearrange during bending. (C-D) Representation of the fiber jamming module undergoing a single (C) and three (D) slipping transitions along the longitudinal sections of the beam. (E-F) The sliding along the longitudinal sections of the beam undergoing slipping transition generates traction. We assume this effect of the bending resistance due to the traction to be negligible in comparison to the resistance to bending caused by the stiffness of the cohesive longitudinal sections of the beam.

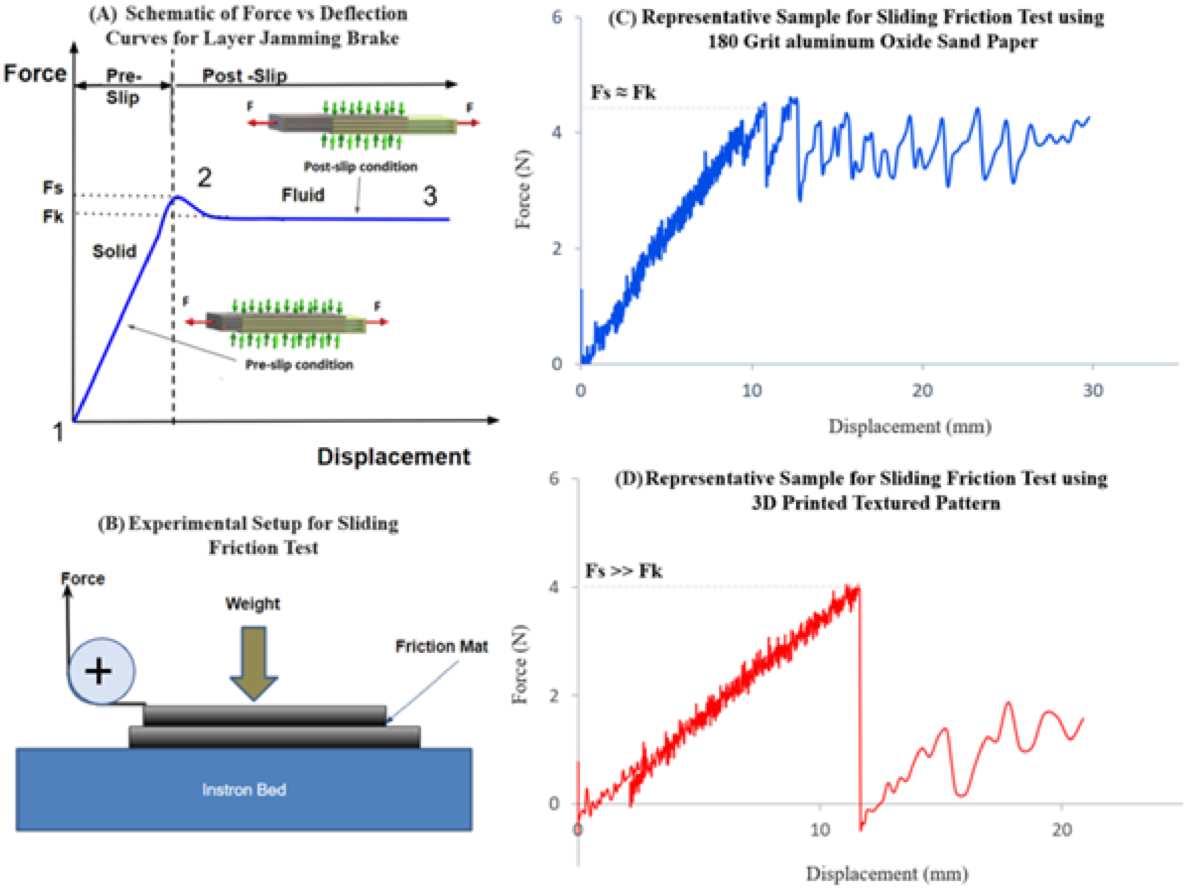
(A) Schematic of Force vs Deflection Curves for Layer Jamming Brake

(B) Experimental Setup for Sliding Friction Test

(C) Representative Sample for Sliding Friction Test using 180 Grit aluminum Oxide Sand Paper

(D) Representative Sample for Sliding Friction Test using 3D Printed Textured Pattern

Figure A.3: Empirical calculation of the coefficient of friction for the fiber material: (A) Schematic of Force vs. Displacement curve for sliding friction test. When frictional resistance is higher than the tensile stress, the displacement linearly increases with the increase in force. When the tensile stress exceeds frictional resistance, the layers slide freely relative to each other with constant frictional resistance. (B) Schematic of the experimental setup for the sliding friction test. (C)& (D) Representative results obtained from sliding friction test for 3D printed textured pattern and 180 Grit aluminum oxide sandpaper. For sandpaper, the static and kinetic coefficient of friction is approximately equal (Fs=Fk), which causes the stick-slip response. For the 3D-Printed texture, the static coefficient of friction is considerably higher than the kinetic coefficient of friction (Fs¿¿Fk).

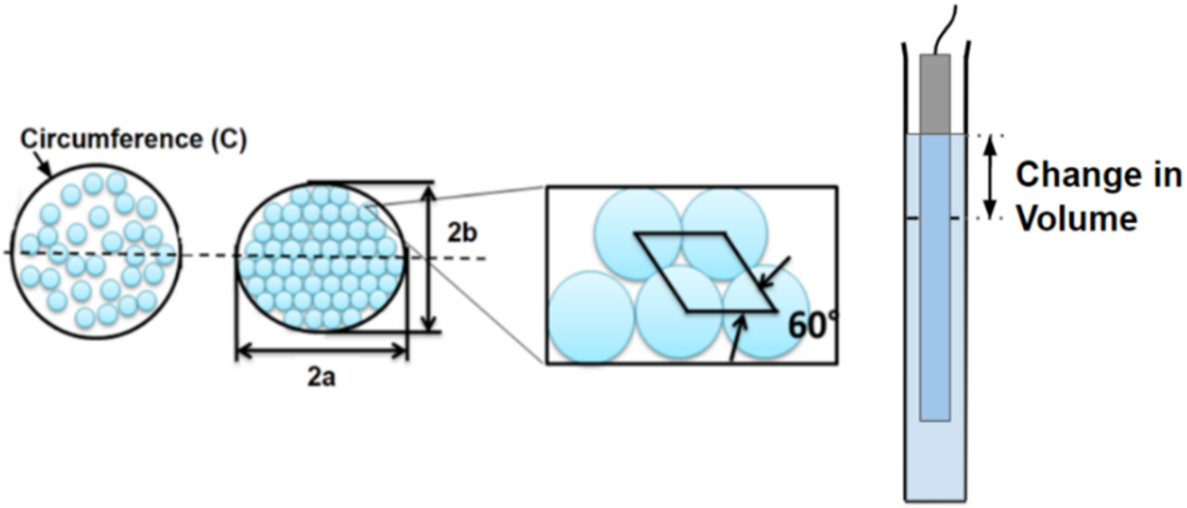

Figure A.4: Empirical calculation of ellipse dimensions: (Left) The circular envelope collapses into an elliptical shape when the vacuum is applied. The dimensions of the ellipse depend on the number of fibers within the envelope and the circumference of the ellipse. (Right) Experimental setup to calculate the packing factor for the FJM.

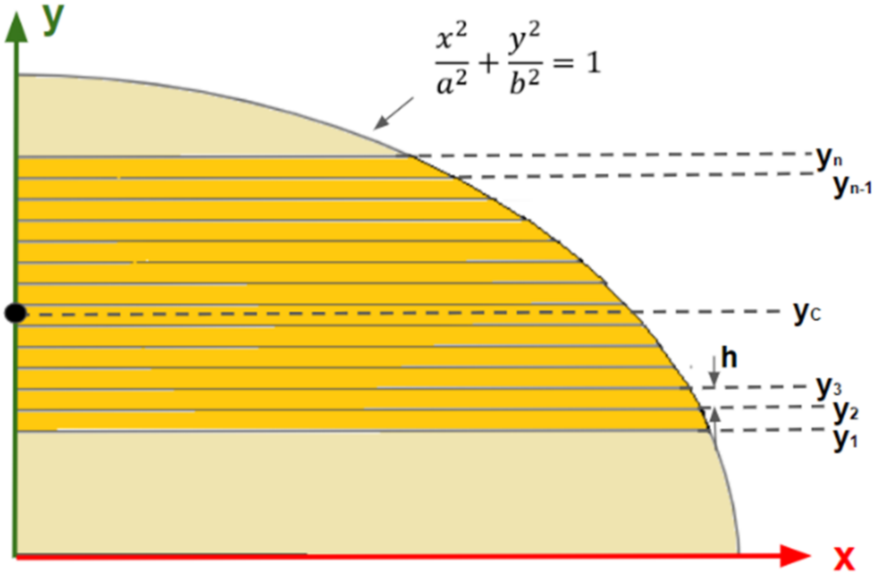

Figure A.5: Finite Element Modeling to calculate the correction factor for elliptical cross-sections ($k_{elliptical}$): In the case of layer jamming, the points along the cross-section of the beam in the horizontal direction start slipping simultaneously when the shear stress exceeds the maximum shear resistance (hence, in this case, the average shear stress can be used to predict the slipping condition). However, in the case of fiber jamming, the fibers along the cross-section in the horizontal direction can start slipping independently along the single layer, similar to crack propagation. Hence, it is more appropriate to use the maximum shear stress along the horizontal direction to predict the yield condition for the beam. The correction factor used to calculate the shear stress at slip corrects the failure stress to the maximum shear stress induced in the elliptical beam as explained in Figure 3 (J) of the main text.

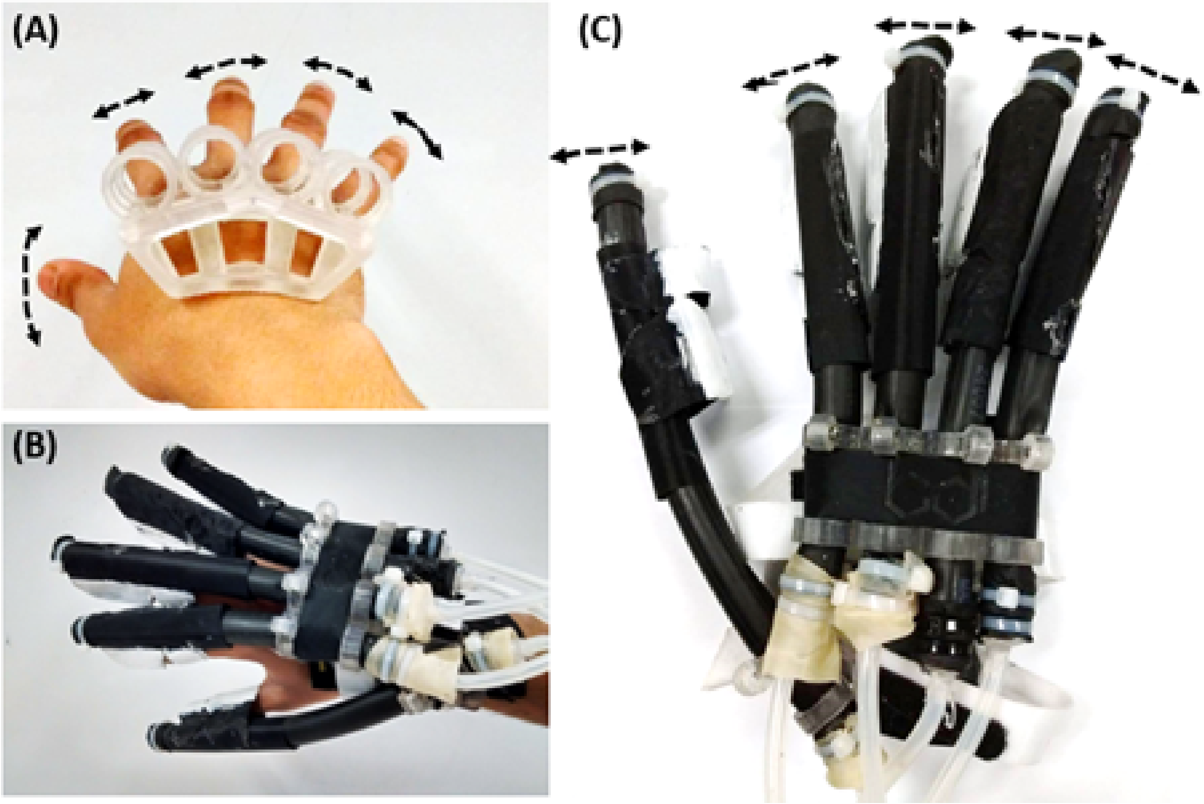

Figure A.6: The adaptability of the fiber jamming based haptic glove. (A) The spacing between the fingers will vary depending on hand size, and the exoskeleton needs to adapt to this variation in spacing. (B)& (C) The ability of fiber jamming modules to bend in space makes it adaptable to variation in hand sizes and also does not artificially constrain the motion of the thumb to a single plane

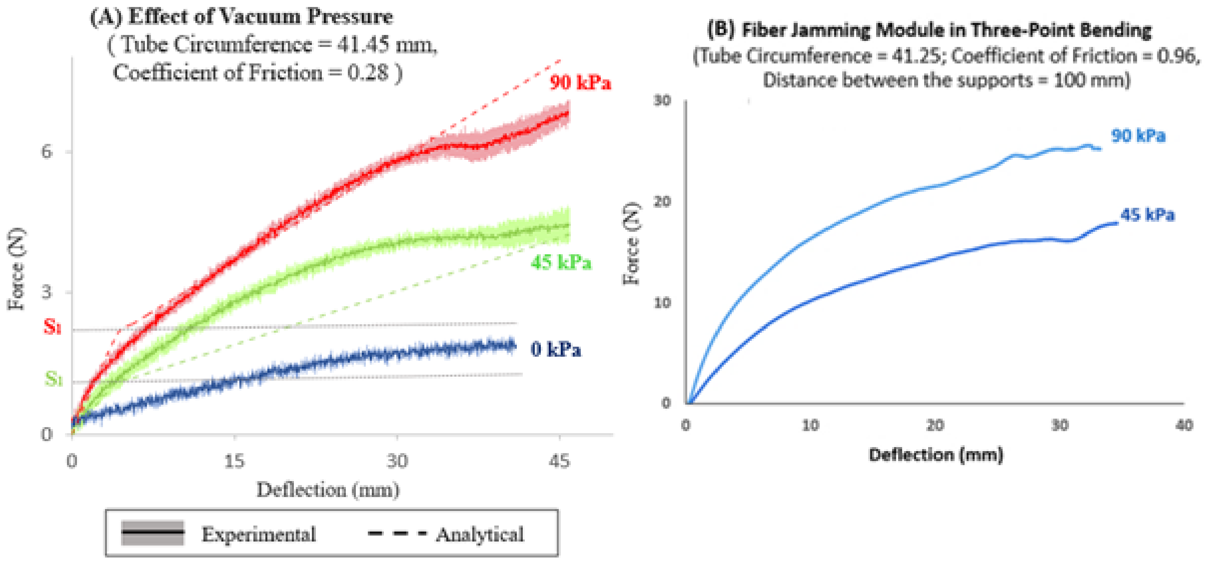

Figure A.7: Additional experimental results for fiber jamming module (A) Force vs Deflection plot for fiber jamming module at 90, 45, and 0 kPa for plain fibers (B) Representative trials of fiber jamming module in a three-point bending (simply supported) loading configuration.

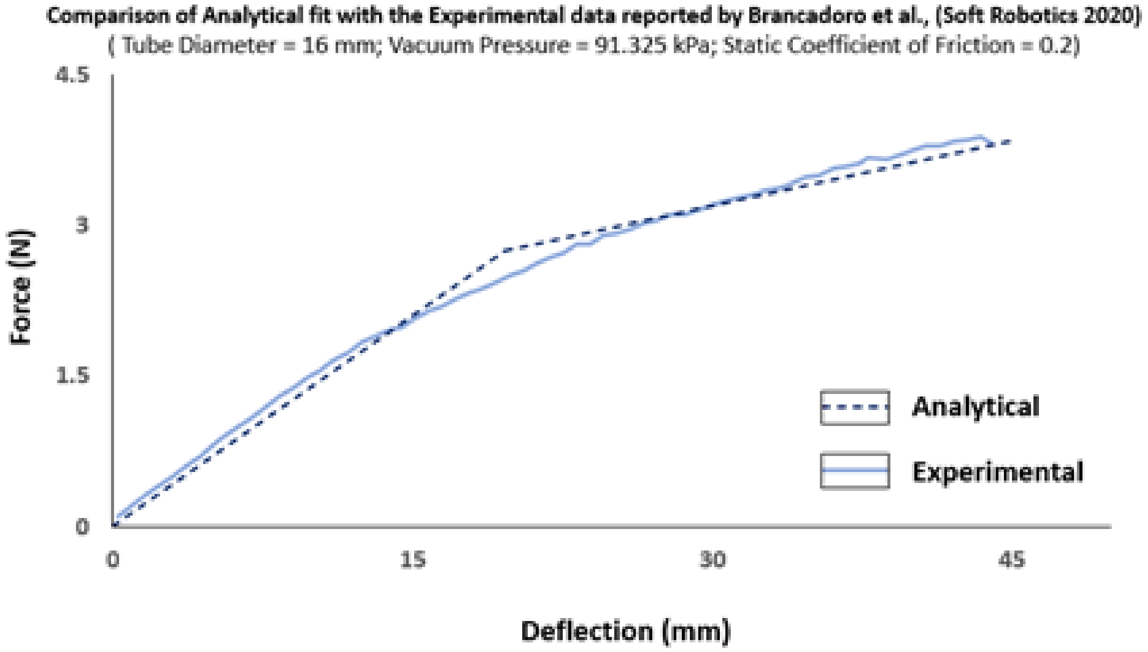

Figure A.8: Comparison of our Analytical Fit with the Experimental Data reported by Brancadoro et al., (Soft Robotics 2020). The reported tube diameter = 16 mm and vacuum pressure = 91325 Pa. We assumed coefficient of friction = 0.2 for nylon to nylon contact (The Engineers Toolbox, Coefficient of Friction)

Bibliography

[1] Morio, “Mercedes-benz w198 space frame chassis rear-left 2013 mercedes-benz, museum, https://creativecommons.org/licenses/by-sa/3.0/deed.en,” 2012.

[2] D. J. Preston, P. Rothemund, H. J. Jiang, M. P. Nemitz, J. Rawson, Z. Suo, and G. M. Whitesides, “Digital logic for soft devices,” *Proceedings of the National Academy of Sciences*, vol. 116, no. 16, pp. 7750–7759, 2019.

[3] D. J. Preston, H. J. Jiang, V. Sanchez, P. Rothemund, J. Rawson, M. P. Nemitz, W.-K. Lee, Z. Suo, C. J. Walsh, and G. M. Whitesides, “A soft ring oscillator,” *Science Robotics*, vol. 4, no. 31, 2019.

[4] D. Drotman, S. Jadhav, D. Sharp, C. Chan, and M. T. Tolley, “Electronics-free pneumatic circuits for controlling soft-legged robots,” *Science Robotics*, vol. 6, no. 51, 2021.

[5] N. W. Bartlett, K. P. Becker, and R. J. Wood, “A fluidic demultiplexer for controlling large arrays of soft actuators,” *Soft matter*, vol. 16, no. 25, pp. 5871–5877, 2020.

[6] C. Majidi, “Soft robotics: a perspective—current trends and prospects for the future,” *Soft robotics*, vol. 1, no. 1, pp. 5–11, 2014.

[7] L. Wang, Y. Yang, Y. Chen, C. Majidi, F. Iida, E. Askounis, and Q. Pei, “Controllable and reversible tuning of material rigidity for robot applications,” *Mat Tod*, vol. 21, pp. 563–576, 2018.

[8] L. Blanc, A. Delchambre, and L. P. F. medical devices, “Review of controllable stiffness solutions,” *In Actuators*, vol. 6, 2017.

[9] Y. Yang, Y. Li, and C. Y., “Principles and methods for stiffness modulation in soft robot design and development,” *Biodesign Manufac*, vol. 1, pp. 14–25, 2018.

[10] J. HM., “Celebrating soft matters 10th anniversary: toward jamming by design,” in *Soft matter11*, pp. 12–27, Crossref. PubMed, 2015.

[11] X. Gu, Y. Zhang, W. Sun, Y. Bian, D. Zhou, and P. O. Kristensson, “Dexmo: an inexpensive and lightweight mechanical exoskeleton for motion capture and force feedback in vr,” in

Proceedings of the 2016 CHI Conference on Human Factors in Computing Systems, (CHI'16, ACM), pp. 1991–1995, New York, NY, USA . Crossref, 2016.

[12] E. Strasnick, C. Holz, E. Ofek, M. Sinclair, and H. Benko, "Haptic links: bimanual haptics for virtual reality using variable stiffness actuation," in *Proceedings of the 2018 CHI Conference on Human Factors in Computing Systems. , NY: ACM p. 644*, 2018.

[13] G. Senatore, Q. Wang, H. Bier, and P. Teuffel, "The use of variable stiffness joints in adaptive structures," *In Proceedings of IASS Annual Symposia*, vol. 2017, pp. 1–10, 2017.

[14] Z. Zhai, Y. Wang, and J. H., "Origami-inspired on-demand deployable and collapsible mechanical metamaterials with tunable stiffness," in *Proc Natl Acad Sci115:*, pp. 2032–2037, Crossref. PubMed, 2018.

[15] J. Kim, D.-Y. Lee, S.-R. Kim, and K.-J. Cho, "A self-deployable origami structure with locking mechanism induced by buckling effect," in *2015 IEEE International Conference on Robotics and Automation (ICRA)*, (Seattle, WA), pp. 3166–3171, IEEE . Crossref, 2015.

[16] W. Wang, H. Rodrigue, and A. S-H., "Deployable soft composite structures," in *Sci Rep6:20869*, Crossref. PubMed, 2016.

[17] J. Blake and G. HB., "Haptic glove with mr brakes for virtual reality," *IEEE/ASME Trans Mechatronics*, vol. 14, pp. 606–615, 2009.

[18] A. Pettersson, S. Davis, J. O. Gray, T. J. Dodd, and T. Ohlsson, "Design of a magnetorheological robot gripper for handling of delicate food products with varying shapes," *J Food Eng*, vol. 98, pp. 332–338, 2010.

[19] J. Z. Chen and L. WH., "Design testing and control of a magne-torheological actuator for assistive knee braces," *Smart Mater Struct*, vol. 19, 2010.

[20] J.-S. Oh, Y.-M. Han, S.-R. Lee, and S.-B. Choi, "A 4-dof haptic master using er fluid for minimally invasive surgery system application," *Smart Mater Struct*, vol. 22, 2013.

[21] A. Sadeghi, L. Beccai, and B. Mazzolai, "Innovative soft robots based on electrorheological fluids," in *Conference on Intelligent Robots and Systems (IROS)* (I. International, ed.), (Vilamoura, Portugal), pp. 4237–4242, IEEE . Crossref, 2012.

[22] J. Shintake, B. Schubert, S. Rosset, H. Shea, and D. Floreano, "Variable stiffness actuator for soft robotics using dielectric elastomer and low-melting-point alloy," in *2015 IEEE/RSJ International Conference on Intelligent Robots and Systems (IROS)*, (Hamburg, Germany), pp. 1097–1102, IEEE . Crossref, 2015.

[23] A. M. Nasab, A. Sabzehzar, M. Tatari, C. Majidi, and W. Shan, "A soft gripper with rigidity tunable elastomer strips as ligaments," in *Soft Robotics*, pp. 411–420, Crossref. PubMed, 2017.

[24] B. Yang and Q. A. Lin, "Latchable microvalve using phase change of paraffin wax," *Sens Actuat A Phys*, vol. 134, pp. 194–200, 2007.

[25] E. Steltz, A. Mozeika, N. Rodenberg, E. Brown, and H. M. Jaeger, "Jsel: jamming skin enabled locomotion," in *2009 IEEE/RSJ International Conference on Intelligent Robots and Systems (IROS)*, (St. Louis, MO, USA), pp. 5672–5677, IEEE, 2009.

[26] E. Steltz, A. Mozeika, J. Rembisz, N. Corson, and H. Jaeger, "Jamming as an enabling technology for soft robotics," *In Electroactive Polymer Actuators and Devices (EAPAD)*, vol. 7642, p. 63, 2010.

[27] E. Lathrop, I. Adibnazari, N. Gravish, and M. T. Tolley, "Shear strengthened granular jamming feet for improved performance over natural terrain," in *2020 3rd IEEE International Conference on Soft Robotics (RoboSoft)*, (New Haven, CT, USA), pp. 388–393, IEEE, 2020.

[28] E. Brown, N. Rodenberg, J. Amend, A. Mozeika, E. Steltz, M. R. Zakin, H. Lipson, and H. M. Jaeger, "Universal robotic gripper based on the jamming of granular material," *Proc Natl Acad Sci*, vol. 107, pp. 18809–18814, 2010.

[29] A. A. Stanley, J. C. Gwilliam, and O. AM., "Haptic jamming: a deformable geometry variable stiffness tactile display using pneumatics and particle jamming," *In World Haptics Conference (WHC). Daejeon, South Korea: IEEE pp*, pp. 25–30, 2013.

[30] S. Follmer, D. Leithinger, A. Olwal, N. Cheng, and H. Ishii, "Jamming user interfaces: programmable particle stiffness and sensing for malleable and shape-changing devices," in *Proceedings of the 25th Annual ACM Symposium on User Interface Software and Technology*, (New York, NY, USA), pp. 519–528, ACM, 2012, . Crossref . Simon TM, Smith RT, Thomas BH. Wearable jamming mitten for virtual environment haptics. In Proceedings of the 2014 ACM International Symposium on Wearable Computers, ISWC'14, ACM. New York, NY, USA pp. 67–70. Crossref, 2014.

[31] J. R. Amend and H. Lipson, "Shape-shifting materials for pro-grammable structures," in *International Conference on Ubiquitous Computing: Workshop on Architectural Robotics*, (New York), Citeseer. , NY, USA: ACM, 2009. Keller S, Jaeger HM. Aleatory architectures. Gran Matter18:29. Crossref, 2016.

[32] M. Cianchetti, T. Ranzani, G. Gerboni, T. Nanayakkara, K. Althoefer, P. Dasgupta, and A. Menciassi, "Soft robotics technologies to address shortcomings in today's minimally invasive surgery: the stiff-flop approach," *Soft Robotics*, vol. 1, pp. 122–131, 2014.

[33] A. Jiang, G. Xynogalas, P. Dasgupta, K. Althoefer, and T. Nanayakkara, "Design of a variable stiffness flex-ible manipulator with composite granular jamming and membrane coupling," in *2012 IEEE/RSJ International Conference on Intelligent Robots and Systems (IROS)*, (Vilamoura, Porztugal), pp. 2922–2927, IEEE, 2012.

[34] A. Jiang, T. Ranzani, G. Gerboni, L. Lekstutyte, K. Althoefer, P. Dasgupta, and T. Nanayakkara, "Robotic granular jamming: does the membrane matter?," *Soft Robotics*, vol. 1, pp. 192–201, 2014.

[35] Y. S. Narang, A. Degirmenci, J. J. Vlassak, and R. D. Howe, "Transforming the dynamic response of robotic structures and systems through laminar jamming," *IEEE Robot Autom Letters*, vol. 3, pp. 688–695, 2017.

[36] Y. Narang, J. J. Vlassak, and H. RD., "Mechanically versatile soft machines through laminar jamming," *Adv Functional Materials*, vol. 28, p. 17071, 2018.

[37] I. Zubrycki and G. Granosik, "Novel haptic device using jamming principle for providing kinaesthetic feedback in glove-based control interface," *Journal of Intelligent Robot Systems*, vol. 85, pp. 413–429, 2017.

[38] Y. Zhang, D. Wang, Z. Wang, Y. Zhang, and J. Xiao, "Passive force-feedback gloves with joint-based variable impedance using layer jamming," in *IEEE Trans Haptics* (I. T. Haptics12:, ed.), pp. 269–280, PubMed, 2019.

[39] Y.-J. Kim, S. Cheng, S. Kim, and K. Iagnemma, "A novel layer jamming mechanism with tunable stiffness capability for minimally invasive surgery," *IEEE Trans on Robotics*, vol. 29, pp. 1031–1042, 2013.

[40] T. M. Simon, R. T. Smith, and B. H. Thomas, "Wearable jamming mitten for virtual environment haptics," in *Proceedings of the 2014 ACM International Symposium on Wearable Computers*, pp. 67–70, 2014.

[41] M. Brancadoro, M. Manti, S. Tognarelli, and M. Cianchetti, "Preliminary experimental study on variable stiff-ness structures based on fiber jamming for soft robots," in *2018 IEEE International Conference on Soft Robotics (RoboSoft)*, (Livorno, Italy), pp. 258–263, IEEE, 2018.

[42] M. Brancadoro, M. Manti, F. Grani, S. Tognarelli, A. Menciassi, and M. Cianchetti, "Towards a vari-able stiffness surgical manipulator based on fiber jamming transition," in *Front Robot AI6:12*, Crossref. PubMed, 2019.

[43] M. Brancadoro, M. Manti, S. Tognarelli, and M. Cianchetti, "Fiber jamming transition as a stiffening mechanism for soft robotics," in *Soft Robotics*, pp. 663–674, Crossref. PubMed, 2020.

[44] N. Vasios, Y. Narang, B. Aktaş, R. Howe, and K. Bertoldi, "Numerical analysis of periodic laminar and fibrous media undergoing a jamming transition," *Eur J Mech A Solids*, vol. 75, pp. 322–329, 2019.

[45] R. G. Budynas and N. JK., "Shigley's mechanical engineering design," in *Vol*, pp. 117–131, New York: McGraw-Hill, 1971.

[46] Y. Zheng, D. Wang, Z. Wang, Y. Zhang, Y. Zhang, and W. Xu, “Design of a lightweight force-feedback glove with a large workspace,” *Engineering*, vol. 4, pp. 869–880, 2018.

[47] H. Bai, S. Li, and R. F. Shepherd, “Elastomeric haptic devices for virtual and augmented reality,” *Advanced Functional Materials*, p. 2009364, 2021.

[48] J. Alexander, A. Roudaut, J. Steimle, K. Hornbæk, M. Bruns Alonso, S. Follmer, and T. Merritt, “Grand challenges in shape-changing interface research,” in *Proceedings of the 2018 CHI conference on human factors in computing systems*, pp. 1–14, 2018.

[49] S. Jong, “Arduino toolkit for the control of pneumatically actuated wearables,” B.S. thesis, University of Twente, 2020.

[50] T. J. Lisney, B. Ekesten, R. Tauson, O. Håstad, and A. Ödeen, “Using electroretinograms to assess flicker fusion frequency in domestic hens gallus gallus domesticus,” *Vision research*, vol. 62, pp. 125–133, 2012.

[51] Y. Zhai, Z. Wang, K.-S. Kwon, S. Cai, D. J. Lipomi, and T. N. Ng, “Printing multi-material organic haptic actuators,” *Advanced Materials*, vol. 33, no. 19, p. 2002541, 2021.

[52] D. Pyo, S. Ryu, K.-U. Kyung, S. Yun, and D.-S. Kwon, “High-pressure endurable flexible tactile actuator based on microstructured dielectric elastomer,” *Applied Physics Letters*, vol. 112, no. 6, p. 061902, 2018.

[53] E. Leroy, R. Hinchet, and H. Shea, “Multimode hydraulically amplified electrostatic actuators for wearable haptics,” *Advanced Materials*, vol. 32, no. 36, p. 2002564, 2020.

[54] J. Walker, T. Zidek, C. Harbel, S. Yoon, F. S. Strickland, S. Kumar, and M. Shin, “Soft robotics: a review of recent developments of pneumatic soft actuators,” in *Actuators*, vol. 9, p. 3, Multidisciplinary Digital Publishing Institute, 2020.

[55] B. Mosadegh, P. Polygerinos, C. Keplinger, S. Wennstedt, R. F. Shepherd, U. Gupta, J. Shim, K. Bertoldi, C. J. Walsh, and G. M. Whitesides, “Pneumatic networks for soft robotics that actuate rapidly,” *Advanced functional materials*, vol. 24, no. 15, pp. 2163–2170, 2014.

[56] C. Harrison and S. E. Hudson, “Providing dynamically changeable physical buttons on a visual display,” in *Proceedings of the SIGCHI Conference on Human Factors in Computing Systems*, pp. 299–308, 2009.

[57] S. Follmer, D. Leithinger, A. Olwal, A. Hogge, and H. Ishii, “inform: dynamic physical affordances and constraints through shape and object actuation.,” in *Uist*, vol. 13, pp. 2501988–2502032, 2013.

[58] M. Goulthorpe, M. Burry, and G. Dunlop, “Aegis hyposurface©: the bordering of university and practice,” 2001.

[59] A. A. Stanley, J. C. Gwilliam, and A. M. Okamura, "Haptic jamming: A deformable geometry, variable stiffness tactile display using pneumatics and particle jamming," in *2013 World Haptics Conference (WHC)*, pp. 25–30, IEEE, 2013.

[60] A. A. Stanley and A. M. Okamura, "Controllable surface haptics via particle jamming and pneumatics," *IEEE transactions on haptics*, vol. 8, no. 1, pp. 20–30, 2015.

[61] M. Koehler, N. S. Usevitch, and A. M. Okamura, "Model-based design of a soft 3-d haptic shape display," *IEEE Transactions on Robotics*, vol. 36, no. 3, pp. 613–628, 2020.

[62] A. Maimani and A. Roudaut, "Frozen suit: Toward a changeable stiffness suit and its application for haptic games," in *Proceedings of the CHI Conference on Human Factors in Computing Systems, Denver, CO, USA*, pp. 6–11, 2017.

[63] L. He, C. Xu, D. Xu, and R. Brill, "Pneuhaptic: delivering haptic cues with a pneumatic armband," in *Proceedings of the 2015 ACM International Symposium on Wearable Computers*, pp. 47–48, 2015.

[64] K. Gohlke, E. Hornecker, and W. Sattler, "Pneumatibles: exploring soft robotic actuators for the design of user interfaces with pneumotactile feedback," in *Proceedings of the TEI'16: Tenth International Conference on Tangible, Embedded, and Embodied Interaction*, pp. 308–315, 2016.

[65] A. Delazio, K. Nakagaki, R. L. Klatzky, S. E. Hudson, J. F. Lehman, and A. P. Sample, "Force jacket: Pneumatically-actuated jacket for embodied haptic experiences," in *Proceedings of the 2018 CHI Conference on Human Factors in Computing Systems*, pp. 1–12, 2018.

[66] D. P. Holland, E. J. Park, P. Polygerinos, G. J. Bennett, and C. J. Walsh, "The soft robotics toolkit: Shared resources for research and design," *Soft Robotics*, vol. 1, no. 3, pp. 224–230, 2014.

[67] A. Shtarbanov, "Flowio development platform–the pneumatic "raspberry pi" for soft robotics," in *Extended Abstracts of the 2021 CHI Conference on Human Factors in Computing Systems*, pp. 1–6, 2021.

[68] M. A. Robertson, M. Murakami, W. Felt, and J. Paik, "A compact modular soft surface with reconfigurable shape and stiffness," *IEEE/ASME Transactions on Mechatronics*, vol. 24, no. 1, pp. 16–24, 2018.

[69] M. Wehner, R. L. Truby, D. J. Fitzgerald, B. Mosadegh, G. M. Whitesides, J. A. Lewis, and R. J. Wood, "An integrated design and fabrication strategy for entirely soft, autonomous robots," *Nature*, vol. 536, no. 7617, pp. 451–455, 2016.

[70] C. Liao, *Gas ejector modeling for design and analysis*. Texas A&M University, 2008.

[71] J. H. Keenan, E. P. Neumann, and F. Lustwerk, "An investigation of ejector design by analysis and experiment," 1950.

[72] D.-W. Sun and I. W. Eames, "Recent developments in the design theories and applications of ejectors-a review," in *Fuel and Energy Abstracts*, vol. 5, p. 361, 1995.

[73] G. Emanuel, "Optimum performance for a single-stage gaseous ejector," *AIAA Journal*, vol. 14, no. 9, pp. 1292–1296, 1976.

[74] A. A. Stanley, A. Amini, C. Glick, N. Usevitch, Y. Mengüç, and S. J. Keller, "Lumped-parameter response time models for pneumatic circuit dynamics," *Journal of Dynamic Systems, Measurement, and Control*, vol. 143, no. 5, p. 051001, 2021.

[75] D. E. Weisberg, "A brief overview of the history of cad," *The engineering design revolution: The people, companies and computer systems that changed forever the practice of engineering*, pp. 2–1, 2008.

[76] L. P. Berg and J. M. Vance, "Industry use of virtual reality in product design and manufacturing: a survey," *Virtual reality*, vol. 21, no. 1, pp. 1–17, 2017.

[77] T. A. KELLEY, *The art of innovation: Lessons in creativity from IDEO, America's leading design firm*, vol. 10. Broadway Business, 2001.

[78] P. B. Paulus and B. A. Nijstad, *Group creativity: Innovation through collaboration*. Oxford University Press, 2003.

[79] B. Robertson and D. Radcliffe, "Impact of cad tools on creative problem solving in engineering design," *Computer-aided design*, vol. 41, no. 3, pp. 136–146, 2009.

[80] C. Bouchard, A. Aoussat, and R. Duchamp, "Role of sketching in conceptual design of car styling," *Journal of Design Research*, vol. 5, no. 1, pp. 116–148, 2006.

[81] M. Tovey, S. Porter, and R. Newman, "Sketching, concept development and automotive design," *Design studies*, vol. 24, no. 2, pp. 135–153, 2003.

[82] R. Balakrishnan, G. Fitzmaurice, G. Kurtenbach, and W. Buxton, "Digital tape drawing," in *Proceedings of the 12th annual ACM symposium on User interface software and technology*, pp. 161–169, 1999.

[83] S.-H. Bae and R. Kijima, "Digital styling for designers: in prospective automotive design," *Proc. Virt. Sys. and Mult*, 2003.

[84] R. Zammit and J. A. I. Munoz, "Has digital clay finally arrived?," *Computer-Aided Design and Applications*, vol. 11, no. sup1, pp. S20–S26, 2014.

[85] M. Fiorentino, R. de Amicis, G. Monno, and A. Stork, "Spacedesign: A mixed reality workspace for aesthetic industrial design," in *Proceedings. International Symposium on Mixed and Augmented Reality*, pp. 86–318, IEEE, 2002.

[86] S. Mueller, S. Im, S. Gurevich, A. Teibrich, L. Pfisterer, F. Guimbretière, and P. Baudisch, “Wireprint: 3d printed previews for fast prototyping,” in *Proceedings of the 27th annual ACM symposium on User interface software and technology*, pp. 273–280, 2014.

[87] S. Mueller, “Roma: Interactive fabrication with augmented reality and a robotic 3d printer,” 2018.

[88] D. Leen, R. Ramakers, and K. Luyten, “Strutmodeling: A low-fidelity construction kit to iteratively model, test, and adapt 3d objects,” in *Proceedings of the 30th Annual ACM Symposium on User Interface Software and Technology*, pp. 471–479, 2017.

[89] H. Agrawal, U. Umapathi, R. Kovacs, J. Frohnhofen, H.-T. Chen, S. Mueller, and P. Baudisch, “Protopiper: Physically sketching room-sized objects at actual scale,” in *Proceedings of the 28th Annual ACM Symposium on User Interface Software & Technology*, pp. 427–436, 2015.

[90] Y. Kim and S.-H. Bae, “Sketchingwithhands: 3d sketching handheld products with first-person hand posture,” in *Proceedings of the 29th Annual Symposium on User Interface Software and Technology*, pp. 797–808, 2016.

[91] H. Song, F. Guimbretière, and H. Lipson, “The modelcraft framework: Capturing freehand annotations and edits to facilitate the 3d model design process using a digital pen.,” *ACM Trans. Comput. Hum. Interact.*, vol. 16, no. 3, pp. 14–1, 2009.

[92] Y. Li, X. Luo, Y. Zheng, P. Xu, and H. Fu, “Sweepcanvas: Sketch-based 3d prototyping on an rgb-d image,” in *Proceedings of the 30th Annual ACM Symposium on User Interface Software and Technology*, pp. 387–399, 2017.

[93] K. Huo and K. Ramani, “Window-shaping: 3d design ideation in mixed reality,” in *Proceedings of the 2016 Symposium on Spatial User Interaction*, pp. 189–189, 2016.

[94] B. Yee, Y. Ning, and H. Lipson, “Augmented reality in-situ 3d sketching of physical objects,” in *Intelligent UI workshop on sketch recognition*, vol. 1, Citeseer, 2009.

[95] P. Lapides, E. Sharlin, M. C. Sousa, and L. Streit, “The 3d tractus: A three-dimensional drawing board,” in *First IEEE International Workshop on Horizontal Interactive Human-Computer Systems (TABLETOP’06)*, pp. 8–pp, IEEE, 2006.

[96] R. Schmidt and B. Wyvill, “Shapeshop: Free-form 3d design with implicit solid modeling,” in *Sketch-based Interfaces and Modeling*, pp. 287–312, Springer, 2011.

[97] T. Igarashi, S. Matsuoka, and H. Tanaka, “Teddy: a sketching interface for 3d freeform design,” in *ACM SIGGRAPH 2006 Courses*, pp. 11–es, 2006.

[98] H. Qin and D. Terzopoulos, “D-nurbs: a physics-based framework for geometric design,” *IEEE Transactions on Visualization and Computer Graphics*, vol. 2, no. 1, pp. 85–96, 1996.

[99] G. Evans, "Development of a 3d conceptual design environment using a commodity head mounted display virtual reality system," 2018.

[100] M. Matsumiya, H. Takemura, and N. Yokoya, "An immersive modeling system for 3d free-form design using implicit surfaces," in *Proceedings of the ACM symposium on Virtual reality software and technology*, pp. 67–74, 2000.

[101] J. P. Schulze, C. E. Hughes, L. Zhang, E. Edelstein, and E. Macagno, "Cavecad: a tool for architectural design in immersive virtual environments," in *The Engineering Reality of Virtual Reality 2014*, vol. 9012, p. 901208, International Society for Optics and Photonics, 2014.

[102] C. E. Hughes, L. Zhang, J. P. Schulze, E. Edelstein, and E. Macagno, "Cavecad: Architectural design in the cave," in *2013 IEEE Symposium on 3D User Interfaces (3DUI)*, pp. 193–194, IEEE, 2013.

[103] T. Chittenden, "Tilt brush painting: Chronotopic adventures in a physical-virtual threshold," *Journal of contemporary painting*, vol. 4, no. 2, pp. 381–403, 2018.

[104] D. F. Keefe, D. A. Feliz, T. Moscovich, D. H. Laidlaw, and J. J. LaViola Jr, "Cavepainting: a fully immersive 3d artistic medium and interactive experience," in *Proceedings of the 2001 symposium on Interactive 3D graphics*, pp. 85–93, 2001.

[105] Autodesk, "Vred,," 2020.

[106] A. Inc, "Ansys," *Southpointe*, vol. 275, 2014.

[107] C. Noon, R. Zhang, E. Winer, J. Oliver, B. Gilmore, and J. Duncan, "A system for rapid creation and assessment of conceptual large vehicle designs using immersive virtual reality," *Computers in Industry*, vol. 63, no. 5, pp. 500–512, 2012.

[108] K. Holtzblatt and H. Beyer, "Contextual design. interaction design foundation: Encycl," *Human-Computer Interact*, 2016.

[109] V. Kaptelinin, "Affordances and design," *The interaction design foundation*, 2014.

[110] S. Jayaram, J. Vance, R. Gadh, U. Jayaram, and H. Srinivasan, "Assessment of vr technology and its applications to engineering problems," *J. Comput. Inf. Sci. Eng.*, vol. 1, no. 1, pp. 72–83, 2001.

[111] S. Greenberg and B. Buxton, "Usability evaluation considered harmful (some of the time)," in *Proceedings of the SIGCHI conference on Human factors in computing systems*, pp. 111–120, 2008.

[112] D. Ledo, S. Houben, J. Vermeulen, N. Marquardt, L. Oehlberg, and S. Greenberg, "Evaluation strategies for hci toolkit research," in *Proceedings of the 2018 CHI Conference on Human Factors in Computing Systems*, pp. 1–17, 2018.

[113] D. R. Olsen Jr, “Evaluating user interface systems research,” in *Proceedings of the 20th annual ACM symposium on User interface software and technology*, pp. 251–258, 2007.

[114] S. Houben and N. Marquardt, “Watchconnect: A toolkit for prototyping smartwatch-centric cross-device applications,” in *Proceedings of the 33rd annual ACM conference on human factors in computing systems*, pp. 1247–1256, 2015.

[115] T. Seyed, A. Azazi, E. Chan, Y. Wang, and F. Maurer, “Sod-toolkit: A toolkit for interactively prototyping and developing multi-sensor, multi-device environments,” in *Proceedings of the 2015 International Conference on Interactive Tabletops & Surfaces*, pp. 171–180, 2015.